

Development and application of ultrafast scanning electron microscopy

Garming, M.W.H.

DOI

[10.4233/uuid:5b758b09-292f-4a3d-8fc3-221ae9cc02f3](https://doi.org/10.4233/uuid:5b758b09-292f-4a3d-8fc3-221ae9cc02f3)

Publication date

2022

Document Version

Final published version

Citation (APA)

Garming, M. W. H. (2022). *Development and application of ultrafast scanning electron microscopy*. [Dissertation (TU Delft), Delft University of Technology]. <https://doi.org/10.4233/uuid:5b758b09-292f-4a3d-8fc3-221ae9cc02f3>

Important note

To cite this publication, please use the final published version (if applicable). Please check the document version above.

Copyright

Other than for strictly personal use, it is not permitted to download, forward or distribute the text or part of it, without the consent of the author(s) and/or copyright holder(s), unless the work is under an open content license such as Creative Commons.

Takedown policy

Please contact us and provide details if you believe this document breaches copyrights. We will remove access to the work immediately and investigate your claim.

Development and application of ultrafast scanning electron microscopy

Development and application of ultrafast scanning electron microscopy

Proefschrift

ter verkrijging van de graad van doctor
aan de Technische Universiteit Delft,
op gezag van de Rector Magnificus prof. dr. ir. T.H.J.J. van der Hagen,
voorzitter van het College voor Promoties,
in het openbaar te verdedigen op maandag 19 december 2022 om 12:30 uur

door

Mathijs Wouter Henk GARMING

Master of Science in Applied Physics,
Technische Universiteit Delft, Nederland,
geboren te Breda, Nederland.

Dit proefschrift is goedgekeurd door de promotoren.

Samenstelling promotiecommissie bestaat uit:

Rector Magnificus,	voorzitter
Dr. ir. J.P. Hoogenboom,	Technische Universiteit Delft, promotor
Prof. dr. ir. P. Kruit,	Technische Universiteit Delft, promotor

Onafhankelijke leden:

Prof. dr. P.G. Steeneken	Technische Universiteit Delft
Prof. dr. A. Polman	AMOLF & Universiteit van Amsterdam
Prof. dr. M. Kociak	Université Paris-Saclay
Dr. S. Conesa-Boj	Technische Universiteit Delft
Dr. A. Tagliaferri	Politecnico di Milano
Prof. dr. B. Rieger	Technische Universiteit Delft, reservelid



The work in this dissertation was conducted at the Microscopy Instrumentation and Techniques group, formerly Charged Particle Optics group, department of Imaging Physics, faculty of Applied Sciences, Delft University of Technology.

Printed by: Ridderpint

Front cover: Artist impression of a sample pumped with laser pulses, generating mobile charge carriers in the bulk and trapped carriers on the surface, and probed with electron pulses resulting in the emission of secondary electrons.

Copyright © 2022 by M.W.H. Garming

ISBN 978-94-6384-395-9

An electronic version of this dissertation is available at
<http://repository.tudelft.nl/>.

Contents

Summary	vii
Samenvatting	ix
1 Introduction	1
1.1 Pulsed electron microscopy	2
1.2 Ultrafast electron microscopy applications	2
1.3 This project	4
References	5
2 Lock-in Ultrafast Scanning Electron Microscopy	11
2.1 Introduction	11
2.2 Methods	13
2.3 Results and discussion	14
2.3.1 Disentangling fast and slow dynamics	14
2.3.2 Surface dependent trapping	14
2.3.3 Photo-induced surface potentials	16
2.4 Conclusion	18
References	19
2.A1 Instrumentation and methodology	25
2.A2 Sample preparation	26
2.A3 Particle tracing simulations	28
2.A4 Retarding field analyser	30
References	32
3 High-NA Ultrafast Scanning Electron Microscopy	33
3.1 Introduction	33
3.2 Experimental section	35
3.3 Results	39
3.3.1 Spatial and temporal optical probe size	39
3.3.2 Ultrafast dynamics	40
3.3.3 Dipolar USEM contrast pattern	43
3.4 Conclusion	45
References	45
3.A1 Dose dependence of contrast	51
References	53

4	Imaging Resonant Micro-Cantilever Motion	55
4.1	Introduction	55
4.2	Setup and method	56
4.3	Results	58
4.4	Conclusion	62
	References	62
5	Development of a Laser Triggered Beam Blanker	65
5.1	Introduction	65
5.2	Principle	67
5.3	Parameters	69
5.3.1	L/d ratio	69
5.3.2	Device size	69
5.3.3	Spot displacement and blur	70
5.4	Design	71
5.4.1	Blanker	71
5.4.2	Optics	74
5.5	Construction and assembly	75
5.6	Testing	75
5.7	Discussion	82
5.8	Conclusion	83
	References	83
6	Conclusion	87
6.1	Outlook	88
	Acknowledgements	91
	Curriculum Vitae	93

Summary

Scanning electron microscopes (SEMs) can capture detail on the single nanometer length scale through the interaction of a tightly focused electron beam with a sample, but this impressive spatial resolution is not matched with a capability to resolve dynamic processes on the ultrafast time scale. A variety of processes occur at nanosecond and faster time scale, and at spatial scales out of reach of conventional light optical microscopes, for example in nanoscale solid state devices and nanomechanical resonators. An imaging tool combining high spatial and temporal resolution is therefore required.

In recent years, some research groups have worked on a technique to add ultrafast imaging to the capabilities of a SEM, building on concepts developed for transmission electron microscopy. In so-called ultrafast scanning electron microscopy (USEM), the combination of a pulsed laser and a pulsed electron beam enables the formation of movies capturing dynamics much faster than possible with a conventional SEM. Dynamics are initiated with femtosecond laser excitation of the sample and probed with electron beam pulses arriving with tightly controlled delay. The temporal resolution of this pump-probe scheme is determined by the laser and electron pulse duration. Secondary electrons, emitted from the top few nanometer of the sample, are collected and used to construct ultrafast movies. The aim of this thesis is to further develop the technique by making multiple improvements in our implementation, gaining additional insight into the contrast mechanism of USEM, and exploring new applications.

In chapter 2 our implementation of USEM for the application of recording semiconductor charge carrier dynamics is described. Carriers are photo-excited with a laser pulse and later probed with an electron pulse. Contrast arises as the number of secondary electrons collected depends on the presence of photo-generated charge carriers at the time and place the electron pulse probes. However, the yield difference is small and dynamics occurring at the surface and in bulk occur at different rates which can be hard to disentangle in the final results. Therefore we have implemented a detection scheme based on lock-in detection. Lock-in USEM allows for the disentangling of fast and slow processes, simultaneously visualizing fast bulk recombination and slow trapping. In experiments with Gallium (Ga) and Arsenide (As) terminated GaAs samples, we show the surface termination profoundly influences ultrafast movies, and present simulations that indicate the difference can be attributed to the formation of surface photovoltages. The results both demonstrate the surface sensitivity of USEM, and cement our understanding of the contrast mechanism.

Chapter 3 constitutes an improvement in the optical excitation resolution. Instead of a viewport in the side of the SEM vacuum chamber to illuminate the sample with a laser, the use of an inverted optical microscope built into USEM setup for laser excitation with high numerical aperture is demonstrated. The laser spot size is reduced from tens of microns in previous implementation to sub-micron in this configuration. This enables probing surface photovoltages with higher resolution. The approach is demonstrated on

MoS₂ flakes stamped on a transparent glass substrate, where ultrafast relaxation curves are measured on multiple different flakes as well as on different sites within the same flake. The new capability of sub-micron excitation narrows the gap between the optical and electron optical resolution in USEM and increases possibilities in measuring carrier dynamics in nanostructured devices and materials.

In chapter 4, an alternative application of USEM presented. The technique is applied for making ultrafast movies of a nanomechanical resonator at resonance with nanoscale spatio-temporal resolution. A cantilever is brought into motion through photo thermal excitation, and imaged with electron pulses to form a 50 MHz framerate video while maintaining electron beam resolution and depth of focus. The laser excitation is tuned to the cantilever resonance with a pulse picker using a pulse frequency modulation scheme. Ultrafast movies of both the 300 kHz fundamental and 2 MHz second mode oscillation are recorded, and the power and frequency dependence are characterised. Detected amplitudes span the range from 20 nm to 9 μm . This chapter shows that USEM can provide insightful movies of resonant oscillators, which can potentially aid in the development of novel nanomechanical resonators and the deepening of understanding of existing resonators.

Compared to conventional beam blankers, shorter electron pulses and better synchronisation between laser and electron pulses can potentially be generated by laser triggered blankers. A photoconductive switch facilitates rapid changes in voltage over the blanker plates creating fast electron pulses directly synchronised to the laser. In chapter 5, a design for a mm-sized laser triggered beam blanker making use of a commercially available photoconductive switch is presented, with the goal of generating 10 ps electron pulses at 5 kV acceleration voltage. The design features a 60 micron plate separation and is sufficiently compact to be incorporated into a scanning electron microscope through the standard blanker port. A working prototype has been constructed and characterised. Streak camera measurements demonstrate both laser induced electron beam deflection and electron pulse generation. The measured pulse duration is 530 ps, in close agreement with a calculated estimate based on the current experimental parameters. Faster pulses are expected to be possible through modification of the laser pulse duration and repetition frequency.

Samenvatting

De scannende elektronenmicroscop (SEM) is in staat details te vangen op lengteschalen van een enkele nanometer door gebruik van een gefocusseerde elektronenbundel, maar de mogelijkheid om dynamische processen op de ultrasnelle tijdschaal in beeld te brengen ontbreekt. Verscheidene processen komen voor op de nanoseconde tijdschaal en sneller, en met lengteschalen buiten bereik van conventionele optische microscopen, bijvoorbeeld in nanoschaal halfgeleiderapparatuur en nanoschaal mechanische resonatoren. Een microscop die hoge spatiële en tijdsresolutie combineert is daarom benodigd.

In de afgelopen jaren hebben enkele andere onderzoeksgroepen gewerkt aan een manier om beeldvorming met ultrasnelle tijdsresolutie toe te voegen aan mogelijkheden van SEM, middels concepten origineel ontwikkeld voor transmissie elektronenmicroscopen. In zogenaamde ultrasnelle scannende elektronenmicroscopie (USEM) maakt de combinatie van een gepulseerde laser en een gepulseerde elektronenbundel het mogelijk om filmpjes te maken die veel snellere dynamica kunnen vangen dan mogelijk met een reguliere SEM. Dynamische processen worden in gang gezet door het preparaat aan te slaan met een femtoseconde laserpuls. Een elektronenpuls die met een vertraging ten opzichte van de laserpuls aankomt zorgt voor signaal. De tijdsresolutie van dit pump-probe schema wordt bepaald door de duur van de laser- en elektronenpulsen. Secundaire elektronen, welke uit de bovenste paar nanometer van het sample komen, worden opgevangen en gebruikt om een ultrasnelle film te construeren. Het doel van dit proefschrift is de techniek verder te ontwikkelen middels verbeteringen in onze implementatie van USEM, het vergroten van het begrip van het contrast mechanisme, en het onderzoeken van nieuwe toepassingen.

In hoofdstuk 2 wordt onze implementatie van USEM beschreven, met als toepassing het meten van dynamica van ladingsdragers in halfgeleiders. Ladingsdragers worden met een laserpuls gegenereerd en met een elektronenpuls gedetecteerd. Het aantal gemeten secundaire elektronen hangt af van de aanwezigheid van ladingsdragers op het moment en de plek dat de elektronenpuls het preparaat raakt, dit zorgt voor contrast. Echter, het verschil is klein en daarnaast kunnen dynamica op de oppervlakte en daaronder verschillende tijdsconstanten hebben. Daarom hebben wij een detectiemethode geïmplementeerd met een fasegevoelige detector. Lock-in USEM maakt het mogelijk snelle en langzame processen uit elkaar te trekken, waardoor snelle bulk dynamica en langzame oppervlakte effecten tegelijk kunnen worden gemeten en afzonderlijk bekeken. Experimenten met GaAs met Gallium (Ga) toplaag en met Arsenide (As) toplaag laten zien dat de oppervlakte van het preparaat grote invloed heeft op het contrast in de ultrasnelle films. Simulatie resultaten tonen aan dat de verschillen voortkomen uit een oppervlakte potentiaal. De resultaten in dit hoofdstuk demonstreren de grote oppervlaktegevoeligheid van de meetmethode, en vergroten ook het begrip van hoe het contrast in de meetresultaten tot stand komt.

Hoofdstuk 3 gaat over een verbetering van de focus van de laser. Waar typisch een raam in de zijkant van de SEM vacuümkamer wordt gebruikt om de laser naar binnen te schijnen, wordt hier gebruik gemaakt van een ingebouwde geïnverteerde optische microscoop in de USEM opstelling. Dit zorgt voor een veel grotere numerieke apertuur en een verkleining van de laser focus van tientallen μm in de gebruikelijke configuratie naar minder dan een enkele μm . Hierdoor kunnen oppervlaktepotentialen met hogere resolutie gemeten worden. De methode wordt gedemonstreerd met dunne MoS_2 schilfers op transparant substraat, waar ultrasnel verval wordt gemeten op verschillende schilfers maar ook op meerdere plekken op dezelfde schilfer. De nieuwe mogelijkheid om te exciteren met sub-micron resolutie verkleint het verschil tussen de optische en elektronenoptische resolutie in USEM en schept nieuwe mogelijkheden voor het meten van halfgeleider dynamica op de nanoschaal.

In hoofdstuk 4 wordt een andere toepassing van USEM toegelicht. De techniek wordt toegepast voor het maken van ultrasnelle films van een mechanische resonator op nanoschaal. Een balkresonator wordt middels fothermische excitatie aangeslagen en in beeld gebracht met elektronenpulsen. Een filmpje met een beeldfrequentie van 50 MHz wordt samengesteld met de resolutie en scherptediepte van de elektronenbundel. De laser frequentie is afgestemd op de resonator door laserpulsen al dan niet door te laten volgens een puls frequentie modulatie schema. Filmpjes worden gemaakt van zowel de 300 kHz grondfrequentie als de 2 MHz harmonische trilling, en de vermogens- en frequentieafhankelijkheid worden gekarakteriseerd. Gemeten amplitudes zitten tussen 20 nm en 9 μm . Dit hoofdstuk laat zien dat USEM inzichtelijke videos van mechanische resonatoren op resonantie kan produceren, welke potentieel bruikbaar zijn voor de ontwikkeling van nieuwe resonatoren alsmede het vergroten van het begrip van bestaande resonatoren.

Vergeleken met conventionele deflectoren hebben deflectoren die met een laser worden geactiveerd de potentie om kortere elektronenpulsen te genereren die bovendien beter gesynchroniseerd zijn met de laserpulsen. Een fotogeleidende schakelaar faciliteert snelle verandering van de spanning over de deflector platen waardoor een korte puls wordt gegenereerd die direct aan de lasergesynchroniseerd is. In hoofdstuk 5 wordt een ontwerp voor een dergelijke deflector gepresenteerd, met als doel 10 ps pulsen bij 5 keV elektron energie. De afstand tussen de deflectorplaten is 60 μm en het hele ontwerp is compact genoeg om door de standaard poort in de SEM kolom gebracht te worden. Er wordt gebruik gemaakt van een commerciële fotogeleidende schakelaar. Een werkend prototype is gefabriceerd en hier zijn experimenten mee uitgevoerd. Hierbij is vastgesteld dat de elektronenbundel inderdaad gedeflecteerd wordt bij belichting van de schakelaar, en er is een elektronenpuls gemeten. De duur van deze puls is 530 ps, wat overeenkomt met een berekening gebaseerd op de huidige experimentele parameters. Snellere elektronenpulsen worden mogelijk geacht na aanpassing van de pulsduur en de repetitiefrequentie van de laser.

1

Introduction

Electron microscopy is a leading technique in terms of spatial resolution, as electrons enable better focus than possible with optical photons. In scanning electron microscopy (SEM), a nanosized probe is scanned over the sample to construct images containing information on the shape, size, and elemental composition of the specimen by detecting electrons and photons locally emitted by the sample under the action of the electron beam [1]. Transmission electron microscopes (TEMs) contain additional optics below the sample to focus transmitted electrons on a detector, which can also be used for diffraction based characterization of samples.

At typical electron microscope energies, electrons have picometre wavelengths; for 1 keV electrons it is 39 pm and this goes down to 2 pm at 300 kV. These short wavelengths reduce the effect of diffraction on the resolution, making aberrations all the more important. Over the years much attention has been devoted to reducing lens aberrations and the development of aberration correctors [2]. Improvements have been made to the point where sub-nm probe sizes are possible in SEM, and TEMs can achieve atomic resolution [3]. While further improvements are possible, these developments have had the effect of increased attention for other possible improvements to electron microscopy, including time resolved electron microscopy of dynamic processes.

Scanning electron microscopy works best on static or quasi-static specimens as modifications or movement of the sample during the scanning of the beam results in distorted images. Finite pixel dwell times combined with high pixel counts required for high fidelity imaging make for scanning times on the order of hundreds of milliseconds and longer. Omitting the scanning of images and focusing on a single probe position negates scan time limitations and pushes achievable time scales to the capabilities of the detector, typically on the microsecond or hundred nanosecond order of magnitude. Beyond this, the discrete nature of electrons and the finite current that can be contained into a nm sized electron probe form the next barrier. A 1 nA electron beam has a mere six electrons per ns on average, causing a level of shot noise in measurements on this time scale that is overwhelming.

Access to faster time scales is desirable as a variety of processes occur at time scales

of nanoseconds and below, and spatial scales smaller than what is achievable with conventional light optics [4, 5]. Examples can be found in the fields of plasmonics, chemical reactions, nanoscale solid state devices, and nanomechanical MEMS resonators. Techniques capable of interrogating nanoscale devices whose functioning relies on ultrafast phenomena can be useful tools in fostering our understanding of such devices and thereby aid their further development and support the trend of miniaturization.

1.1. Pulsed electron microscopy

The use of pulsed electron beams in a stroboscopic measurement scheme enables measurements on much faster time scales than possible with continuous electron beams. Electron pulses are synchronised to voltage pulses or laser excitation of the sample, and the resulting pump probe scheme has a time resolution determined by the duration and synchronisation accuracy of pump and probe pulses. In stroboscopic measurements electron pulses contain only a few electrons and the pump-probe cycle is repeated many times to acquire sufficient signal. An alternative to stroboscopic mode is repeated mode which has more electrons per pulse, therefore requiring fewer pulses and having less strict sample repeatability requirements at the expense of reduced spatial and temporal resolution [6]. Stroboscopic scanning electron microscopy was demonstrated in the 1960s for the inspection of microcircuits with 10 ns electron pulse duration [7]. Electron pulses were generated with beam blanking, the chopping a continuous beam by deflecting it over an aperture.

Further improvements to beam blanking technology have been made throughout the years by MacDonald et al. [8], Ura et al. [9], Winkler et al. [10], and Fehr et al. [11], demonstrating pulse durations down to the sub-ns and even sub-ps range. However, these gains in temporal resolution have proven difficult to combine with the sub-100 nm spatial resolution expected of electron-based imaging. Nanoscale spatial and temporal resolution combined was enabled by photoemission sources as reported by Merano et al. [12] and Hommelhoff et al. [13], where pulsed laser excitation of the electron source prompts emission of electron pulses. Photoemission sources have been developed and implemented by many labs to date [14–19].

Recent implementations of beam blanking to pulse the electron beam have also demonstrated the possibility of sub-100 ps electron pulses combined with high spatial resolution [19, 20]. Designs for a micro-fabricated laser triggered blanker have been presented and can potentially reduce the pulse duration to 100 fs, but this is still to be experimentally demonstrated [21, 22]. A blanker design based on a resonating microwave cavity in a TEM has shown 750 fs electron pulses in an experimental setting, demonstrating the fs time scale is accessible with electron beam blankers at high spatial resolution [23].

1.2. Ultrafast electron microscopy applications

Ultrafast electron microscopy has found various applications, using different contrast mechanisms to extract information about dynamics of the sample initiated by pulsed laser excitation. Diffraction measurements in transmission geometries or electron backscatter diffraction instruments allow for the measurement of phase changes. Examples include

experiments into the melting of aluminium by Siwick et al., where changes in diffraction pattern were corroborated with structural changes to the sample lattice structure [24]. This was measured in repeated mode on 20 nm films using a transmission diffraction instrument. Ultrafast backscatter electron diffraction has been demonstrated by Mohamed et al., who measured lattice expansion of InAs upon laser excitation [25]. Experiments at the Stanford Linear Accelerator facility have revealed molecular structure changes with MeV electron diffraction, such as the ring opening of 1,3-cyclohexadine [26, 27].

Besides diffraction based imaging, information can also be extracted from electron energy spectra. Electron energy loss spectroscopy relies on the monitoring of changes in electron energy after passing through or by a specimen to obtain information on the sample's electronic structure. Carbone et al. have implemented this with fs time resolution and revealed compression and expansion of graphite through spectral shift and intensity variation of loss peaks [28]. Fields around photonic nanostructures can also be examined in photon-induced near-field electron microscopy (PINEM) experiments, where the electron beam gains or loses photon energy quanta as it passes the specimen [29–31]. The effect was first demonstrated by Barwick et al. on carbon nanotubes, visualising the evanescent field in time and also showing the dependence of field strength on laser polarisation [32].

Ultrafast TEM with dark field transmission imaging has been shown capable of visualising strain wave dynamics in thin flakes of materials including MoS₂, WSe₂, and germanium [33–35]. Here, contrast stems from different degrees of scattering depending on whether incoming electrons hit a wave peak or trough.

Ultrafast scanning electron microscopy instrumentation with 300 fs temporal resolution and nm-scale probe resolution has been implemented by the Zewail lab using a photoemission pulsed electron source [25, 36]. A pulsed laser beam is split between the sample and the electron source to facilitate laser pumping and electron probing of the sample. The pump beam is focussed on the sample through an optically transparent window in the vacuum chamber with a lens on the outside, and pump probe delay can be regulated with an optical delay line [17]. An ultrafast USEM movie can be constructed by successively scanning images with various delays ranging from negative (electron probe before laser pump) to positive (laser pump before electron probe). If contrast is not sufficient to see a clear change around zero delay, the difference can be highlighted by plotting the difference between images recorded with positive and negative delay [37], a technique referred to as reference image subtraction.

The technique has been applied for studying the dynamics of semiconductor charge carriers, which can be detected through a carrier induced change in secondary electron yield of the material [17, 37, 38]. Materials studied include bulk crystal of GaAs [38], Si [39], and CdSe [40], but also more complicated systems such as p-n junctions [41] and black phosphorus flakes exhibiting anisotropic carrier diffusion [42]. Insulating materials have been studied as well with an ultrafast SEM setup working in ultrahigh vacuum, as been reported by Zani et al. [18]. Another application is the imaging of surface acoustic waves demonstrated by Najafi et al., where USEM data was used to determine the Young's modulus of a polymer material [43].

While the variety of samples examined with USEM over the past years has greatly increased, the user base of USEM is still very limited especially compared to ultrafast

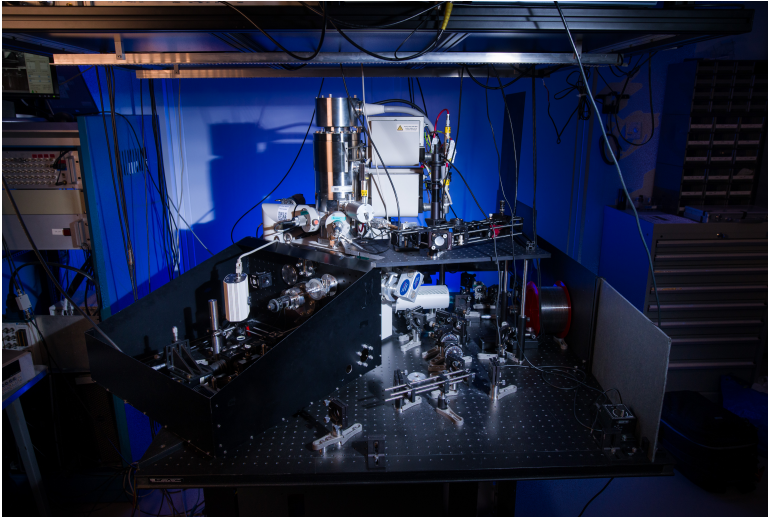


Figure 1.1: Overview of the pulsed SEM setup used for this thesis. Laser and electron optics are combined to perform ultrafast laser-pump electron-probe experiments. Photograph by Robert Moerland.

TEM. Also, USEM instrumentation has seen limited advances and may require extensive modifications to the SEM. Moreover, there are challenges in interpreting the results. The aim of this thesis is the further development of USEM instrumentation, particularly electron beam blanking to generate electron pulses as opposed to photoemission, and to make improvements in detection and excitation. We also aim to improve our knowledge of the contrast mechanism for better interpretation of results. Thus, we will build a better understanding of USEM allowing exploration of new applications for the technique.

1.3. This project

The starting point is a pulsed beam SEM developed for time resolved cathodoluminescence (CL) experiments (figure 1.1). The microscope is equipped with an integrated optical microscope, where CL is collected with a high numerical aperture (NA) objective and directed through a window in the vacuum door via a mirror mounted at 45 degrees [44]. Outside the vacuum, light can be focussed on a variety of photodetectors. A beam blanking scheme allows for the generation of 90 ps electron pulses at 4 kV acceleration voltage [20]. Previous work has shown the systems capabilities in to measure cathodoluminescent lifetimes, and variations in lifetime between particles and in nanophotonic structures [45, 46]. In addition, the system was used for a project on the development of a nanofabricated laser triggered blanker targeting faster pulse durations than possible with a conventional blanker [47]. For actuation of this blanker, a fs-laser was added to the setup as well. With the availability of a pulsed electron beam and a fs-laser, combining them and implementing USEM experiments is the next step.

In chapter 2, lock-in USEM is introduced. This extension of the regular USEM technique with lock-in detection allows for simultaneous measurement of ultrafast carrier

dynamics and slow carrier trapping, extending beyond the capabilities of the standard reference frame subtraction method. Comparing different surface terminations of GaAs highlights the surface sensitivity of the technique. New insight in the contrast mechanism for USEM carrier dynamics measurements is gained with particle tracing simulations that indicate the technique can probe localised surface photovoltages.

The scale at which these photovoltages can be probed is limited by the laser pump spot size. In chapter 3, the pump resolution is pushed to below 1 micron using a high-NA optical objective below the sample. Compared to the conventional illumination method this is an improvement of more than an order of magnitude. Flakes of MoS₂ exfoliated on a glass substrate are used to demonstrate high-NA USEM.

In terms of applications, USEM research has been mainly focussed on resolving semiconductor charge carriers, with only some exceptions. In chapter 4, the application of USEM for the imaging of nanomechanical movement is explored. We implement pulse frequency modulation to bring a mechanical cantilever resonator into motion via optical excitation, while electron pulses are used to image displacement. Using the cantilever of an atomic force microscope as model system, we construct ultrafast movies of the fundamental and second harmonic oscillations and characterise power and frequency response with USEM.

In chapter 5, the development of a new blanker is discussed. Building on a previous project about a laser triggered beam blanking, a new design is proposed for a laser triggered beam blanker with the goal of generating faster pulses than achievable with the existing implementation of electrostatic blanking. By triggering the laser with the blanker directly, trigger jitter of electronics driving an electrostatic blanker is avoided. A prototype of the design is constructed and characterised in the USEM setup.

A conclusion and outlook for possible future USEM experiments, applications, and developments are presented in chapter 6.

References

- [1] L. Reimer, *Scanning Electron Microscopy*, 2nd ed., Vol. 45, Springer Series in Optical Sciences (Springer Berlin Heidelberg, Berlin, Heidelberg, 1998).
- [2] C. Hetherington, “Aberration correction for TEM”, *Materials Today* **7**, 50–55 (2004).
- [3] D. A. Muller, T. Sorsch, S. Moccio, F. H. Baumann, K. Evans-Lutterodt, and G. Timp, “The electronic structure at the atomic scale of ultrathin gate oxides”, *Nature* **399**, 758–761 (1999).
- [4] W. E. King, G. H. Campbell, A. Frank, B. Reed, J. F. Schmerge, B. J. Siwick, B. C. Stuart, and P. M. Weber, “Ultrafast electron microscopy in materials science, biology, and chemistry”, *Journal of Applied Physics* **97**, 111101 (2005).
- [5] B. Barwick and A. H. Zewail, “Photonics and Plasmonics in 4D Ultrafast Electron Microscopy”, *ACS Photonics* **2**, 1391–1402 (2015).
- [6] L. Zhang, J. P. Hoogenboom, B. Cook, and P. Kruit, “Photoemission sources and beam blankers for ultrafast electron microscopy”, *Structural Dynamics* **6**, 10.1063/1.5117058 (2019).

- [7] G. S. Plows and W. C. Nixon, “Stroboscopic scanning electron microscopy”, *Journal of Physics E: Scientific Instruments* **1**, 595 (1968).
- [8] N. C. MacDonald, G. Y. Robinson, and R. M. White, “Time-resolved scanning electron microscopy and its application to bulk-effect oscillators”, *Journal of Applied Physics* **40**, 4516–4528 (1969).
- [9] K. Ura, H. Fujioka, and T. Hosokawa, “Picosecond pulse stroboscopic scanning electron microscope”, *Journal of Electron Microscopy* **27**, 247–252 (1978).
- [10] D. Winkler, R. Schmitt, M. Brunner, and B. Lischke, “Flexible picosecond probing of integrated circuits with chopped electron beams”, *IBM Journal of Research and Development* **34**, 189–203 (1990).
- [11] J. Fehr, W. Reiners, L. J. Balk, E. Kubalek, D. Köther, and I. Wolff, “A 100-femtosecond electron beam blanking system”, *Microelectronic Engineering* **12**, 221–226 (1990).
- [12] M. Merano, S. Sonderegger, A. Crottini, S. Collin, P. Renucci, E. Pelucchi, A. Malko, M. H. Baier, E. Kapon, B. Deveaud, and J. D. Ganière, “Probing carrier dynamics in nanostructures by picosecond cathodoluminescence”, *Nature* **2005** 438:7067 **438**, 479–482 (2005).
- [13] P. Hommelhoff, C. Kealhofer, and M. A. Kasevich, “Ultrafast electron pulses from a tungsten tip triggered by low-power femtosecond laser pulses”, *Physical Review Letters* **97**, 247402 (2006).
- [14] B. Barwick, S. P. Hyun, O. H. Kwon, J. S. Baskin, and A. H. Zewail, “4D imaging of transient structures and morphologies in ultrafast electron microscopy”, *Science* **322**, 1227–1231 (2008).
- [15] G. Herink, D. R. Solli, M. Gulde, and C. Ropers, “Field-driven photoemission from nanostructures quenches the quiver motion”, *Nature* **2012** 483:7388 **483**, 190–193 (2012).
- [16] D. A. Plemmons, P. K. Suri, and D. J. Flannigan, “Probing structural and electronic dynamics with ultrafast electron microscopy”, *Chemistry of Materials* **27**, 3178–3192 (2015).
- [17] J. Sun, V. A. Melnikov, J. I. Khan, and O. F. Mohammed, “Real-space imaging of carrier dynamics of materials surfaces by second-generation four-dimensional scanning ultrafast electron microscopy”, *Journal of Physical Chemistry Letters* **6**, 3884–3890 (2015).
- [18] M. Zani, V. Sala, G. Irde, S. M. Pietralunga, C. Manzoni, G. Cerullo, G. Lanzani, and A. Tagliaferri, “Charge dynamics in aluminum oxide thin film studied by ultrafast scanning electron microscopy”, *Ultramicroscopy* **187**, 93–97 (2018).
- [19] S. Meuret, M. Solà Garcia, T. Coenen, E. Kieft, H. Zeijlemaker, M. Lätzel, S. Christiansen, S. Y. Woo, Y. H. Ra, Z. Mi, and A. Polman, “Complementary cathodoluminescence lifetime imaging configurations in a scanning electron microscope”, *Ultramicroscopy* **197**, 28–38 (2019).

- [20] R. J. Moerland, I. G. C. Weppelman, M. W. H. Garming, P. Kruit, and J. P. Hoogenboom, “Time-resolved cathodoluminescence microscopy with sub-nanosecond beam blanking for direct evaluation of the local density of states”, *Optics Express* **24**, 24760 (2016).
- [21] I. G. C. Weppelman, R. J. Moerland, J. P. Hoogenboom, and P. Kruit, “Concept and design of a beam blanker with integrated photoconductive switch for ultrafast electron microscopy”, *Ultramicroscopy* **184**, 8–17 (2018).
- [22] I. G. C. Weppelman, R. J. Moerland, L. Zhang, E. Kieft, P. Kruit, and J. P. Hoogenboom, “Pulse length, energy spread, and temporal evolution of electron pulses generated with an ultrafast beam blanker”, *Structural Dynamics* **6**, 10.1063/1.5089517 (2019).
- [23] J. F. M. Van Rens, W. Verhoeven, E. R. Kieft, P. H. A. Mutsaers, and O. J. Luiten, “Dual mode microwave deflection cavities for ultrafast electron microscopy”, *Applied Physics Letters* **113**, 163104 (2018).
- [24] B. J. Siwick, J. R. Dwyer, R. E. Jordan, and R. J. D. Miller, “An Atomic-Level View of Melting Using Femtosecond Electron Diffraction”, *Science* **302**, 1382–1385 (2003).
- [25] O. F. Mohammed, D. S. Yang, S. K. Pal, and A. H. Zewail, “4D scanning ultrafast electron microscopy: Visualization of materials surface dynamics”, *Journal of the American Chemical Society* **133**, 7708–7711 (2011).
- [26] S. P. Weathersby, G. Brown, M. Centurion, T. F. Chase, R. Coffee, J. Corbett, J. P. Eichner, J. C. Frisch, A. R. Fry, M. Gühr, N. Hartmann, C. Hast, R. Hettel, R. K. Jobe, E. N. Jongewaard, J. R. Lewandowski, R. K. Li, A. M. Lindenberg, I. Makasyuk, J. E. May, D. McCormick, M. N. Nguyen, A. H. Reid, X. Shen, K. Sokolowski-Tinten, T. Vecchione, S. L. Vetter, J. Wu, J. Yang, H. A. Dürr, and X. J. Wang, “Mega-electron-volt ultrafast electron diffraction at SLAC National Accelerator Laboratory”, *Review of Scientific Instruments* **86**, 073702 (2015).
- [27] T. J. A. Wolf, D. M. Sanchez, J. Yang, R. M. Parrish, J. P. F. Nunes, M. Centurion, R. Coffee, J. P. Cryan, M. Gühr, K. Hegazy, A. Kirrander, R. K. Li, J. Ruddock, X. Shen, T. Vecchione, S. P. Weathersby, P. M. Weber, K. Wilkin, H. Yong, Q. Zheng, X. J. Wang, M. P. Minitti, and T. J. Martínez, “The photochemical ring-opening of 1,3-cyclohexadiene imaged by ultrafast electron diffraction”, *Nature Chemistry* **2019 11:6 11**, 504–509 (2019).
- [28] F. Carbone, O. H. Kwon, and A. H. Zewail, “Dynamics of Chemical Bonding Mapped by Energy-Resolved 4D Electron Microscopy”, *Science* **325**, 181–184 (2009).
- [29] F. J. Garcia De Abajo, A. Asenjo-Garcia, and M. Kociak, “Multiphoton Absorption and Emission by Interaction of Swift Electrons with Evanescent Light Fields”, *Nano Letters* **10**, 1859–1863 (2010).
- [30] A. Feist, K. E. Echternkamp, J. Schauss, S. V. Yalunin, S. Schäfer, and C. Ropers, “Quantum coherent optical phase modulation in an ultrafast transmission electron microscope”, *Nature* **2015 521:7551 521**, 200–203 (2015).

- [31] H. Liu, J. Spencer Baskin, A. H. Zewail, F. Carbone, A. Howie, and X. S. Xie, “Infrared PINEM developed by diffraction in 4D UEM”, *Proceedings of the National Academy of Sciences* **113**, 2041–2046 (2016).
- [32] B. Barwick, D. J. Flannigan, and A. H. Zewail, “Photon-induced near-field electron microscopy”, *Nature* **2009** 462:7275 **462**, 902–906 (2009).
- [33] Y. Zhang and D. J. Flannigan, “Observation of Anisotropic Strain-Wave Dynamics and Few-Layer Dephasing in MoS₂ with Ultrafast Electron Microscopy”, *Nano Letters* **19**, 8216–8224 (2019).
- [34] D. R. Cremons, D. A. Plemmons, and D. J. Flannigan, “Defect-mediated phonon dynamics in TaS₂ and WSe₂”, *Structural Dynamics* **4**, 044019 (2017).
- [35] D. R. Cremons, D. X. Du, and D. J. Flannigan, “Picosecond phase-velocity dispersion of hypersonic phonons imaged with ultrafast electron microscopy”, *Physical Review Materials* **1**, 073801 (2017).
- [36] D. S. Yang, O. F. Mohammed, and A. H. Zewail, “Scanning ultrafast electron microscopy”, *Proceedings of the National Academy of Sciences* **107**, 14993–14998 (2010).
- [37] B. Liao and E. Najafi, “Scanning ultrafast electron microscopy: A novel technique to probe photocarrier dynamics with high spatial and temporal resolutions”, *Materials Today Physics* **2**, 46–53 (2017).
- [38] J. Cho, T. Y. Hwang, and A. H. Zewail, “Visualization of carrier dynamics in p(n)-type GaAs by scanning ultrafast electron microscopy”, *Proceedings of the National Academy of Sciences of the United States of America* **111**, 2094–2099 (2014).
- [39] E. Najafi, V. Ivanov, A. Zewail, and M. Bernardi, “Super-diffusion of excited carriers in semiconductors”, *Nature Communications* **8**, 15177 (2017).
- [40] J. Sun, A. Adhikari, B. S. Shaheen, H. Yang, and O. F. Mohammed, “Mapping carrier dynamics on material surfaces in space and time using scanning ultrafast electron microscopy”, *Journal of Physical Chemistry Letters* **7**, 985–994 (2016).
- [41] E. Najafi, T. D. Scarborough, J. Tang, and A. Zewail, “Four-dimensional imaging of carrier interface dynamics in p-n junctions”, *Science* **347**, 164–167 (2015).
- [42] B. Liao, H. Zhao, E. Najafi, X. Yan, H. Tian, J. Tice, A. J. Minnich, H. Wang, and A. H. Zewail, “Spatial-temporal imaging of anisotropic photocarrier dynamics in black phosphorus”, *Nano Letters* **17**, 3675–3680 (2017).
- [43] E. Najafi, B. Liao, T. Scarborough, and A. Zewail, “Imaging surface acoustic wave dynamics in semiconducting polymers by scanning ultrafast electron microscopy”, *Ultramicroscopy* **184**, 46–50 (2018).
- [44] A. C. Zonneville, R. F. C. Van Tol, N. Liv, A. C. Narvaez, A. P. J. Effting, P. Kruit, and J. P. Hoogenboom, “Integration of a high-NA light microscope in a scanning electron microscope”, *Journal of Microscopy* **252**, 58–70 (2013).
- [45] M. W. H. Garming, I. G. C. Weppelman, P. De Boer, F. P. Martínez, R. Schirhagl, J. P. Hoogenboom, and R. J. Moerland, “Nanoparticle discrimination based on wavelength and lifetime-multiplexed cathodoluminescence microscopy”, *Nanoscale* **9**, 12727–12734 (2017).

- [46] R. J. Moerland, I. G. C. Weppelman, M. Scotuzzi, and J. P. Hoogenboom, “Nanoscale Imaging of Light-Matter Coupling Inside Metal-Coated Cavities with a Pulsed Electron Beam”, [Nano Letters](#) **18**, 6107–6112 (2018).
- [47] I. G. C. Weppelman, “Creation of electron pulses with a laser-triggered micro fabricated electron beam deflector”, PhD thesis (2021).

2

Lock-in Ultrafast Scanning Electron Microscopy

Visualizing charge carrier flow over interfaces or near surfaces meets great challenges concerning resolution and vastly different time scales of bulk and surface dynamics. Ultrafast or four-dimensional scanning electron microscopy (USEM) using a laser pump electron probe scheme circumvents the optical diffraction limit, but disentangling surface-mediated trapping and ultrafast carrier dynamics in a single measurement scheme has not yet been demonstrated. Here, we present lock-in USEM, which simultaneously visualizes fast bulk recombination and slow trapping. As a proof of concept, we show that the surface termination on GaAs, i.e., Ga or As, profoundly influences ultrafast movies. We demonstrate the differences can be attributed to trapping-induced surface voltages of approximately 100–200 mV, which is further supported by secondary electron particle tracing calculations. The simultaneous visualization of both competing processes opens new perspectives for studying carrier transport in layered, nanostructured, and two-dimensional semiconductors, where carrier trapping constitutes a major bottleneck for device efficiency.

2.1. Introduction

Observing and controlling the motion and recombination of excited charge carriers are keys to the functionality of semiconductor devices. Concomitant with miniaturization of device components, the relative contribution of trapping and recombination at surface or interface defects is increasing compared to that of bulk dynamics. Nevertheless, continuous miniaturization has so far been driving progress in many areas of technology, e.g., boosting computational power and clock speed in computer chips, increasing brightness and uniformity in lighting applications and displays, and enhancing efficiency in solar cells [2–6]. In fact, nanocomposite or nanostructured building blocks can now be found

This chapter has been published as M. W. H. Garming, M. Bolhuis, S. Conesa-Boj, P. Kruit, and J. P. Hoogenboom, “Lock-in Ultrafast Electron Microscopy Simultaneously Visualizes Carrier Recombination and Interface-Mediated Trapping”, *Journal of Physical Chemistry Letters* **11**, 8880–8886 (2020)

or have been proposed in many of these devices [7–10]. However, interface effects are becoming or, as in layered semiconductor solar cells, already are the main limitation of efficiency [11–14].

Traditionally used optical techniques are incapable of meeting the nanometer-range resolution requirement to map the flow of charge carriers over interfaces, and further complications arise from bulk and surface dynamics occurring on time scales that can differ by orders of magnitude [15–18]. In ultrafast scanning electron microscopy (USEM), a focused electron beam is used to probe the dynamics of a charge carrier distribution after laser excitation, thus bringing electron beam resolution into the traditional pump–probe schemes [19–22]. With USEM, carrier dynamics has been studied in bulk materials such as Si and GaAs, in crystals including CIGSe and CdSe, and in layered materials like black phosphorus and across a silicon p–n junction [23–32]. In all schemes, low-energy, 0–10 eV, secondary electrons (SEs) are used as the probe signal. As these SEs typically have a very short, only a few nanometers, mean free path, the bulk contribution to the signal is naturally limited, leading to an exquisite sensitivity to surface-related phenomena [33]. Indeed, marked differences in subsurface carrier diffusivity for differently functionalized CdTe have recently been revealed using USEM [34]. However, the visualization of trapping at the surface together with the ultrafast carrier recombination dynamics has not been demonstrated. Visualizing trapped states is important for two reasons. First, highlighting where and the extent to which carrier trapping occurs allows for optimization of device fabrication and subsequent quality control, including surface cleaning and termination strategies. Second, trapped charges may lead to the occurrence of localized potentials that could, depending on their magnitude, in turn impact carrier transport and recombination near the interface. Directly decoupling ultrafast bulk dynamics and longer time-scale surface-induced trapping in USEM would thus provide more insight into the interplay between these competing mechanisms and thus aid further optimization of nanostructured semiconductor devices.

Here, we introduce lock-in secondary electron detection in USEM and show that it allows the detection of processes slower than the pump–probe repetition rate simultaneously with bulk relaxation. Thus, within the ultrafast movie, we can study the fast nanosecond-scale dynamics of the sample as a function of pump–probe delay, while the slow dynamics is imprinted in the longer pump–probe delays where the detector is effectively gated to remove the fast dynamics.

We use GaAs to illustrate our lock-in SEM. GaAs is a III–V semiconductor often used in optoelectronic applications, either directly or as a base material for further epitaxial growth of layered or nanoscale devices [35]. The GaAs interface has been well studied and exhibits a different landscape of trap states depending on the crystal orientation [36, 37]. The (111) orientation in particular displays a smooth interface terminated with either a Ga or an As atomic layer [35, 38]. The landscape of trap states on GaAs surfaces is known to give rise to the occurrence of surface voltages upon photoexcitation on the order of only 100–200 mV [39]. We will show that despite this small potential difference, our implementation of lock-in USEM reveals a marked difference in image contrast pattern between the (111)A and (111)B orientations. We will further show that this pattern formation can indeed be assigned to the slow, i.e., surface trapping-induced, component in carrier relaxation, while in both cases, the fast dynamics is governed by

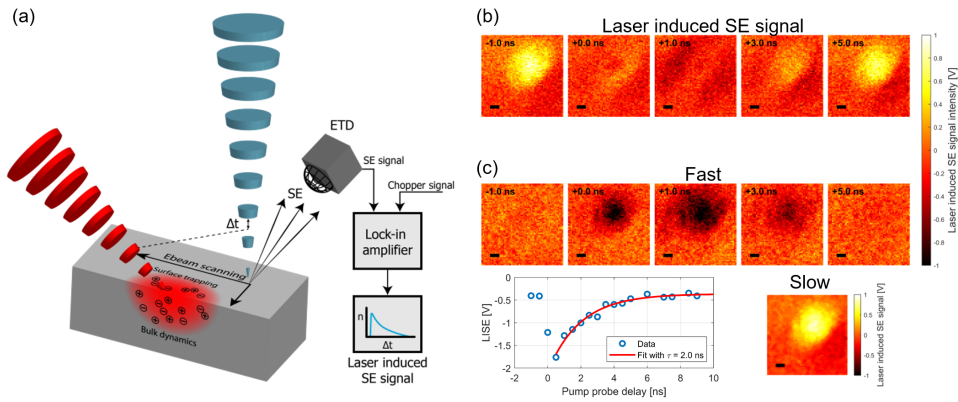


Figure 2.1: **Lock-in USEM disentangles bulk recombination and surface trapping in GaAs from a single ultrafast measurement sequence.** (a) In lock-in USEM, a laser pump electron probe scheme is used to map carrier dynamics through spatiotemporal variations in the secondary electron (SE) signal that are amplified through lock-in detection. (b) Scanning a GaAs (100) sample at various laser electron delays gives an ultrafast laser-induced SE image sequence. This shows the effect of carrier excitation at 0 ns on the SE yield, with the profile after ultrafast carrier relaxation matching that at negative times. (c) This movie can then be separated into the fast dynamics (<10 ns, top row) and slow relaxation processes, including carrier trapping (bottom right panel), allowing for data on both time scales to be acquired in a single measurement. The average intensity of the five darkest pixels in the fast dynamics figures decays single exponentially with a 2.0 ± 0.5 ns time constant, corresponding to the expected bulk carrier relaxation time of the material. Scale bars of $50 \mu\text{m}$.

direct carrier recombination. We confirm our results through particle tracing simulations, electron spectroscopy, and direct sample current measurements. The ability to observe both trapping-induced localized voltages and ultrafast carrier transport underneath and around these locations may provide new avenues for inspection and optimization of semiconductor nanodevices and the study of carrier dynamics in and around interfaces.

2.2. Methods

In USEM, a pulsed laser beam excites electrons from the valence to the conduction band while a pulsed electron beam scans the sample at a set time delay with respect to the laser pulse. The presence of photoexcited charge carriers leads to a modification of the SE yield, which is probed by the electron pulse [23, 40]. Through this laser-induced SE yield (LISE), i.e., the change in SE yield due to photoexcitation, the electron pulses thus probe the diffusion and relaxation of the excited carriers in time and space.

Our lock-in USEM setup (see also figure 2.1a and figure 2.A1) combines a 95 MHz Coherent Vitera-T Ti:Sapph femtosecond laser at 800 nm with a pulsed electron beam (sub-100 ps at 4keV [41]) in a FEI Quanta 200 FEG SEM instrument. Contrary to earlier implementations of USEM that have all required laser illumination of the electron source [21, 31, 42], we use a standard commercial beam blarker to pulse our electron beam (see also section 2.A1 of the supplementary information and ref [41]). Beam blankers are a well-established way to create pulsed electron beams [43–45] but have thus far not been applied to USEM systems. Moreover, we modulate the laser beam with a 940 Hz chopper and apply lock-in detection to directly extract the LISE signal from the SE

detector (figure 2.1a). While previous implementations relied on subtraction of long or negative time-delay data to obtain the LISE signal [22, 29, 30], this lock-in scheme ensures that any processes with a characteristic frequency between the pump–probe repetition frequency of 95 MHz and the 940 Hz chopping frequency will also be visible, on top of the ultrafast dynamic information. Additionally, the lock-in detection filters out minor drift-induced variations in the brightness of the image.

2.3. Results and discussion

2.3.1. Disentangling fast and slow dynamics

We illustrate our lock-in USEM acquisition in figure 2.1 using (100)-oriented GaAs, cleaned immediately before mounting in the USEM (see section 2.A2 of the supporting information). A bright laser induced secondary electron (LISE) signal is observed in figure 2.1b for pump–probe delays of 5–10 ns, i.e., approaching the inverse of our laser repetition frequency and, more importantly, much longer than the typical GaAs carrier lifetime of ~ 2 ns [46–48]. Upon laser illumination, this bright spot instantly disappears, after which, with an increasing pump–probe delay, first dark side bands appear at $\Delta t = 1$ ns, followed by a gradual recovery of the bright signal. We attribute the persistent laser-induced enhancement of the SE signal that occurs long after laser pulse illumination to the trapping of photoexcited charge carriers at trap states on the GaAs surface.

GaAs surfaces are well-known for containing trap states that can have lifetimes significantly longer than our 10 ns pump–probe repetition rate [47]. We note that lock-in detection allows for their detection provided relaxation is faster than the 1 kHz laser chopping frequency. As we will show later, the presence of these trapped charges leads to an increase in the SE detection efficiency through the action of an induced local electric field at the vacuum side of the interface. We will refer to this surface trapping with a time constant in the range from 10 ns to 1 ms as the slow component in the carrier relaxation dynamics. Under the assumption that this slow component contributes equally to the LISE signal for all delays, we extract the fast dynamics by subtracting the long pump–probe delay image from all other images (figure 2.1c). In this way, we obtain the typical dark contrast images previously reported for USEM on GaAs using the reference image subtraction technique [23]. Here, the dark contrast is seen to spread and return to the background signal on a 0–5 ns time scale. Plotting this fast LISE component versus delay time (figure 2.1c), we indeed recover a single-exponential lifetime (τ) of 2.0 ± 0.5 ns, typical of bulk carrier recombination. Four other measurements on two additional chips resulted in lifetimes of 1.9, 1.9, 1.9, and 2.0 ns (data not shown). Note that the occurrence of the dark side bands in the LISE signal in figure 2.1b at $\tau = 1$ ns coincides with the maximal spreading of photoexcited carriers in the top row of figure 2.1c. Thus, the two photoexcitation relaxation pathways of bulk recombination and trapping at surface defects both affect the LISE signal in qualitatively different ways and can, despite their different time scales, both be visualized in the same lock-in USEM measurements.

2.3.2. Surface dependent trapping

Surface composition and morphology can profoundly influence the nature of surface trap states [36, 37]; as the (100) surface is known to be terraced containing a multitude

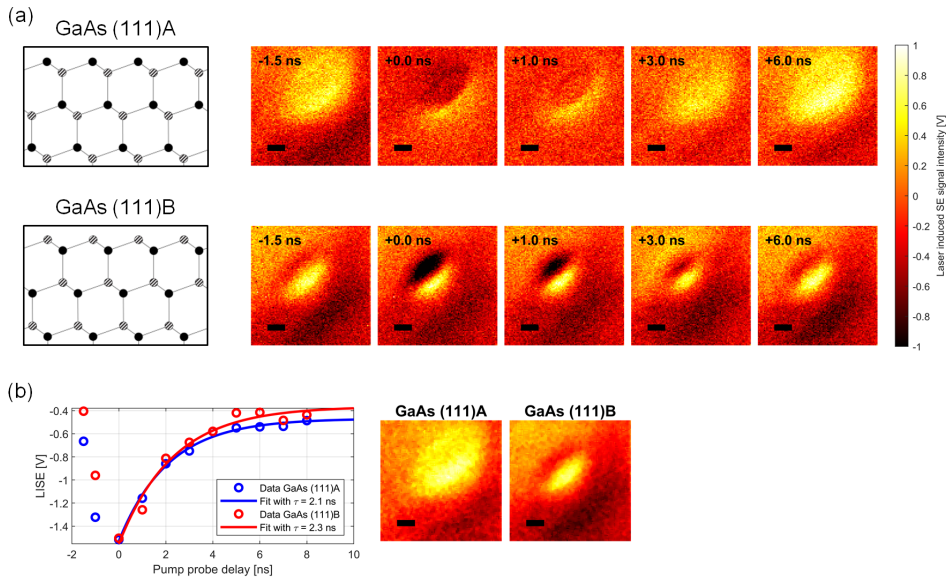


Figure 2.2: Visualization of trapping-induced contrast variations in ultrafast sequences of differently terminated GaAs (111). (a) GaAs (111) comes in a Ga-terminated A variant (top row) and an As-terminated B variant (bottom row), which display strikingly dissimilar ultrafast lock-in USEM image sequences, with a dipolar pattern appearing for the GaAs (111)B variant. In crystal structure images, solid-colored atoms correspond to Ga and dashed atoms to As. (b) Decomposing the videos in the slow components (images, right) and the ultrafast dynamics (graphed, left) in the same way as in figure 2.1 reveals that the underlying bulk carrier lifetime is similar for both surfaces. Thus, the contrast differences originate from the slower processes and are attributed to different local surface voltages that develop due to carrier trapping but do not strongly affect the subsurface carrier lifetime. Scale bars of 50 μm .

of surface reconstructions over small length scales, we switch to the (111) orientation to illustrate this. The (111)-oriented GaAs crystal exists in a gallium-terminated variety termed GaAs (111)A and an arsenide-terminated variety termed GaAs (111)B [35, 38]. The A and B variants thus have the same bulk structure but differ in their surface layer (figure 2.2a) and thereby exhibit a different energy landscape at the interface. We perform USEM measurements on both GaAs (111)A and GaAs (111)B following the same cleaning procedure mentioned above (section 2.A2 of the supporting information).

Our lock-in USEM gives a strikingly different appearance for the LISE images obtained on GaAs (111)A compared to those obtained on (111)B (figure 2.2a). Where the (111)A Ga surface shows a bright spot for the longer time delays similar to that obtained for the GaAs (100) surface, the (111)B As surface has a markedly smaller and more elliptical high-intensity spot. Immediately after laser illumination, this difference becomes even more pronounced with the (111)B surface developing a strong dipolar profile oriented perpendicular to the long axis of the laser illumination profile. The dark contrast lobe in this dipolar profile gradually diminishes with an increase in delay time. However, if, for both surfaces we subtract the slow component (image panels in figure 2.2b) from the temporal dynamics like we did for the GaAs (100) above, we retrieve lifetimes of 2.1 and 2.3

ns for GaAs (111)A and GaAs (111)B, respectively (figure 2.2b). An additional measurement on different chips gave values of 3.0 and 1.9 ns, respectively (data not shown). These ultrafast relaxation rates are reminiscent of bulk carrier recombination.

Despite the similarity of the underlying ultrafast carrier decay rate, the modulation of this ultrafast component with the persistent longer time-scale contribution gives rise to the even more dissimilar appearance of the LISE images for delays of a few nanoseconds, including the appearance of the dipolar contrast profile for GaAs (111)B. Like for GaAs (100), we attribute the slow component to carrier trapping at the GaAs–vacuum interface. This occupation of surface traps and the accompanying separation of charge carriers lead to the occurrence of a net surface potential [39]. The magnitude and sign of this surface potential depend on the density and energy levels of the trap states, which are different for different surface terminations and/or bulk crystal orientations. The surface potential in turn influences the trajectories of the low-energy secondary electrons [49], leading to a surface potential-dependent LISE collection efficiency. To examine this in more detail, we show in 2.3a diagonal cross sections for the intensity observed on the A and B surface lock-in USEM images at $\tau \approx 8$ ns. Asymmetric profiles are observed for both variants. The B variety shows a clear dip adjacent to a region of increased SE emission. This dip is slightly off center from the laser illumination spot. We note that this left side of the curve, and thus the top left corner of the LISE images in figures 2.2 and 2.4, is the position that in our experimental configuration is closest to the location of the SE detector. The dip is absent in the A variety, but here a smaller LISE yield is also observed on the left side of the photoexcitation region. Both surface terminations therefore exhibit asymmetry in the LISE images but to a different degree, which we argue is due to a difference in surface potential.

2.3.3. Photo-induced surface potentials

We corroborate our interpretation of a surface potential-induced variation of collection efficiency with SE collection efficiencies obtained from particles tracing simulations in the presence of a 100–200 mV photoinduced surface potential (details of the simulation are given in section 2.A3 of the supporting information). The calculated probability of SEs reaching the Everhart–Thornley detector (ETD) as a function of release position shows a marked similarity with our experimental results (figures 2.3a,b). A surface potential of 100–200 mV already results in a clearly asymmetric, dipolar shape of SE collection efficiency. The calculated change in SE collection efficiency is on the order of a percent, comparable to the amplitude observed in the experiment. Thus, the dipolar contrast profile appears to be due to a combination of reabsorption of SEs and redirection of emitted SEs to the detector. As the ETD field is rather weak in the space between the grounded SEM pole piece and the sample (see also figure 2.A3), many SEs are not sufficiently redirected and hit the pole piece instead of arriving at the ETD. Slowing these electrons with a local, positive surface potential partially prevents this from occurring. Moreover, SEs originating from the farther side of the laser illumination spot, as seen from the ETD, are not only slowed but also deflected toward the ETD by the surface potential. For electrons on the other side of the laser spot, the opposite occurs with the ETD field and surface potential field competing and thus creating a decrease in the SE collection efficiency in line with our experimental results. This surface potential-induced modulation of the SE

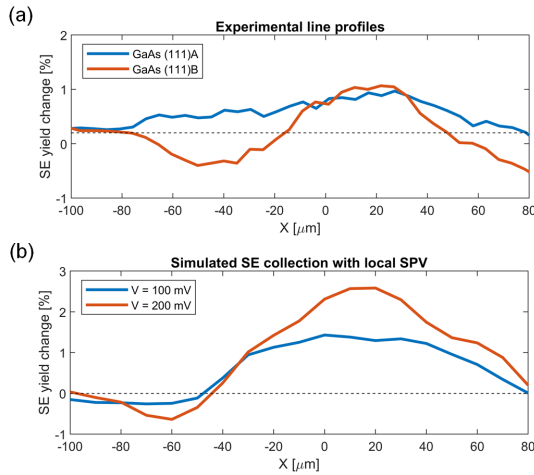


Figure 2.3: **Trapping-induced local surface voltages lead to a spatially varying secondary electron collection yield that is responsible for the dipolar pattern on GaAs (111)B.** (a) Diagonal cross section of laser-induced SE signal figures from top left to bottom right at an 8 ns pump–probe delay for GaAs (111)A and GaAs (111)B. For both curves, the number of SEs collected from the side of the laser spot closest to the detector is lowest. However, for the B variant, the contrast inversion is clearly visible; this is absent for the A variant. (b) Simulated SE collection efficiencies in the presence of a 100 and 200 mV Gaussian surface potential reproduce the dipolar contrast inversion when the surface voltage increases toward 200 mV.

collection efficiency is complementary to a possible change in SE yield, which is unrelated to the detector geometry and therefore intrinsically symmetric.

The surface potential of 100–200 mV corresponds to literature values of GaAs surface photovoltages that develop during continuous laser illumination [50–54]. On perovskites, surface photovoltages of ~ 5 V arising from continuous laser illumination have been recently reported to influence SE trajectories to such an extent that a position-dependent collection efficiency can be observed [49]. We exclude the occurrence of localized surface potentials of this magnitude using a home-built retarding field analyzer (see section 2.A4 of the supporting information). Here, a retarding field between sample and ETD prevents SEs with an energy smaller than the field magnitude from reaching the detector. The SE energy spectrum at each incident beam scan position is thus measured by varying the magnitude of the retarding field and collecting the transmitted electrons to construct an S curve. We observe no major shift in the curves obtained on laser-irradiated areas versus unirradiated areas on GaAs (111)B (figure 2.4a,b), meaning the difference in surface potential is less than the sensitivity of the spectrometer, i.e., $\lesssim 250$ mV. This is in stark contrast to calibration measurements using a biased copper wire that show clear curve shifts when an externally applied local potential is on the order of ≥ 1 V (figure 2.A7). Finally, we note that the observed asymmetry in the lock-in USEM images results from the combined action of the local surface potential and the ETD bias field that attracts the SEs. Indeed, if we measure the current through the sample as a function of scan position, the dipolar asymmetry disappears when the ETD bias field is switched off (figure 2.4c,d). Thus, we conclude that lock-in USEM enables simultaneous visualization of photoexcited

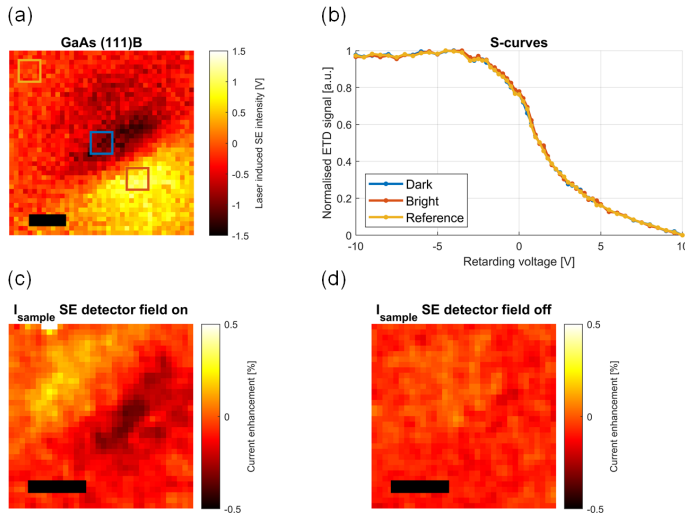


Figure 2.4: Retarding field spectral analyzer and direct sample current measurements confirm contrast variations are caused by small localized surface voltages. (a) Lock-in USEM result for GaAs (111)B with a 0 V retarding field on a grid placed above the sample. Regions of interest where the signal on the SE detector is monitored while the retarding voltage on the grid is varied are indicated with colored boxes. (b) For these regions, similar S curves are obtained, meaning the surface potential is <250 mV. (c) Measuring the current through the sample with the bias field on the SE detector switched on, we observe the contrast pattern inverted. (d) Switching the SE detector bias field off, we see the contrast pattern disappear, confirming the pattern is caused by an asymmetry in SE collection efficiency. Scale bars of $50 \mu\text{m}$

carrier relaxation via bulk recombination as well as trapping at energy states located at the interface.

2.4. Conclusion

The ability to see ultrafast carrier motion in relation to trapping-induced localized voltages provides new avenues for studying carrier transport in and across heterojunctions, underneath nanostructured surfaces, or at edges or layer transitions in two-dimensional materials. Locations for charge buildup can be directly visualized and related to changes in carrier recombination near the defect site. In the characterization of semiconductor nanodevices, lock-in USEM can enable the identification of spatial inhomogeneities that lead to trapping and thus aid the development of optimized fabrication processes and allow for quality control. Addition of an SE energy spectrum analyzer, like our initial retarding field analyzer, allows a direct evaluation of the magnitude of localized surface potentials, while the influence of the resulting internal field on charge dynamics can be monitored on time scales of nanoseconds or faster. We evaluated smooth interfaces, but localized impurities or defects that occur in fabrication may lead to larger local potentials. Lock-in USEM allows visualization of these fields, while their influence on local carrier transport can be simultaneously measured. Thus, we finally have the intriguing prospect of seeing charges move and recombine in and around the fields generated by trapped charges at high spatial and temporal resolution. This will ultimately aid the development

of semiconductor nanodevices, for instance, in photovoltaics and photodetection, where the optimization of the ratio between bulk dynamics and surface trapping is crucial in optimizing device performance.

References

- [1] M. W. H. Garming, M. Bolhuis, S. Conesa-Boj, P. Kruit, and J. P. Hoogenboom, “Lock-in Ultrafast Electron Microscopy Simultaneously Visualizes Carrier Recombination and Interface-Mediated Trapping”, *Journal of Physical Chemistry Letters* **11**, 8880–8886 (2020).
- [2] A. D. Franklin, “Nanomaterials in transistors: From high-performance to thin-film applications”, *Science* **349**, aab2750–aab2750 (2015).
- [3] M. Epicoco, “Knowledge patterns and sources of leadership: Mapping the semiconductor miniaturization trajectory”, *Research Policy* **42**, 180–195 (2013).
- [4] B. Chen, N. Pradhan, and H. Zhong, “From large-scale synthesis to lighting device applications of ternary I-III-VI semiconductor nanocrystals: Inspiring greener material emitters”, *Journal of Physical Chemistry Letters* **9**, 435–445 (2018).
- [5] R. Yu, Q. Lin, S. F. Leung, and Z. Fan, “Nanomaterials and nanostructures for efficient light absorption and photovoltaics”, *Nano Energy* **1**, 57–72 (2012).
- [6] B. Guzelturk, P. L. H. Martinez, Q. Zhang, Q. Xiong, H. Sun, X. W. Sun, A. O. Govorov, and H. V. Demir, “Excitronics of semiconductor quantum dots and wires for lighting and displays”, *Laser and Photonics Reviews* **8**, 73–93 (2014).
- [7] P. Yang, R. Yan, and M. Fardy, “Semiconductor nanowire: Whats next?”, *Nano Letters* **10**, 1529–1536 (2010).
- [8] O. Lopez-Sanchez, D. Lembke, M. Kayci, A. Radenovic, and A. Kis, “Ultrasensitive photodetectors based on monolayer MoS₂”, *Nature Nanotechnology* **8**, 497–501 (2013).
- [9] D. Van Dam, D. R. Abujetas, R. Paniagua-Domínguez, J. A. Sánchez-Gil, E. P. A. M. Bakkers, J. E. M. Haverkort, and J. Gómez Rivas, “Directional and polarized emission from nanowire arrays”, *Nano Letters* **15**, 4557–4563 (2015).
- [10] S. J. Gibson, B. van Kasteren, B. Tekcan, Y. Cui, D. van Dam, J. E. M. Haverkort, E. P. A. M. Bakkers, and M. E. Reimer, “Tapered InP nanowire arrays for efficient broadband high-speed single-photon detection”, *Nature Nanotechnology* **14**, 473–479 (2019).
- [11] Y. Cui, J. Wang, S. R. Plissard, A. Cavalli, T. T. T. Vu, R. P. J. Van Veldhoven, L. Gao, M. Trainor, M. A. Verheijen, J. E. M. Haverkort, and E. P. A. M. Bakkers, “Efficiency enhancement of InP nanowire solar cells by surface cleaning”, *Nano Letters* **13**, 4113–4117 (2013).
- [12] S. Y. Kim, T. R. Rana, J. H. Kim, D. H. Son, K. J. Yang, J. K. Kang, and D. H. Kim, “Limiting effects of conduction band offset and defect states on high efficiency CZTSSe solar cell”, *Nano Energy* **45**, 75–83 (2018).

- [13] J. E. M. Haverkort, E. C. Garnett, and E. P. A. M. Bakkers, “Fundamentals of the nanowire solar cell: Optimization of the open circuit voltage”, *Applied Physics Reviews* **5**, 031106 (2018).
- [14] J. V. Holm, H. I. Jørgensen, P. Krogstrup, J. Nygård, H. Liu, and M. Aagesen, “Surface-passivated GaAsP single-nanowire solar cells exceeding 10% efficiency grown on silicon”, *Nature Communications* **4**, 1–5 (2013).
- [15] R. Haight, “Electron dynamics at surfaces”, *Surface Science Reports* **21**, 275–325 (1995).
- [16] Y. Yang, M. Yang, D. T. Moore, Y. Yan, E. M. Miller, K. Zhu, and M. C. Beard, “Top and bottom surfaces limit carrier lifetime in lead iodide perovskite films”, *Nature Energy* **2**, 1–7 (2017).
- [17] B. Pattengale and J. Huang, “Implicating the contributions of surface and bulk states on carrier trapping and photocurrent performance of BiVO₄ photoanodes”, *Physical Chemistry Chemical Physics* **19**, 6831–6837 (2017).
- [18] B. S. Shaheen, A. M. El-Zohry, J. Yin, M. De Bastiani, S. De Wolf, O. M. Bakr, and O. F. Mohammed, “Visualization of charge carrier trapping in silicon at the atomic surface level using four-dimensional electron imaging”, *Journal of Physical Chemistry Letters* **10**, 1960–1966 (2019).
- [19] D. S. Yang, B. Liao, and O. F. Mohammed, “Scanning ultrafast electron microscopy: Four-dimensional imaging of materials dynamics in space and time”, *MRS Bulletin* **43**, 491–496 (2018).
- [20] A. H. Zewail, “Four-dimensional electron microscopy”, *Science* **328**, 187–193 (2010).
- [21] O. F. Mohammed, D. S. Yang, S. K. Pal, and A. H. Zewail, “4D scanning ultrafast electron microscopy: Visualization of materials surface dynamics”, *Journal of the American Chemical Society* **133**, 7708–7711 (2011).
- [22] B. Liao and E. Najafi, “Scanning ultrafast electron microscopy: A novel technique to probe photocarrier dynamics with high spatial and temporal resolutions”, *Materials Today Physics* **2**, 46–53 (2017).
- [23] J. Cho, T. Y. Hwang, and A. H. Zewail, “Visualization of carrier dynamics in p(n)-type GaAs by scanning ultrafast electron microscopy”, *Proceedings of the National Academy of Sciences of the United States of America* **111**, 2094–2099 (2014).
- [24] R. Bose, A. Bera, M. R. Parida, A. Adhikari, B. S. Shaheen, E. Alarousu, J. Sun, T. Wu, O. M. Bakr, and O. F. Mohammed, “Real-space mapping of surface trap states in CIGSe nanocrystals using 4D electron microscopy”, *Nano Letters* **16**, 4417–4423 (2016).
- [25] B. Liao, E. Najafi, H. Li, A. J. Minnich, and A. H. Zewail, “Photo-excited hot carrier dynamics in hydrogenated amorphous silicon imaged by 4D electron microscopy”, *Nature Nanotechnology* **12**, 871–876 (2017).
- [26] B. Liao, H. Zhao, E. Najafi, X. Yan, H. Tian, J. Tice, A. J. Minnich, H. Wang, and A. H. Zewail, “Spatial-temporal imaging of anisotropic photocarrier dynamics in black phosphorus”, *Nano Letters* **17**, 3675–3680 (2017).

- [27] B. S. Shaheen, J. Sun, D. S. Yang, and O. F. Mohammed, "Spatiotemporal observation of electron-impact dynamics in photovoltaic materials using 4D electron microscopy", *Journal of Physical Chemistry Letters* **8**, 2455–2462 (2017).
- [28] D. S. Yang, O. F. Mohammed, and A. H. Zewail, "Environmental scanning ultrafast electron microscopy: Structural dynamics of solvation at interfaces", *Angewandte Chemie - International Edition* **52**, 2897–2901 (2013).
- [29] E. Najafi, T. D. Scarborough, J. Tang, and A. Zewail, "Four-dimensional imaging of carrier interface dynamics in p-n junctions", *Science* **347**, 164–167 (2015).
- [30] E. Najafi, V. Ivanov, A. Zewail, and M. Bernardi, "Super-diffusion of excited carriers in semiconductors", *Nature Communications* **8**, 15177 (2017).
- [31] M. Zani, V. Sala, G. Irde, S. M. Pietralunga, C. Manzoni, G. Cerullo, G. Lanzani, and A. Tagliaferri, "Charge dynamics in aluminum oxide thin film studied by ultrafast scanning electron microscopy", *Ultramicroscopy* **187**, 93–97 (2018).
- [32] R. Bose, J. Sun, J. I. Khan, B. S. Shaheen, A. Adhikari, T. K. Ng, V. M. Burlakov, M. R. Parida, D. Priante, A. Goriely, B. S. Ooi, O. M. Bakr, and O. F. Mohammed, "Real-space visualization of energy loss and carrier diffusion in a semiconductor nanowire array using 4D electron microscopy", *Advanced Materials* **28**, 5106–5111 (2016).
- [33] L. Reimer, "Emission of Backscattered and Secondary Electrons", in *Scanning electron microscopy* (Springer Berlin Heidelberg, Berlin, Heidelberg, 1998), pp. 135–169.
- [34] A. M. El-Zohry, B. S. Shaheen, V. M. Burlakov, J. Yin, M. N. Hedhili, S. Shikin, B. Ooi, O. M. Bakr, and O. F. Mohammed, "Extraordinary carrier diffusion on CdTe surfaces uncovered by 4D electron microscopy", *Chem* **5**, 706–718 (2019).
- [35] N. Moll, A. Kley, E. Pehlke, and M. Scheffler, "GaAs equilibrium crystal shape from first principles", *Physical Review B - Condensed Matter and Materials Physics* **54**, 8844–8855 (1996).
- [36] H. J. Joyce, P. Parkinson, N. Jiang, C. J. Docherty, Q. Gao, H. H. Tan, C. Jagadish, L. M. Herz, and M. B. Johnston, "Electron mobilities approaching bulk limits in "surface-free" GaAs nanowires", *Nano Letters* **14**, 5989–5994 (2014).
- [37] O. Demichel, M. Heiss, J. Bleuse, H. Mariette, and I. A. Fontcuberta Morral, "Impact of surfaces on the optical properties of GaAs nanowires", *Applied Physics Letters* **97**, 201907 (2010).
- [38] M. R. Brozel and G. E. Stillman, "Properties of gallium arsenide (3rd edition)", *Institution of Engineering and Technology*, 145–149 (1996).
- [39] L. Kronik and Y. Shapira, "Surface photovoltage spectroscopy of semiconductor structures: At the crossroads of physics, chemistry and electrical engineering", *Surface and Interface Analysis* **31**, 954–965 (2001).
- [40] J. Sun, A. Adhikari, B. S. Shaheen, H. Yang, and O. F. Mohammed, "Mapping carrier dynamics on material surfaces in space and time using scanning ultrafast electron microscopy", *Journal of Physical Chemistry Letters* **7**, 985–994 (2016).

- [41] R. J. Moerland, I. G. C. Weppelman, M. W. H. Garming, P. Kruit, and J. P. Hoogenboom, “Time-resolved cathodoluminescence microscopy with sub-nanosecond beam blanking for direct evaluation of the local density of states”, *Optics Express* **24**, 24760 (2016).
- [42] J. Sun, V. A. Melnikov, J. I. Khan, and O. F. Mohammed, “Real-space imaging of carrier dynamics of materials surfaces by second-generation four-dimensional scanning ultrafast electron microscopy”, *Journal of Physical Chemistry Letters* **6**, 3884–3890 (2015).
- [43] N. C. MacDonald, G. Y. Robinson, and R. M. White, “Time-resolved scanning electron microscopy and its application to bulk-effect oscillators”, *Journal of Applied Physics* **40**, 4516–4528 (1969).
- [44] G. Y. Robinson, “Stroboscopic scanning electron microscopy at Gigahertz frequencies”, *Review of Scientific Instruments* **42**, 251–255 (1971).
- [45] K. Ura, H. Fujioka, and T. Hosokawa, “Picosecond pulse stroboscopic scanning electron microscope”, *Journal of Electron Microscopy* **27**, 247–252 (1978).
- [46] M. C. Beard, G. M. Turner, and C. A. Schmuttenmaer, “Transient photoconductivity in GaAs as measured by time-resolved terahertz spectroscopy”, *Physical Review B - Condensed Matter and Materials Physics* **62**, 15764–15777 (2000).
- [47] A. W. Walker, S. Heckelmann, C. Karcher, O. Höhn, C. Went, M. Niemeyer, A. W. Bett, and D. Lackner, “Nonradiative lifetime extraction using power-dependent relative photoluminescence of III-V semiconductor double-heterostructures”, *Journal of Applied Physics* **119**, 155702 (2016).
- [48] J. S. Weiner and P. Y. Yu, “Free carrier lifetime in semi-insulating GaAs from time-resolved band-to-band photoluminescence”, *Journal of Applied Physics* **55**, 3889–3891 (1984).
- [49] G. Irde, S. M. Pietralunga, V. Sala, M. Zani, J. M. Ball, A. J. Barker, A. Petrozza, G. Lanzani, and A. Tagliaferri, “Imaging photoinduced surface potentials on hybrid perovskites by real-time Scanning Electron Microscopy”, *Micron* **121**, 53–65 (2019).
- [50] L. Burstein, J. Bregman, and Y. Shapira, “Characterization of interface states at III-V compound semiconductor-metal interfaces”, *Journal of Applied Physics* **69**, 2312–2316 (1991).
- [51] J. Łagowski, I. Baltov, and H. C. Gatos, “Surface photovoltage spectroscopy and surface piezoelectric effect in GaAs”, *Surface Science* **40**, 216–226 (1973).
- [52] G. M. Marshall, G. P. Lopinski, F. Bensebaa, and J. J. Dubowski, “Electro-optic investigation of the surface trapping efficiency in n-alkanethiol SAM passivated GaAs(001)”, *Nanotechnology* **22**, 10.1088/0957-4484/22/23/235704 (2011).
- [53] P. Siffalovic, M. Drescher, and U. Heinzmann, “Femtosecond time-resolved core-level photoelectron spectroscopy tracking surface photovoltage transients on p-GaAs”, *Europhysics Letters (EPL)* **60**, 924–930 (2002).

- [54] D. Mao, A. Kahn, G. LeLay, M. Marsi, Y. Hwu, G. Margaritondo, M. Santos, M. Shayegan, L. T. Florez, and J. P. Harbison, “Surface photovoltage and band bending at metal/GaAs interfaces: A contact potential difference and photoemission spectroscopy study”, *Journal of Vacuum Science and Technology B: Microelectronics and Nanometer Structures* **9**, 2083–2089 (1991).

Appendix

2.A1. Instrumentation and methodology

Our USEM, schematically shown in figure 2.A1, is based on a FEI Quanta 200 FEG SEM equipped with a 95 MHz Coherent Vitara-T Ti:Sapph fs-laser. The electron beam is pulsed with a fast beam blanker enabling sub 100 ps electron pulse duration at 4 kV by rapidly deflecting the electron beam over a blanking aperture positioned in the electron objective lens. There is a linear relation between pulse duration and acceleration voltage. Major advantages of this technique of pulsing the beam over photoemission sources are easy switching between continuous and pulsed beam, and insensitivity to alignment drift providing stability allowing for many hours of uninterrupted operation. The laser enters the vacuum through a viewport in the side of the vacuum chamber, resulting in an elliptical spot measuring some 55 by 95 micron FWHM on the minor and major axes. Laser and electron pulses are locked by triggering the electric pulse generator driving the beam blanker on a photodiode illuminated with the laser; the pump probe delay is regulated through an electronic delay box (SRS DB64).

In addition to the optical path through the viewport, the setup is also equipped with an inverted optical microscope below the sample, which is used for alignment purposes to achieve spatiotemporal coincidence between laser and electron pulses on the sample. Spatial alignment is done by imaging the laser spot and electron beam induced cathodoluminescence (CL) on an ITO covered glass slide with a CCD camera, and adjusting to make the spots coincide. Temporal alignment can be performed through a time correlated single photon counting (TCSPC) scheme, where the arrival time of electron beam generated CL is compared to the arrival time of specular reflected laser light.

Lock-in detection is implemented by chopping the laser beam at a frequency of 940 Hz, and picking up the resulting modulation on the SE signal at this frequency with a lock-in amplifier (EG&G Model 5101). The output of the lock-in amplifier, i.e. the difference between the SE yield achieved with and without the laser excitation, is referred to as the laser induced SE (LISE) signal. As no data is subtracted in obtaining the LISE signal, any processes with a characteristic frequency between the pump probe repetition frequency of 95 MHz and 940Hz chopping frequency will also remain visible, albeit without dynamic information. Additionally, minor drift induced variations in brightness of the image will be filtered out in the lock-in detection, allowing for very long exposure times.

A lock-in USEM measurement series is conducted by sequentially performing full image scans around the laser focus location with a fixed pump-probe delay, repeating until all delays are covered. The experiments are conducted with a laser fluence of some $4 \cdot 10^{-5} \text{ J cm}^{-2}$, electron acceleration voltage of 30 kV, and pixel dwell time of 50 ms. An average of 5 electrons per pulse is used, which, in combination with the short distance between blanking aperture and sample, makes for negligible temporal broadening of the

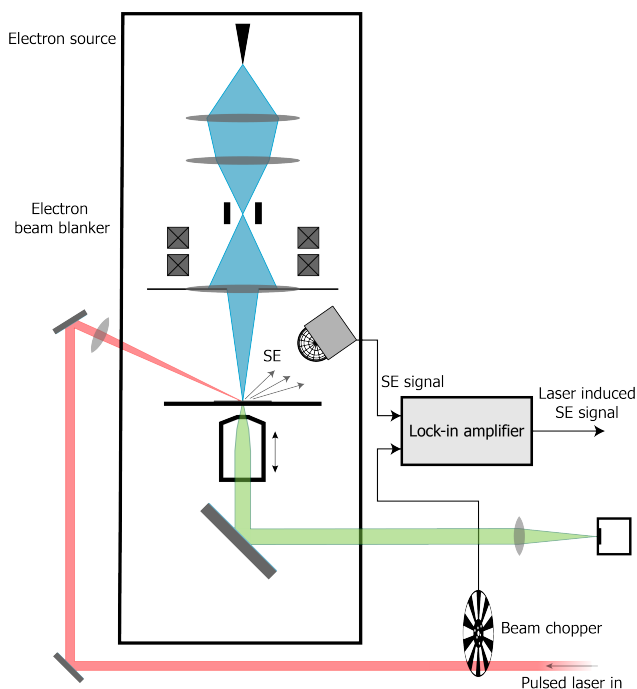


Figure 2.A1: Our USEM set-up makes use of beam blanking for electron pulse generation, and is equipped with a viewport to facilitate fs laser excitation. The laser is chopped for lock-in detection and an inverted optical microscope is used for alignment purposes.

pulse. The measurement order of the pump-probe delays was randomised to prevent misinterpretation of long term effects (e.g. possible sample drift) as ultrafast dynamics. Lifetimes are obtained by fitting a single exponential function to the mean intensity of the darkest 5 pixels in the ultrafast images; in order to reduce the effects of noise, the ROI is cropped to roughly twice the spot size at 0 ns for measurements obtained with a field of view larger than this.

Conversion from lock-in output voltage to a fractional change in collected SE signal can be done by dividing the lock-in output voltage by the amplifier gain and dividing that by the voltage of the ETD signal relative to its zero level. The lock-in amplifier gain has here been determined by comparing the lock-in output voltage to the known peak-peak voltage of a square wave at the input.

2.A2. Sample preparation

GaAs has a native oxide layer [1–3] that we remove prior to the measurements. The full sample preparation procedure is as follows. Chips are diced from a wafer and cleaned through sonication for 5 minutes in acetone and subsequently IPA, followed by 1 minute of oxygen plasma cleaning at 300W. The chip is then washed in ammonium hydroxide solution (25%) for 90s to remove the oxide layer [2, 3], rinsed with DI water, dried with

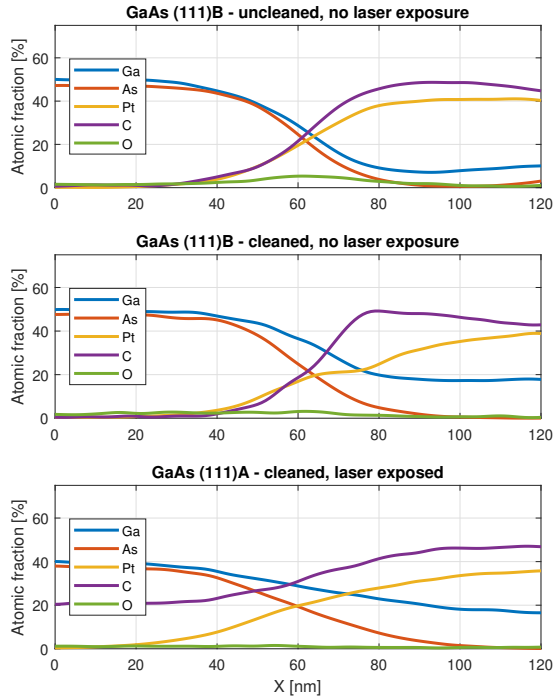


Figure 2.A2: EDX TEM results on cross sections of GaAs (111) samples. Prominent elements are Ga and As from the GaAs and the Ga ion beam used to prepare the TEM lamellae, Pt and C from the precursor used to grow a protective layer on the surface in lamella preparation, and O from sample oxidation. The uncleaned sample (top pane) shows a visible oxygen peak above the background that is not present for the surfaces treated with ammonium hydroxide, from which we conclude the procedure is effective in removing the oxide of GaAs.

a blast of nitrogen, and immediately loaded into the SEM vacuum. The GaAs chips are positioned on an ITO covered glass slide, which is in turn mounted on an aluminium holder.

EDX TEM measurements have been performed to measure the efficacy of the oxide removal procedure. To this end, GaAs chips are treated and then either loaded directly into a dual beam SEM, or laser exposed in the USEM system before transfer to the dual beam for fabrication of TEM lamellae. The process is to cover the GaAs with a layer of platinum through electron and ion beam induced deposition to protect the surface and prevent further oxide growth, followed by focussed ion beam (FIB) milling to obtain lamellae. These are then transferred to a TEM sample holder. Lamellae are also cut from an untreated, uncleaned chip. The lamellae are examined in the TEM by scanning a focussed beam across the GaAs-Pt interface and recording the EDX spectra along this line. Figure 2.A2 shows the elemental composition fitted from these spectra along a cross section. From these plots we conclude that only the uncleaned sample has an oxygen peak at the GaAs-Pt interface while this peak is absent in treated samples. This indicates

the procedure is effective and oxygen content on the GaAs surface is reduced to a level no longer measurable.

2.A3. Particle tracing simulations

The SE collection efficiencies are calculated using charged particle tracing in COMSOL Multiphysics. In our LISE images, the laser is incident from the upper right corner and the detector, an Everhart-Thornley detector (ETD) biased at 250V, is positioned on the upper side of the image. Electrons in the simulation are released 1 μm from the sample surface, which has a Gaussian potential distribution measuring 75 x 150 μm full width half maximum. We represent the ETD by a sphere biased at 250 V (see figure 2.A3) and record what fraction of electrons reaches this detector. Initial electron velocities are set to obey the Lambert cosine law for their direction and to have energies drawn from the Weibull distribution shown in figure 2.A4, closely following the SE spectrum of silicon generated by the simulation software Gean4. We ignore a potential change in SE yield as a result of the induced surface voltage, which suffices for making a qualitative comparison with the obtained experimental images. Electric fields are computed in 3D with the electrostatics interface in the first simulation step (figure 2.A3a), and particles are then traced through this field with the charged particle tracing interface in the next step (figure 2.A3b). A parameter sweep is conducted varying the SE release position relative to the location with surface potential as well as the intensity of the surface potential, and it is recorded what fraction of released particles reach the detector. We neglect Coulomb interactions between electrons and also ignore re-emission when electrons hit a surface. Thus, we do not include the contribution of SEs generated by backscatter electrons, often denoted as SE3s [4], to the total SE signal. This means that the proportional change in collection efficiency is smaller in reality than in the simulations.

Validation of our model by measuring the surface potential in situ during laser exposure is not possible as our USEM is not equipped with metrology equipment such as a kelvin probe or an advanced electron spectrometer to accurately measure the surface potential. Hence, we test the validity of our model by performing simulations and experiments with an added varying stage bias, which is expected to be a very influential parameter to the existence of the dipolar effect as it too has great influence on electron reabsorption and impact on the pole piece. Figure 2.A5 shows a comparison of the simulated and experimentally found cross section of the dipolar effect, broken down into positive and negative stage biases. We observe the following trends between them. For negative stage biases, the dipolar effect loses intensity for increasing bias voltage, but remains visible in the entire range. As the total number of detected SEs also drops with increasingly negative stage bias, a decreased modulation is in line with expectations. A positive stage bias promotes reabsorption of SEs in the sample, and for both simulation and experiment, the split completely disappears. At 5V, the simulations even predict a dip, which would fit as the added local potential results in increased absorption, but in the experiment there seemingly is an additional effect causing a marginal increase in the SE yield. The lower experimental values for the modulation compared to simulation are at least in part explained by the background of SE2 and SE3 signal on the experimental data, which may comprise over half the total SE signal [4]. Additionally, the surface potential could be lower than the simulated 200 mV. Thus, while the results do not exactly overlap, simulation and

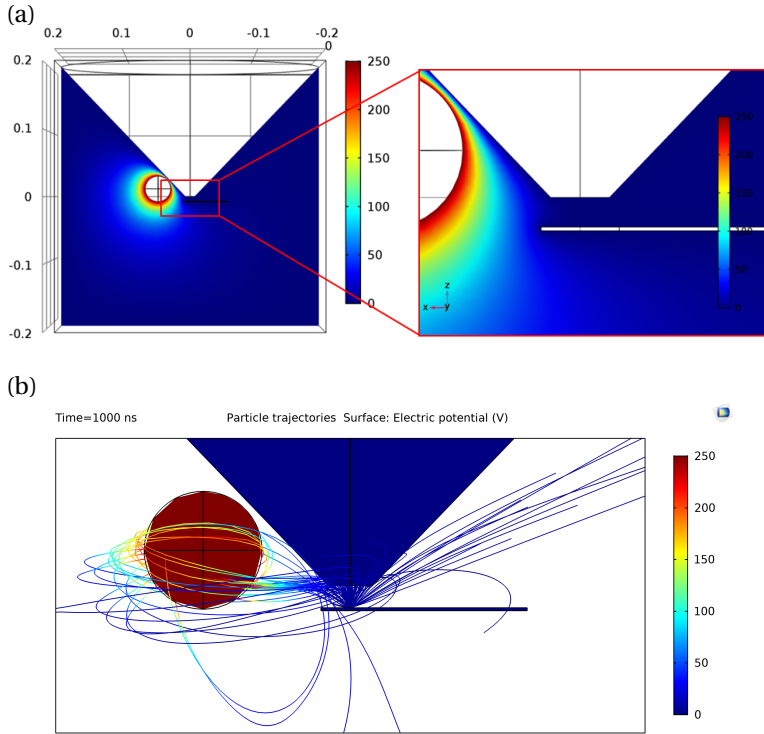


Figure 2.A3: Geometry for the COMSOL simulation of the SE collection efficiency with calculated potential in Volts. The sphere on the left represents the ETD, and the cone and flat surface represent the EM pole piece and sample holder. (a) The field of the ETD hardly protrudes below the pole piece and therefore a surface potential could be very relevant in this area. (b) Particles are traced through the electric field and we record the fraction reaching the detector. Colours indicate component voltage or particle kinetic energy.

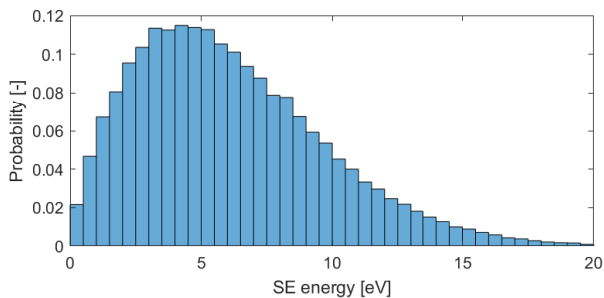


Figure 2.A4: Distribution of the initial energy of released electrons in the particle tracing simulations. It is a Weibull distribution with $a=6.897$ and $b=1.742$, and closely follows the SE spectrum of silicon.

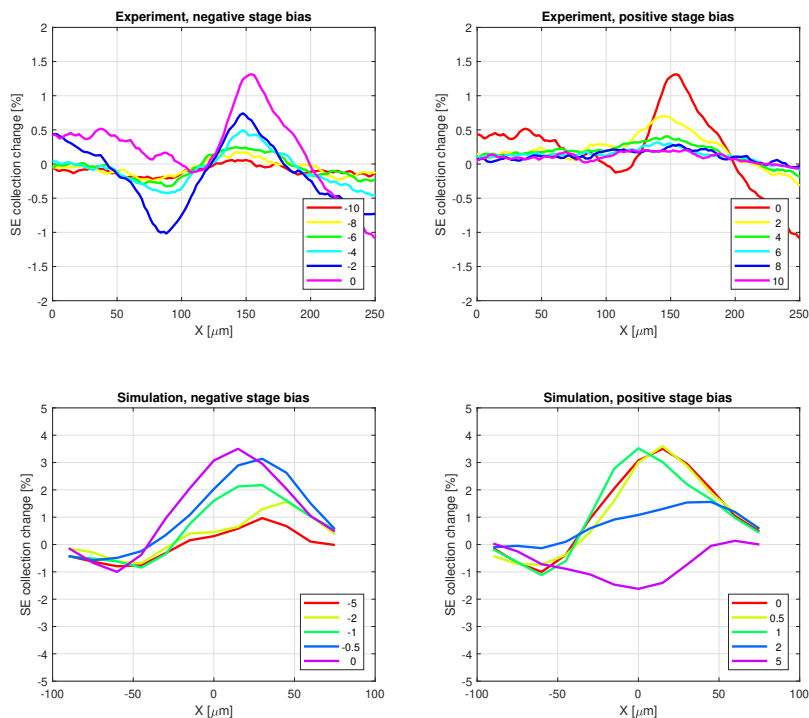


Figure 2.A5: Comparison of simulated and experimentally found cross sections of dipolar effect with a stage bias. All percentages relative to SEs collected at 0V stage bias. Simulation done for 200 mV surface potential. Similar trends are observed between simulation and experiment, supporting the notion of a local surface potential. The higher modulation on the simulated profiles compared to experimental data can be attributed to a lower surface potential being present on the sample and/or background of SE3 not considered in the simulation.

experiment show very similar developments for both polarities, which is impressive given that our model has numerous assumptions and supports the notion of the dipolar effect being caused by a local photo-induced surface potential.

2.A4. Retarding field analyser

In order to verify the surface potential on the sample is indeed small, we analyse the SE spectrum with a retarding field analyser (RFA) consisting of a single curved grid covering the GaAs sample chip as schematically represented in figure 2.A6. A variable retarding field is created by applying a voltage between the grid and the GaAs sample, preventing secondary electrons with an energy less than the RFA voltage determined cut-off energy from being detected. So called S-curves are measured by recording the transmitted SE signal as a function of the RFA voltage. In the presence of a surface potential, SE energy changes and the s-curves are shifted by the surface voltage. Based on a distance from

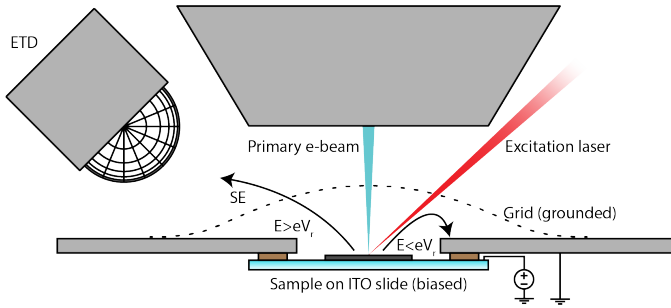


Figure 2.A6: Schematic representation of the retarding field analyser. A retarding field is applied between the sample and the grid by biasing the sample, filtering electrons based on energy and preventing detection of low energy electron. S-curves are constructed by measuring the ETD signal as a function of the retardation voltage.

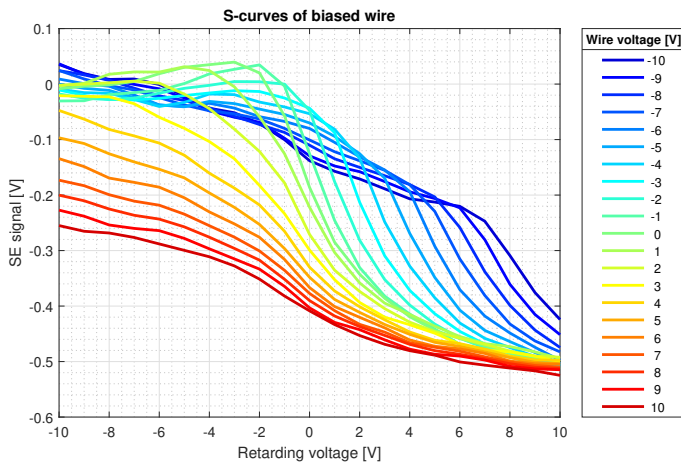


Figure 2.A7: RFA calibration measurements on a biased wire. The functioning of our retarding field analyser has been tested on a thin wire (32 AWG) with a known potential suspended right above the substrate. S curves were measured for different wire bias voltages to find the system response for a surface potential. From these measurements we conclude the SE spectrometer is sensitive enough for measuring surface potentials of a few V.

sample to grid of 4 mm and a mesh size of 0.5 mm, the cut-off energy varies by 0.25 eV within a grid opening, putting a limit on the resolution of the spectrum analyser. The RFA only measures a the directional component of the electron energy normal to the grid, and the grid is not necessarily perpendicular to the SE escape trajectories; this forms a further error contribution. While the RFA is therefore not sufficiently advanced to resolve a 200 meV energy difference with a high degree of certainty, calibration measurements showed that a 5 V potential (as found by ref [5]) certainly would be visible (see also figure 2.A7). The RFA measurements on GaAs can therefore be used to find an upper limit to the surface potential.

References

- [1] N. A. Torkhov, “Formation of a native-oxide structure on the surface of n-GaAs under natural oxidation in air”, *Semiconductors* **37**, 1177–1184 (2003).
- [2] P. Moriarty and G. Hughes, “An investigation of the early stages of native oxide growth on chemically etched and sulfur-treated GaAs(100) and InP(100) surfaces by scanning tunnelling microscopy”, *Ultramicroscopy* **42-44**, 956–961 (1992).
- [3] H. J. Yoon, “The study of native oxide on chemically etched GaAs (100) surfaces”, *Journal of The Electrochemical Society* **139**, 3229 (1992).
- [4] L. Reimer, “Emission of Backscattered and Secondary Electrons”, in *Scanning electron microscopy* (Springer Berlin Heidelberg, Berlin, Heidelberg, 1998), pp. 135–169.
- [5] G. Irde, S. M. Pietralunga, V. Sala, M. Zani, J. M. Ball, A. J. Barker, A. Petrozza, G. Lanzani, and A. Tagliaferri, “Imaging photoinduced surface potentials on hybrid perovskites by real-time Scanning Electron Microscopy”, *Micron* **121**, 53–65 (2019).

3

High-NA Ultrafast Scanning Electron Microscopy

Ultrafast scanning electron microscopy images carrier dynamics and carrier induced surface voltages using a laser pump electron probe scheme, potentially surpassing all-optical techniques in probe resolution and surface sensitivity. Current implementations have left a four order of magnitude gap between optical pump and electron probe resolution, which particularly hampers spatial resolution in the investigation of carrier induced local surface photovoltages. Here, we present a system capable of focusing the laser using an inverted optical microscope built into an ultrafast scanning electron microscopy setup to enable high numerical aperture pulsed optical excitation in conjunction with ultrafast electron beam probing. We demonstrate an order of magnitude improvement in optical pump resolution, bringing this to sub-micrometer length scales. We further show that temporal laser pump resolution can be maintained inside the scanning electron microscope by pre-compensating dispersion induced by the components required to bring the beam into the vacuum chamber and to a tight focus. We illustrate our approach using molybdenum disulfide, a two-dimensional transition metal dichalcogenide, where we measure ultrafast carrier relaxation rates and induced negative surface potentials between different flakes selected with the scanning electron microscope as well as on defined positions within a single flake.

3.1. Introduction

Four-dimensional or ultrafast scanning electron microscopy (USEM) has in recent years been pioneered as a promising technique to study temporal dynamics in nanostructured materials with electron beam resolution [2, 3]. In USEM, a pulsed laser beam excites (or pumps) the sample while a pulsed electron beam, scanning the sample at a fixed

This chapter has been published as M. W. H. Garming, I. G. C. Weppelman, M. Lee, T. Stavenga, and J. P. Hoogenboom, "Ultrafast scanning electron microscopy with sub-micrometer optical pump resolution", [Applied Physics Reviews](#) **9**, 021418 (2022)

delay with respect to the laser pulse, probes the material response with high resolution [4, 5]. The majority of reports to date have targeted the imaging of semiconductor carrier dynamics, creating carriers through fs laser excitation and tracking them with electron probe pulses through a carrier induced change in secondary electron signal. Materials and specimens whose charge carrier dynamics have been studied with USEM to date include bulk samples of silicon of various doping [6–8], GaAs [9], CdSe [3, 10] and alumina [11]. The impressive surface sensitivity of USEM enabled by the detection of low-energy secondary electrons also allows for resolving the influence of surface termination on carrier dynamics, as demonstrated on CdTe [12] and GaAs [13]. In addition, the change in surface potential induced by the presence of photo-excited free charge carriers, can be simultaneously measured with USEM through the local influence of this surface potential on the secondary electron (SE) trajectories and thereby SE collection efficiency [11, 13].

USEM is unique in its combination of direct electron beam microscopy, ultrafast carrier dynamics imaging, surface sensitivity, and surface photovoltage measurement. All-optical transient absorption techniques are traditionally used to measure charge carrier dynamics [14, 15], but are limited by light optical diffraction, and the large penetration depth of photons may lead to reduced contrast from thin samples or surface layers. In addition, sensitivity to induced surface photovoltages is lacking. Surface potentials can be measured with Kelvin probe force microscopy [16], but the scanning probe may be difficult to combine with electron beam imaging of the sample. Time-resolved scanning tunneling microscopy (STM) is another interesting technique capable of surface inspection at high spatial resolution on the ultrafast time scale [17], but also without the electron beam aiding in the selection of measurement areas. Time-resolved photoemission electron microscopy (TR-PEEM) has a similar contrast mechanism and, thus, thin-layer sensitivity as USEM [18, 19], but uses high-energy (UV) photons instead of the probing focused electron beam.

In current implementations of USEM, the optical pump resolution is on the order of tens of micrometers, leaving a four order of magnitude gap in resolution compared to the electron pulse beam [20, 21]. Most USEM setups are based on a scanning electron microscope (SEM) setup, often a commercial system, that is modified to accommodate fs-laser excitation of the sample and a pulsed electron beam [3, 22, 23]. Pulsing the electron beam is typically done by applying a scheme where the electron emitter is photo-excited to generate electron pulses [24, 25]. Photo-excitation of the sample is achieved with an optically transparent window in the vacuum chamber with a lens on the air side to focus the laser on the sample from the same side as the incoming electron beam [20]. This enables focusing the laser on samples for pumping, albeit with a large distance between a lens and a sample and, therefore, a very small numerical aperture (NA) that constitutes a limitation for achievable optical resolution.

Better focusing of the laser has the potential of greatly improving measurement resolution. As the spatial resolution for USEM measurements probing a semiconductor surface photovoltage (SPV) is limited by the size of the laser beam focus, and not the electron beam probe, it is useful to decrease the size of the laser spot in order to probe surface potentials over smaller areas. This would enable measuring on specific sections of samples and devices, rather than bulk wafers, and be particularly useful for measurement of 2D materials. In addition, for very small regions of interest, such as nanoparticles, reduction

in the laser spot size would have the added benefit of only exciting the measurement area without the risk of exposing and possibly modifying the surrounding area. In contrast, current implementations have targeted ensembles of nanoparticles all pumped at the same time [26–29]. Furthermore, a more tightly focused laser spot results in a higher power density; an improvement from a 30 μm spot to a diffraction limited sub-micrometer excitation area would entail roughly a thousand times higher laser fluence on the sample. An improvement in this magnitude would require the addition of (high-NA) optics in the SEM vacuum chamber, which may interfere with an electron beam and signal trajectories and add considerable dispersion to the laser pump pulse potentially compromising temporal resolution.

Here, we present a USEM setup with an integrated inverted optical microscope, utilizing high-NA microscope objective lenses akin to those used in conventional optical microscopes. By bringing all the optics inside the vacuum, the optical working distance is much lower than in the conventional case, and this enables sub-micrometer optical excitation and imaging of the sample, constituting a major step forward in resolution. The light optical objective lens is located below the sample [30, 31], such that it does not interfere with electron microscopy and allows investigation of nanoscale materials on transparent substrates. We show that spatial and temporal resolution can be maintained in the vacuum chamber by pre-compensating dispersion of a vacuum window (VW) and an objective lens, and demonstrate our high-NA USEM setup with ultrafast movies of carrier dynamics on thin molybdenum disulfide (MoS_2) flakes probing both selected individual flakes as well as specific locations within a single micrometer-scaled MoS_2 flake.

3.2. Experimental section

High-NA excitation is implemented in our SEM-based setup, as shown in figure 3.1, which also displays a typical state of the art USEM setup for comparison. The vacuum door and sample stage in a FEI Quanta 200 FEG microscope have been replaced with a custom built inverted optical microscope that accommodates conventional optical objectives. The sample holder, mounted on a piezostage, has an opening over which samples are mounted to ensure optical access. We previously used the integrated high-NA objective lenses for detection of e-beam induced cathodoluminescence [31–34]. Here, we add an optical excitation path to pump the sample with all components except for a mirror and the objective lens outside the vacuum chamber. The vacuum window facilitating this is a 10-mm-thick optical flat (CVI Melles Griot). Secondary electrons (SEs), forming the probe signal, are detected with an Everhart-Thornley detector (ETD) positioned in its standard configuration in the sample chamber.

The optical excitation path from the laser to the sample is shown in figure 3.2. The laser is a Coherent Vitara-T with 800 nm center wavelength and 95 MHz pulse repetition frequency. Sub-20 fs pulse duration is possible with the bandwidth at the widest setting of 125 nm. All optical components, particularly the vacuum window and the objective, introduce frequency dispersion to our broadband optical pulses, causing temporal broadening. We compensate for this with a set of dispersion compensation mirrors, which allow us to add negative dispersion and retain an ultrashort pulse at the sample. Optical power is regulated with a neutral density filter and a combination of a rotatable half lambda

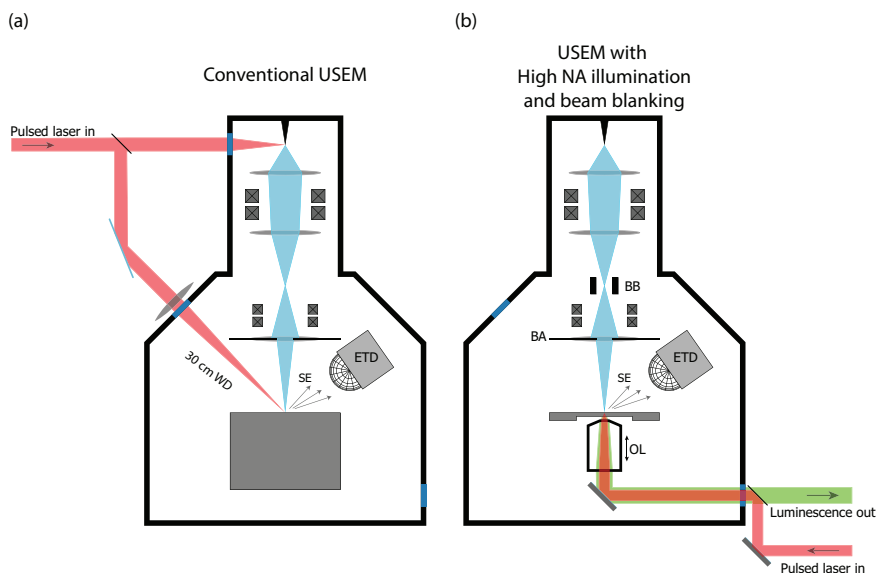


Figure 3.1: **Integrated inverted optical objective allows for high-NA pulsed laser excitation.** (a) Typical state of the art USEM setup with a laser triggered electron source. (b) High-NA USEM setup with a custom built inverted optical microscope for photoexcitation of the sample with high-NA objective lens (OL) at diffraction limited resolution. A beam blinder (BB) with blanking aperture (BA) is used, negating the need to (partially) direct the laser to the electron source for pulsing the electron beam. Secondary electrons are detected as the probe signal with an Everhart-Thornley detector (ETD).

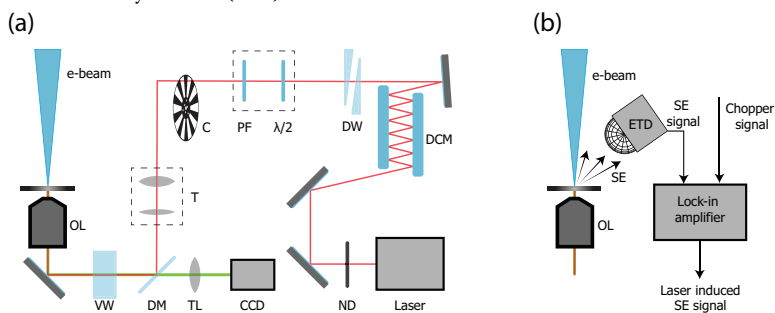


Figure 3.2: **Dispersion compensation optics are used in the excitation path and lock-in detection in the detection path.** (a) The pulsed laser beam (95 MHz, 800 nm) first goes through a neutral density filter (ND) to regulate power before entering dispersion compensation mirrors (DCMs) and dispersion wedges (DWs). Next are a half lambda plate ($\lambda/2$) and a polarization filter (PF) controlling power and polarization, beam chopper (C) for lock-in detection, 3.75:1 beam broadening telescope (T), dichroic mirror (DM), vacuum window (VW), and objective lens (OL). A tube lens (TL) and a CCD camera are used for imaging of the sample. (b) Lock-in detection is implemented by feeding the ETD signal to a lock-in detector to extract the laser induced SE signal from the total SE signal.

plate and a Brewster wedge based polarization filter. A beam expander with 3.75:1 ratio broadens the beam to fill more of the back aperture of objectives and make better use of their high NA; for these experiments, we use a Nikon 40x objective with 0.95 NA or a 40x

1.25 NA water immersion objective in combination with vacuum compatible immersion fluid. The path also contains a beam chopper for lock-in detection.

The laser-induced SE signal is modulated by the beam chopper periodically blocking the laser at a 940 Hz chopping frequency, which allows us to extract it from the total SE emission signal with a lock-in amplifier (figure 3.2). Thus, we do not need to use reference image subtraction [8, 35, 36], with the additional advantage of simultaneously visualizing processes slower than the pump-probe repetition time such as trapping of carriers [13]. Furthermore, in this way, we mitigate drift in the alignment or sample position between the recordings of reference and other images.

Electron beam blanking is used to pulse our electron beam, as detailed in ref [32]. Briefly, the continuous electron beam from a standard source is chopped by the beam blanker rapidly deflecting it over a blanking aperture. This solution of pulsing an electron beam predates the laser triggered source but has recently found more use in various forms [25, 37–39]. While some blanker designs have longer pulse durations than phototriggered sources [38], advantages include less invasive implementation in the microscope and improved stability during use as we are not sensitive to drift of the source vs the laser illumination. Furthermore, the laser power does not have to be divided between the electron source and sample. A pulse duration below 100 ps can be achieved at 4 kV acceleration voltage in our setup [32], with a linear relation between the pulse width and acceleration voltage. The use of a conjugate blanking scheme where the beam is focused between the blanker plates ensures that spatial resolution of the electron beam is preserved [32] and blanker induced spot displacement and blur is negligible [40]. We use a standard 5 Vpp square wave function generator to drive the beam blanker, resulting in an electron pulse for the rising and for the falling edge of the signal.

Accurate synchronization of the laser and electron pulses in time is crucial in achieving temporal resolution. As a beam blanking solution does not yield the same natural synchronization of the pulse repetition frequency as laser triggered sources do, we implemented an alternative procedure. As schematically represented in the block diagram in figure 3.3, electron pulses are locked to the laser pulse train by triggering the square wave generator driving the blanker plates with the signal of a photodiode exposed to the laser. A frequency divider halves the frequency of the triggering signal to account for the rising and falling edge of the square wave, ensuring the repetition frequencies of the laser and electron pulses are identical. Delays can be introduced to the triggering signal with a SRS DB64 coax delay box and fine adjustments in delay, and duty cycle can be made on the square wave generator itself.

Calibration of the pump-probe delay is based on a time correlated single photon counting (TCSPC) scheme. We use an avalanche photodiode (APD) to detect light emitted from the sample, and a PicoHarp 300 TCSPC timing unit to register the arrival time of photons relative to the photodiode signal. For this, we measure the electron-beam induced cathodoluminescence via the objective used for illumination and compare this signal to the arrival time of laser pulse reflections or second harmonic generation (figure 3.3). Zero time delay is found by adjusting the delay in the trigger signal for electron pulse generation such that the arrival time of the laser and CL light coincide. Some timing jitter is present in this scheme, for example, from the triggering of the pulse generators. However, pulse durations of 90 ps have been measured on this setup [32], forming an

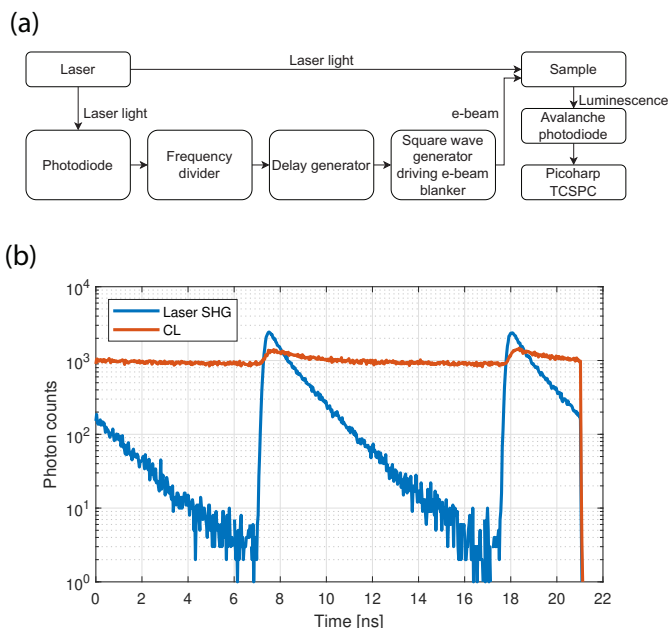


Figure 3.3: **Timing of the laser and electron pulses can be monitored with time correlated single photon counting (TCSPC), enabling sub-ns temporal alignment.** (a) Electron pulse generation is synchronized to the laser pulses by using a laser generated triggering signal on the square wave generator driving the blanker. The laser illuminates a photodiode, whose output signal is sent through a frequency divider and a delay generator before triggering the blanker signal generator. Pulse arrival times are monitored by measuring luminescence from the sample with an avalanche photodiode (APD) and a time correlated single photon counting unit. (b) Logarithmic arrival time histogram of electron beam generated cathodoluminescence and laser reflections measured with time correlated single photon counting. Pulse shapes are the result of a convolution between intrinsic pulse shape and the instrument response primarily determined by the APD and measurement circuit. The timing of the electron pulse generation is adjusted such that the electron beam and laser signals have the same arrival time.

upper limit to the jitter that is much smaller than the timescale of dynamics reported here.

An ultrafast movie is recorded by focusing the laser on the sample (fluence $\sim 2 \text{ mJ}/\text{cm}^2$), and scanning the photo-excited area with a 10 kV acceleration voltage pulsed electron beam. Typical pixel dwell times are on the order of 1 s, comprising many pump-probe cycles. We record the direct SE detector signal as well as the lock-in signal to reconstruct both the total SE signal and the laser induced component of it. The area is scanned multiple times with different pump-probe delays in random order to prevent misinterpretation of sample degradation as ultrafast dynamics. For more information on sample degradation resulting from prolonged exposure, we refer to the appendix.

The MoS_2 samples are prepared using mechanical exfoliation of naturally occurring bulk crystal (SPI) with tape followed by polydimethylsiloxane (PDMS) (Sylgard 184) stamping [41] on a substrate of ITO covered glass (Optics Balzers). We use two different samples, after stamping sample 1 goes through a cleaning procedure consisting of 1 h in anisole, 1

min in isopropylalcohol (IPA), drying with a blast of nitrogen, 2 h in vacuum oven at 200°C, and 4 min of oxygen plasma cleaning at 300 W with faraday cage. Sample 2 was prepared with the same stamping process, but the cleaning steps were omitted. Based on optical inspection, measured flakes are all many layers (tens of nm) thick, and therefore, their properties will resemble those of bulk MoS₂ [42]. In addition, we note that the thickness of the sample is much thinner than the optical penetration depth of MoS₂ at our 800 nm laser wavelength; the optical absorption is, therefore, in good approximation, constant over the sample thickness.

Spatial resolution of the pump laser is characterized using two-photon luminescence from an InP nanowire. The nanowire sample was prepared by transferring the wires (Bakkers lab, TU/e) from the growth substrate to an ITO slide with lint free tissue. The laser is focused on the sample, which is scanned through the laser spot on a piezostage while the second harmonic signal is recorded on an avalanche photodiode with a 400/40 bandpass filter. The laser spot size is determined from the resolution of the resulting second harmonic image.

Assessment of the temporal resolution of the pump laser is done by means of second order autocorrelation traces, from which the laser pulse duration can be determined [43, 44]. The autocorrelation traces are measured using a Michelson interferometer with a 100 μm thick Beta Barium Borate (BBO) crystal (Eksma optics) in the focus of the objective as a second harmonic generator. In the interferometer, the laser beam goes through a beam splitter and one pulse picks up a variable delay in an optical delay line. Both beams are subsequently recombined and focused on the BBO sample, whose second harmonic signal is measured using a photomultiplier tube. With the second harmonic signal intensity proportional to the square of the laser intensity (fourth power of the electric field), the second harmonic signal is up to eight times higher when the pulses overlap in time compared to when they arrive separately.

3.3. Results

3.3.1. Spatial and temporal optical probe size

The spatial extent of the laser pump profile is measured using the two-photon excited signal from an InP nanowire, see figure 3.4a-c. We fit a Gaussian profile (figure 3.4c) to a cross section of the second harmonic image (figure 3.4a) and extract 474 nm full width at half maximum (FWHM). We deconvolve this with the wire width (175 nm, figure 3.4b) and multiply by $\sqrt{2}$ to arrive at a laser spot size of about 620 nm FWHM with the 1.25 NA 40x water immersion objective. Thus, we conclude that we have reached sub-micrometer optical pump resolution.

The second order autocorrelation trace, measured to assess the laser pulse duration, was acquired with 125 nm laser bandwidth. Figure 3.4d shows the measured correlation function after 32 bounces of the incoming laser beam through the dispersion compensation mirrors. We retrieve a pulse duration of 15 fs on the sample. Thus, the ultrashort pulse duration can be retained despite the dispersion introduced by the objective lens and vacuum window. Consequently, the laser pulse duration will not limit the temporal resolution of the pump-probe scheme, and the efficiency of multi-photon processes, such as the generation of second harmonics used for the laser spot size characterisation, is

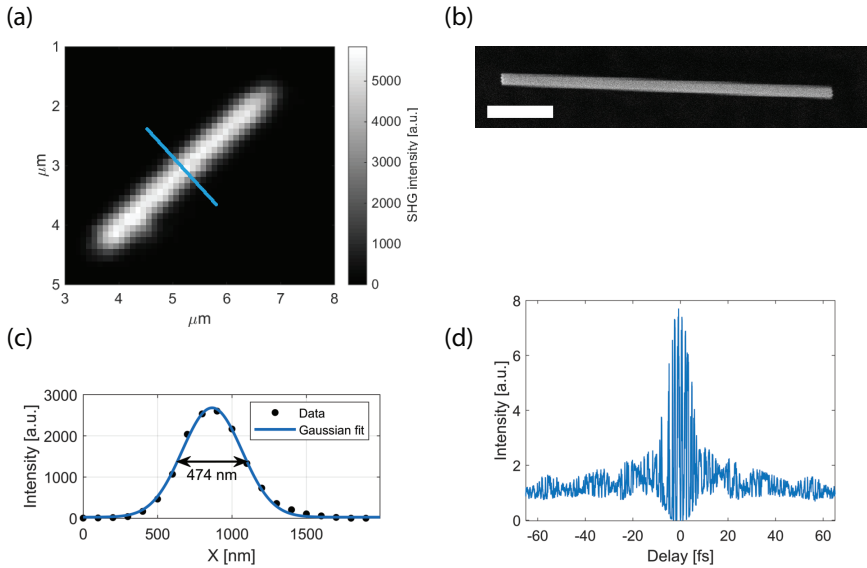


Figure 3.4: **620 nm spatial and 15 fs temporal optical pump resolution inside the ultrafast SEM.** (a) Two-photon excitation image of a 175 nm diameter InP nanowire acquired by scanning the nanowire through the laser spot. (b) SEM image of InP wire. (c) Cross section over the line in image (a) with Gaussian fit. The FWHM of the fit is equal to 474 nm, corresponding to a laser spot size of 620 nm in the focal plane. (d) Second order autocorrelation measured with a BBO crystal in the focal plane of the objective lens and with a laser bandwidth of 125 nm. Some higher order dispersion is visible in the trace with this high bandwidth, but the ratio of the peak to background is approximately 1:8 as expected, and we measure a 15 fs pulse duration after dispersion compensation. Scale bar is 1 μm .

maximized. Furthermore, the full toolbox of optical pulse shaping techniques and pulse train formation is available in the SEM vacuum.

3.3.2. Ultrafast dynamics

An ultrafast movie of the laser induced SE signal acquired with USEM on a single MoS₂ flake is shown in figure 3.5a. At 0 ns pump-probe delay, a dark spot and an adjacent bright spot are observed; a cross section of this dipolar profile is shown in figure 3.5b. A double Gaussian fit indicated as a guide to the eye is found to reproduce the data well. The transition between the minimum and maximum intensity of the fitted curve exhibits a 25-75 edge width of 750 nm, close to the above established resolution limit of our high-NA optical pump scheme.

For increasing pump-probe delay, the contrast gradually recedes until it has almost disappeared at -1 ns (equivalent to +9.5 ns at 95 MHz). The dark contrast is more intense compared to the brighter area. In figure 3.5c, contrast is plotted as a function of pump-probe delay, where data points show the mean of the five darkest pixels in the ultrafast movie frames after applying a $\sigma=2$ px Gaussian filter to the raw data and normalizing between -1 and 0. Fitting to an exponential decay $y = -\exp(-x/a)$ results in a 3.2 ns relaxation time constant. We note, however, that we observe rather large 95% uncertainty bounds for this fit of (2.4, 4.1) ns.

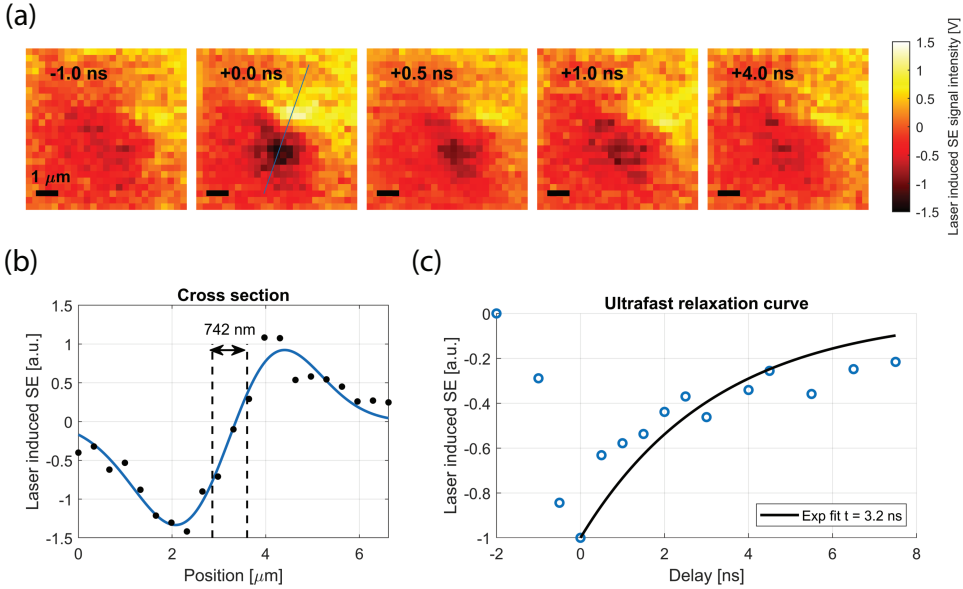


Figure 3.5: **Ultrafast scanning electron microscopy with sub-micrometer optical pump resolution.** (a) Ultrafast movie from an MoS₂ flake, showing SE contrast from the laser irradiated area as a function of laser pump - electron probe delay. A dark and bright spot reminiscent of a carrier-induced surface voltage is observed upon laser irradiation, which decays on a few ns time scale. (b) Intensity profile for the laser-induced SE signal at 0 ns delay over the line indicated in the corresponding panel in (a). The solid line shows a double Gaussian fit to the data revealing a 25-75 resolution of 750 nm. (c) Lock-in signal, i.e., laser induced SE signal as a function of the pump-probe delay. The single-exponential fit to the rising part of the curve yields a recovery time of 3.2 ns.

The above-mentioned result was obtained by pumping a sub-micrometer area on a MoS₂ flake tens of micrometers in size. We repeated this measurement on different areas of the same flake, thus showing how our high-NA USEM setup allows micrometer-scale site-selective excitation. Figure 3.6a shows an optical image of the examined flake while on the PDMS stamp, while figure 3.6b shows a SEM image of the same flake after deposition on the ITO-sample. The SEM image shows more flakes as the sample was stamped multiple times to deposit additional flakes. Region 2 indicates the area selected for recording the dynamics in figure 3.5. The additional areas are labeled as 1 and 3. These yield similar ultrafast movies with ns-scale dynamics with decay constants of 3.7 (2.9, 4.6) and 3.5 ns (2.3, 4.7) (figure 3.6c). When the data points are normalized and fitted together as shown in figure 3.6d a time constant of 3.5 (2.9, 4.0) ns is found. This is in agreement with the few ns lifetime reported in the literature for bulk MoS₂ based on transient absorption measurements, optical-pump THz-probe measurements, and first principles calculations of exciton lifetimes [45–47], and we, therefore, associate this decay with carrier recombination.

We next conducted additional measurements on different MoS₂ flakes on another sample in the experimental section referred to as sample 2. In order to expedite the measurements and focusing on the temporal information, we implemented a faster

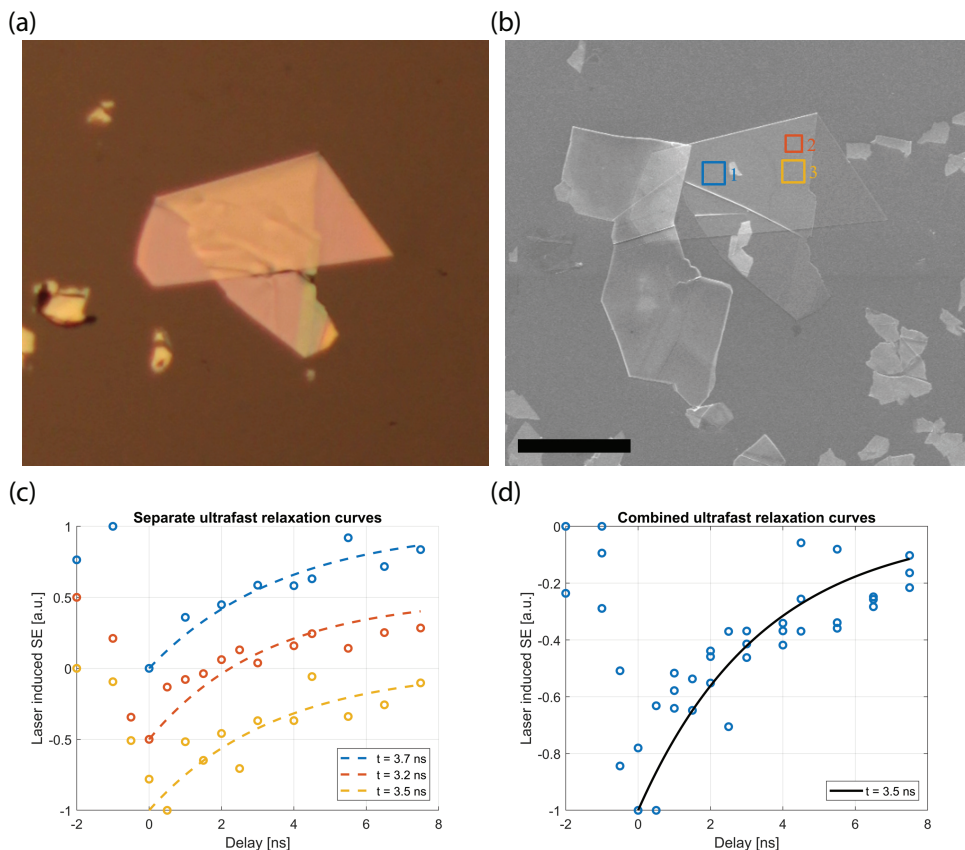


Figure 3.6: Localized sub-micrometer optical pump excitation on pre-selected areas within a single MoS₂ flake. (a) Optical image of an MoS₂ flake on PDMS stamp recorded during sample preparation and (b) an SEM image of the same flake after stamping on ITO coated glass. Marked regions have been selected for recording ultrafast movies. (c) Laser-induced SE signal from the areas marked in (b) as a function of delay time. Curves have been normalized and offset for clarity. Dashed lines indicate exponential fits with lifetimes indicated. (blue for region 1, red 2, yellow 3). (d) All data points combined into a single fit, showing 3.5 ns lifetime. Despite some variation in the individual curves, they collectively yield a lifetime value very close to the photoluminescence lifetime of bulk MoS₂. Scale bar in (b) indicates 50 μm .

acquisition scheme for recovering the ultrafast dynamics. Instead of recording full scan images like in figure 3.5, the electron beam is rapidly scanned over a 1 square micrometer area of the laser spot, and we record the 5 s average laser induced SE signal from the lock-in detector at every delay. We cycle through the delay settings four times and take the mean for each pump-probe delay to get a decay curve. This is done on four regions of interest on three different flakes. We find lifetimes of 2.2 (1.6, 2.7), 2.4 (1.5, 3.2), 3.8 (2.7, 4.8), and 2.9 (2.3, 3.5) ns (figure 3.7a). These values are in correspondence with the range of values observed for the previous sample. Combining the data points into a single fit (figure 3.7b) results in a 2.8 (2.4, 3.2) ns time constant. We conclude that we observe a spread in charge carrier lifetimes measured with USEM of about 2.2 ns to 3.8 ns both for

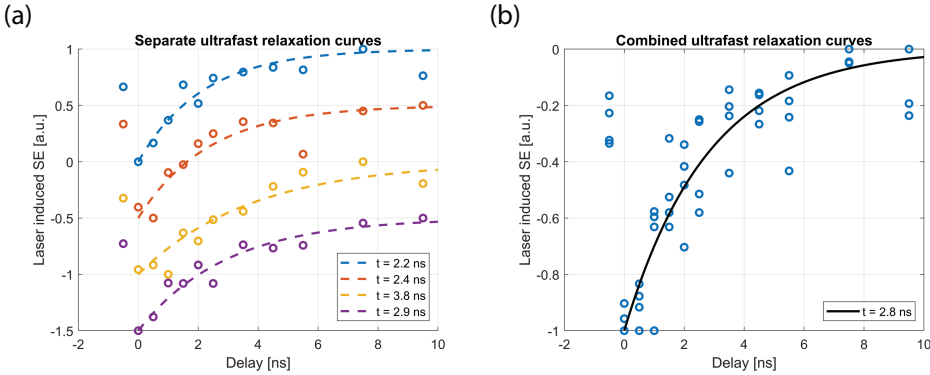


Figure 3.7: **Decay curves measured on multiple flakes consistently show ns-scale recovery.** (a) The decay curves of four separate regions on three different MoS₂ flakes of sample 2 all show ns scale recovery. The variation in fitted decay times spreads from 2.2 to 3.8 ns with mostly overlapping confidence bounds (see the text). (b) When combining the curves into a single fit, a lifetime close to the literature value emerges again.

measurements between different flakes as well as within single flakes, and that most of the uncertainty bounds are overlapping. As non-homogeneities can affect dynamics, we note that the measurement areas we selected on the flakes always appeared homogeneous in SEM and did not visibly overlap with edges or step variations in height, and contained no visible markings, scratches, or defects (see also figure 3.6b). Possibly, sample variations not visible in SEM imaging have still affected the measured lifetimes.

3.3.3. Dipolar USEM contrast pattern

We next turn our attention to the dipolar dark and bright contrast pattern observed in the USEM image sequence on MoS₂ (figure 3.5). We have previously shown on GaAs that carrier induced surface photovoltages (SPV) can result in such a dipolar contrast extending over a tens of micrometer laser pump size [13]. The process of forming this surface potential through band bending and its effect on SE yield of the sample is discussed in detail by Li et al. [48]. In addition to a yield change, a local surface potential influences SE trajectories, creating the dipolar patterns through the interplay between the SPV and asymmetry in the detector positioning [11, 13]. Both the surface potential and the voltage on the grid of the ETD (positioned north relative to the scanning direction in our setup and the image orientation in figure 3.5) affect the trajectory of low energy SEs; the surface potential can either collaborate with the ETD grid to guide SEs in the direction of the detector leading to a brighter than background contrast, or the surface potential negatively influences the local detection efficiency. This contrast then depends on the release position of the SEs relative to the SPV [11, 13].

We first confirm that the above interpretation of the dipolar contrast pattern also holds for sub-micrometer scale SPV areas. To this end, we conducted simulations in COMSOL using the electrostatics and particle tracing interfaces to fly particles through a 2D geometry representing the vacuum chamber. Particles are released 10 nm above the surface at various release positions around the surface potential with an energy distribution representing the SE spectrum of silicon and directions drawn from a 2D

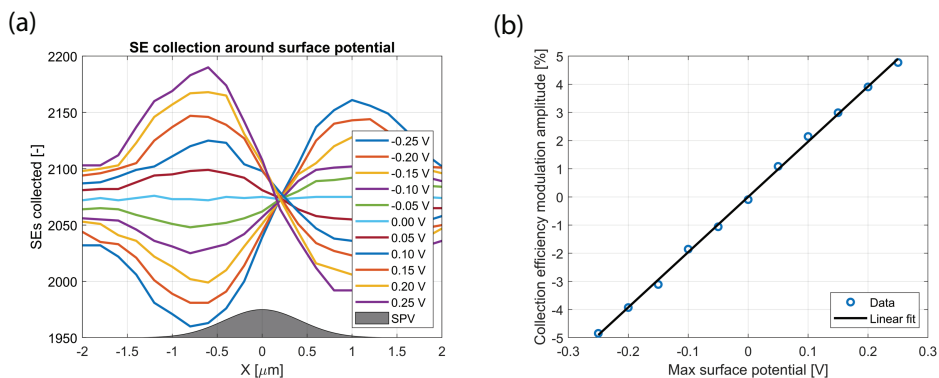


Figure 3.8: **Simulations show a micrometer-scale local surface potential can create dipolar USEM contrast patterns with intensity scaling linearly with voltage.** (a) Simulated number of electrons collected by the detector as a function of release position relative to the center of the surface potential, for varying surface potential voltages. Spatial extent of surface photovoltage shown in gray. The detector is positioned in the positive x direction. (b) Modulation amplitude in percent as a function of surface potential with linear fit.

Lambert cosine distribution. We record the number of electrons reaching the detector. The SE collection efficiency as a function of release position and SPV value is given in figure 3.8a. For all voltages, we see a dipolar pattern appearing that is similar in shape to what was found experimentally (figure 3.5), and in figure 3.8b, it is seen that the intensity of the dipolar profile scales linearly with the surface potential. Based on these results, we conclude that the measured dipolar pattern originates from a negative surface potential. We note that the appearance of a negative surface potential after MoS₂ carrier excitation is probably due to a thin carbon contamination layer formed on top of the MoS₂ after electron beam exposure (see also the appendix).

Based on the simulation results in figure 3.8, an estimate of the magnitude of the surface potential could be made, but we note that this would only constitute a coarse approximation for three reasons. First, we have assumed the intensity profile of the surface potential to follow that of the laser, i.e., Gaussian, but diffusion of carriers and saturation effects could lead to a more complicated spatial profile. Secondly, the simulation only takes into account the secondary electrons released at the primary beam position, the so-called SE1 electrons. In reality, backscatter electrons induce SE emission from other parts of the sample as well as other surfaces such as the pole piece and the vacuum chamber walls. These SE2 and SE3 contributions to the total SE signal do not have the same dependence on surface potential and, therefore, reduce the relative change in the total SE signal compared to the simulated SE1 signal by up to as much as a factor 3 [49]. Thirdly, the modelled SE energy spectrum, SE release direction, and geometry of the vacuum chamber are approximations. Therefore, to quantitatively measure the magnitude of the surface potential with USEM, calibration would be required. Without independent calibration, temporal variations in induced surface potential can be monitored thanks to the linear relation between the surface potential and SE signal modulation.

3.4. Conclusion

We have built and demonstrated a new implementation for USEM in which the sample is laser illuminated from below allowing for improved spatial pump resolution compared to existing implementations. We use dispersion compensation to retain ultrashort, tens of fs, laser pulses in the sub-micrometer focus of a high-NA optical objective. This narrows the gap between the laser optical and electron optical resolution in USEM, allowing us to probe fs-laser excitation induced surface photovoltages over areas as small as a few hundreds of nm in wide. Our laser illumination scheme is particularly suitable for thin or transparent samples, including nanoparticles that can be deposited on transparent substrates and 2D materials such as MoS₂, which we have used to demonstrate the capability of measuring high resolution ultrafast movies of carrier relaxation and carrier induced surface potential dynamics. The addition of an optical parametric oscillator (OPO) and pulse picker to the laser setup has the potential to further generalize the method to be applicable to high band gap materials and long recombination time semiconductors.

High-NA USEM enables single and sub-micrometer light optical pump scales, enhancing the possibilities for measuring carrier dynamics in nanostructured devices and materials. Further studies could, for instance, target sections of 2D materials with specific thickness, or measure across steps, defects, and junctions. The applicability to transition metal dichalcogenide (TMD) materials also provides the interesting prospect of evaluating (hetero)layered semiconductor devices. In addition, the use of conventional microscope objectives for excitation also makes it possible to combine USEM with optical imaging of the sample. Region of interest selection based on optical signals would be another possibility, as is further manipulation of the optical stimulation, e.g., with polarization control, super-resolution, and pulse shaping. This will further increase our possibilities for assessing photo-excited carrier dynamics in and around semiconductor nanodevices, ultimately aiding the optimization and development of novel tools, for example, for photodetection and photovoltaics.

References

- [1] M. W. H. Garming, I. G. C. Weppelman, M. Lee, T. Stavenga, and J. P. Hoogenboom, “Ultrafast scanning electron microscopy with sub-micrometer optical pump resolution”, *Applied Physics Reviews* **9**, 021418 (2022).
- [2] A. H. Zewail, “Four-dimensional electron microscopy”, *Science* **328**, 187–193 (2010).
- [3] O. F. Mohammed, D. S. Yang, S. K. Pal, and A. H. Zewail, “4D scanning ultrafast electron microscopy: Visualization of materials surface dynamics”, *Journal of the American Chemical Society* **133**, 7708–7711 (2011).
- [4] J. Sun, A. Adhikari, B. S. Shaheen, H. Yang, and O. F. Mohammed, “Mapping carrier dynamics on material surfaces in space and time using scanning ultrafast electron microscopy”, *Journal of Physical Chemistry Letters* **7**, 985–994 (2016).
- [5] G. M. Vanacore, A. W. P. Fitzpatrick, and A. H. Zewail, “Four-dimensional electron microscopy: Ultrafast imaging, diffraction and spectroscopy in materials science and biology”, *Nano Today* **11**, 228–249 (2016).

- [6] B. Liao, E. Najafi, H. Li, A. J. Minnich, and A. H. Zewail, “Photo-excited hot carrier dynamics in hydrogenated amorphous silicon imaged by 4D electron microscopy”, *Nature Nanotechnology* **12**, 871–876 (2017).
- [7] E. Najafi and A. Jafari, “Ultrafast imaging of surface-exclusive carrier dynamics in silicon”, *Journal of Applied Physics* **125**, 185303 (2019).
- [8] E. Najafi, T. D. Scarborough, J. Tang, and A. Zewail, “Four-dimensional imaging of carrier interface dynamics in p-n junctions”, *Science* **347**, 164–167 (2015).
- [9] J. Cho, T. Y. Hwang, and A. H. Zewail, “Visualization of carrier dynamics in p(n)-type GaAs by scanning ultrafast electron microscopy”, *Proceedings of the National Academy of Sciences of the United States of America* **111**, 2094–2099 (2014).
- [10] D. S. Yang, O. F. Mohammed, and A. H. Zewail, “Environmental scanning ultrafast electron microscopy: Structural dynamics of solvation at interfaces”, *Angewandte Chemie - International Edition* **52**, 2897–2901 (2013).
- [11] M. Zani, V. Sala, G. Irde, S. M. Pietralunga, C. Manzoni, G. Cerullo, G. Lanzani, and A. Tagliaferri, “Charge dynamics in aluminum oxide thin film studied by ultrafast scanning electron microscopy”, *Ultramicroscopy* **187**, 93–97 (2018).
- [12] A. M. El-Zohry, B. S. Shaheen, V. M. Burlakov, J. Yin, M. N. Hedhili, S. Shikin, B. Ooi, O. M. Bakr, and O. F. Mohammed, “Extraordinary carrier diffusion on CdTe surfaces uncovered by 4D electron microscopy”, *Chem* **5**, 706–718 (2019).
- [13] M. W. H. Garming, M. Bolhuis, S. Conesa-Boj, P. Kruit, and J. P. Hoogenboom, “Lock-in Ultrafast Electron Microscopy Simultaneously Visualizes Carrier Recombination and Interface-Mediated Trapping”, *Journal of Physical Chemistry Letters* **11**, 8880–8886 (2020).
- [14] N. Kumar, J. He, D. He, Y. Wang, and H. Zhao, “Charge carrier dynamics in bulk MoS₂ crystal studied by transient absorption microscopy”, *Journal of Applied Physics* **113**, 133702 (2013).
- [15] M. Yabuta, A. Takeda, T. Sugimoto, K. Watanabe, A. Kudo, and Y. Matsumoto, “Particle Size Dependence of Carrier Dynamics and Reactivity of Photocatalyst BiVO₄ Probed with Single-Particle Transient Absorption Microscopy”, *Journal of Physical Chemistry C* **121**, 22060–22066 (2017).
- [16] W. Melitz, J. Shen, A. C. Kummel, and S. Lee, “Kelvin probe force microscopy and its application”, *Surface Science Reports* **66**, 1–27 (2011).
- [17] S. Yoshida, Y. Arashida, H. Hirori, T. Tachizaki, A. Taninaka, H. Ueno, O. Takeuchi, and H. Shigekawa, “Terahertz Scanning Tunneling Microscopy for Visualizing Ultrafast Electron Motion in Nanoscale Potential Variations”, *ACS Photonics* **8**, 315–323 (2021).
- [18] L. Wang, C. Xu, M. Y. Li, L. J. Li, and Z. H. Loh, “Unraveling Spatially Heterogeneous Ultrafast Carrier Dynamics of Single-Layer WSe₂ by Femtosecond Time-Resolved Photoemission Electron Microscopy”, *Nano Letters* **18**, 5172–5178 (2018).

- [19] M. K. L. Man, A. Margiolakis, S. Deckoff-Jones, T. Harada, E. L. Wong, M. B. M. Krishna, J. Madéo, A. Winchester, S. Lei, R. Vajtai, P. M. Ajayan, and K. M. Dani, “Imaging the motion of electrons across semiconductor heterojunctions”, *Nature Nanotechnology* **12**, 36–40 (2017).
- [20] J. Sun, V. A. Melnikov, J. I. Khan, and O. F. Mohammed, “Real-space imaging of carrier dynamics of materials surfaces by second-generation four-dimensional scanning ultrafast electron microscopy”, *Journal of Physical Chemistry Letters* **6**, 3884–3890 (2015).
- [21] A. Adhikari, J. K. Eliason, J. Sun, R. Bose, D. J. Flannigan, and O. F. Mohammed, “Four-Dimensional Ultrafast Electron Microscopy: Insights into an Emerging Technique”, *ACS Applied Materials & Interfaces* **9**, 3–16 (2017).
- [22] M. Solà-Garcia, S. Meuret, T. Coenen, and A. Polman, “Electron-Induced State Conversion in Diamond NV Centers Measured with Pump-Probe Cathodoluminescence Spectroscopy”, *ACS Photonics* **7**, 232–240 (2020).
- [23] J. Zhao, O. M. Bakr, and O. F. Mohammed, “Ultrafast electron imaging of surface charge carrier dynamics at low voltage”, *Structural Dynamics* **7**, 021001 (2020).
- [24] B. Barwick, S. P. Hyun, O. H. Kwon, J. S. Baskin, and A. H. Zewail, “4D imaging of transient structures and morphologies in ultrafast electron microscopy”, *Science* **322**, 1227–1231 (2008).
- [25] S. Meuret, M. Solà Garcia, T. Coenen, E. Kieft, H. Zeijlemaker, M. Lätzel, S. Christiansen, S. Y. Woo, Y. H. Ra, Z. Mi, and A. Polman, “Complementary cathodoluminescence lifetime imaging configurations in a scanning electron microscope”, *Ultramicroscopy* **197**, 28–38 (2019).
- [26] R. Bose, J. Sun, J. I. Khan, B. S. Shaheen, A. Adhikari, T. K. Ng, V. M. Burlakov, M. R. Parida, D. Priante, A. Goriely, B. S. Ooi, O. M. Bakr, and O. F. Mohammed, “Real-space visualization of energy loss and carrier diffusion in a semiconductor nanowire array using 4D electron microscopy”, *Advanced Materials* **28**, 5106–5111 (2016).
- [27] R. Bose, A. Adhikari, V. M. Burlakov, G. Liu, M. A. Haque, D. Priante, M. N. Hedhili, N. Wehbe, C. Zhao, H. Yang, T. K. Ng, A. Goriely, O. M. Bakr, T. Wu, B. S. Ooi, and O. F. Mohammed, “Imaging Localized Energy States in Silicon-Doped InGaN Nanowires Using 4D Electron Microscopy”, *ACS Energy Letters* **3**, 476–481 (2018).
- [28] R. Bose, A. Bera, M. R. Parida, A. Adhikari, B. S. Shaheen, E. Alarousu, J. Sun, T. Wu, O. M. Bakr, and O. F. Mohammed, “Real-space mapping of surface trap states in CIGSe nanocrystals using 4D electron microscopy”, *Nano Letters* **16**, 4417–4423 (2016).
- [29] B. Liao, H. Zhao, E. Najafi, X. Yan, H. Tian, J. Tice, A. J. Minnich, H. Wang, and A. H. Zewail, “Spatial-temporal imaging of anisotropic photocarrier dynamics in black phosphorus”, *Nano Letters* **17**, 3675–3680 (2017).
- [30] A. C. Zonneville, R. F. C. Van Tol, N. Liv, A. C. Narvaez, A. P. J. Effting, P. Kruit, and J. P. Hoogenboom, “Integration of a high-NA light microscope in a scanning electron microscope”, *Journal of Microscopy* **252**, 58–70 (2013).

- [31] A. C. Narváez, I. G. C. Weppelman, R. J. Moerland, N. Liv, A. C. Zonneville, P. Kruit, and J. P. Hoogenboom, “Cathodoluminescence Microscopy of nanostructures on glass substrates”, *Optics Express* **21**, 29968 (2013).
- [32] R. J. Moerland, I. G. C. Weppelman, M. W. H. Garming, P. Kruit, and J. P. Hoogenboom, “Time-resolved cathodoluminescence microscopy with sub-nanosecond beam blanking for direct evaluation of the local density of states”, *Optics Express* **24**, 24760 (2016).
- [33] M. W. H. Garming, I. G. C. Weppelman, P. De Boer, F. P. Martínez, R. Schirhagl, J. P. Hoogenboom, and R. J. Moerland, “Nanoparticle discrimination based on wavelength and lifetime-multiplexed cathodoluminescence microscopy”, *Nanoscale* **9**, 12727–12734 (2017).
- [34] R. J. Moerland, I. G. C. Weppelman, M. Scotuzzi, and J. P. Hoogenboom, “Nanoscale Imaging of Light-Matter Coupling Inside Metal-Coated Cavities with a Pulsed Electron Beam”, *Nano Letters* **18**, 6107–6112 (2018).
- [35] E. Najafi, V. Ivanov, A. Zewail, and M. Bernardi, “Super-diffusion of excited carriers in semiconductors”, *Nature Communications* **8**, 15177 (2017).
- [36] B. Liao and E. Najafi, “Scanning ultrafast electron microscopy: A novel technique to probe photocarrier dynamics with high spatial and temporal resolutions”, *Materials Today Physics* **2**, 46–53 (2017).
- [37] N. C. MacDonald, G. Y. Robinson, and R. M. White, “Time-resolved scanning electron microscopy and its application to bulk-effect oscillators”, *Journal of Applied Physics* **40**, 4516–4528 (1969).
- [38] L. Zhang, J. P. Hoogenboom, B. Cook, and P. Kruit, “Photoemission sources and beam blankers for ultrafast electron microscopy”, *Structural Dynamics* **6**, 10.1063/1.5117058 (2019).
- [39] W. Verhoeven, J. F. M. van Rens, E. R. Kieft, P. H. A. Mutsaers, and O. J. Luiten, “High quality ultrafast transmission electron microscopy using resonant microwave cavities”, *Ultramicroscopy* **188**, 85–89 (2018).
- [40] L. Zhang, M. W. H. Garming, J. P. Hoogenboom, and P. Kruit, “Beam displacement and blur caused by fast electron beam deflection”, *Ultramicroscopy* **211**, 112925 (2020).
- [41] A. Castellanos-Gomez, M. Buscema, R. Molenaar, V. Singh, L. Janssen, H. S. J. Van Der Zant, and G. A. Steele, “Deterministic transfer of two-dimensional materials by all-dry viscoelastic stamping”, *2D Materials* **1**, 011002 (2014).
- [42] H. Wang, C. Zhang, and F. Rana, “Surface Recombination Limited Lifetimes of Photoexcited Carriers in Few-Layer Transition Metal Dichalcogenide MoS₂”, *Nano Letters* **15**, 8204–8210 (2015).
- [43] N. Accanto, J. B. Nieder, L. Piatkowski, M. Castro-Lopez, F. Pastorelli, D. Brinks, and N. F. Van Hulst, “Phase control of femtosecond pulses on the nanoscale using second harmonic nanoparticles”, *Light: Science and Applications* **3**, e143–e143 (2014).

- [44] M. Pawłowska, S. Goetz, C. Dreher, M. Wurdack, E. Krauss, G. Razinskas, P. Geisler, B. Hecht, and T. Brixner, “Shaping and spatiotemporal characterization of sub-10-fs pulses focused by a high-NA objective”, *Optics Express* **22**, 31496 (2014).
- [45] H. Shi, R. Yan, S. Bertolazzi, J. Brivio, B. Gao, A. Kis, D. Jena, H. G. Xing, and L. Huang, “Exciton dynamics in suspended monolayer and few-layer MoS₂ crystals”, *ACS Nano* **7**, 1072–1080 (2013).
- [46] J. H. Strait, P. Nene, and F. Rana, “High intrinsic mobility and ultrafast carrier dynamics in multilayer metal-dichalcogenide MoS₂”, *PHYSICAL REVIEW B* **90**, 245402 (2014).
- [47] M. Palummo, M. Bernardi, and J. C. Grossman, “Exciton radiative lifetimes in two-dimensional transition metal dichalcogenides”, *Nano Letters* **15**, 2794–2800 (2015).
- [48] Y. Li, U. Choudhry, J. Ranasinghe, A. Ackerman, and B. Liao, “Probing Surface Photovoltage Effect Using Photoassisted Secondary Electron Emission”, *J. Phys. Chem* **2020**, 5252 (2020).
- [49] L. Reimer, *Scanning Electron Microscopy*, 2nd ed., Vol. 45, Springer Series in Optical Sciences (Springer Berlin Heidelberg, Berlin, Heidelberg, 1998).

Appendix

3.A1. Dose dependence of contrast

As our previous work on carefully cleaned GaAs showed that a single atomic termination layer can drastically influence the formation of an surface photovoltage (SPV) [1], we speculated that the SPV on the MoS₂ flakes might originate from carbon contamination during the experiments. In our sample chamber with 10⁻⁶ mbar vacuum, electron beam deposition of contaminants cannot be ruled out, especially given the relatively high electron dose, the small scan area used, and the MoS₂ transfer process involving carbonaceous polymer stamps. To assess whether the SPV is intrinsic to the MoS₂ or related to electron beam induced deposition of contaminants, we compare the laser-induced SE signal measured around the photo-excited area with high and low current. This is done with a continuous electron beam and pulsed laser beam as the signal is stronger than from a pulsed electron beam; a continuous beam scan results in single frame containing all pump-probe delays, effectively the sum of an ultrafast movie. Where the contrast is overall positive for low current (50 pA), we see a dipolar effect for high current (2.5 nA) (figure 3.A1). Scanning the area of panel b with a 50 pA beam after high dose exposure also results in a dipolar contrast (panel c), a clear difference with panel a despite using the same current. This means that the contrast shape depends on the exposed cumulative dose rather than the current. Thus we conclude that the observed dipolar contrast pattern develops as a result of the electron exposure.

To rule out the possibility of net charging as a contribution to these changes in contrast pattern, we conducted an exposure series over a period of 15 hours, continuously scanning SE contrast images (Figure 3.A2). The dipolar contrast is visible from roughly 1 C/cm²

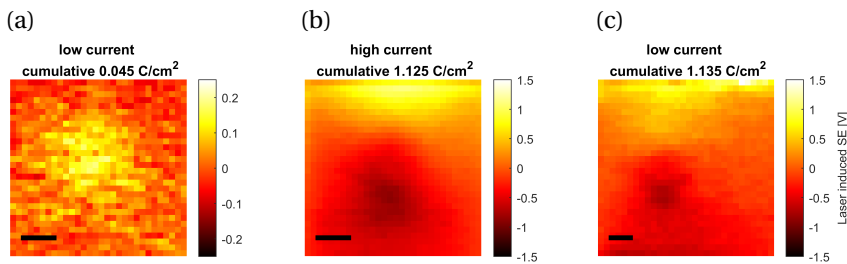


Figure 3.A1: **Measured MoS₂ USEM contrast pattern depends on accumulated electron dose.** (a) low-dose electron exposure of a laser pumped area results in a homogeneous brightening of the laser-irradiated area, whereas (b) high dose exposure leads to a dipolar contrast pattern. (c) Using the low current conditions of panel (a) on a previously irradiated area, also leads to a dipolar contrast pattern, showing it is the cumulative dose that determines the observed contrast pattern on MoS₂. Note that measurements in panels (b) and (c) were conducted on the same area on the same flake, while panel (a) was measured on a different flake. Scale bars 2 μm .

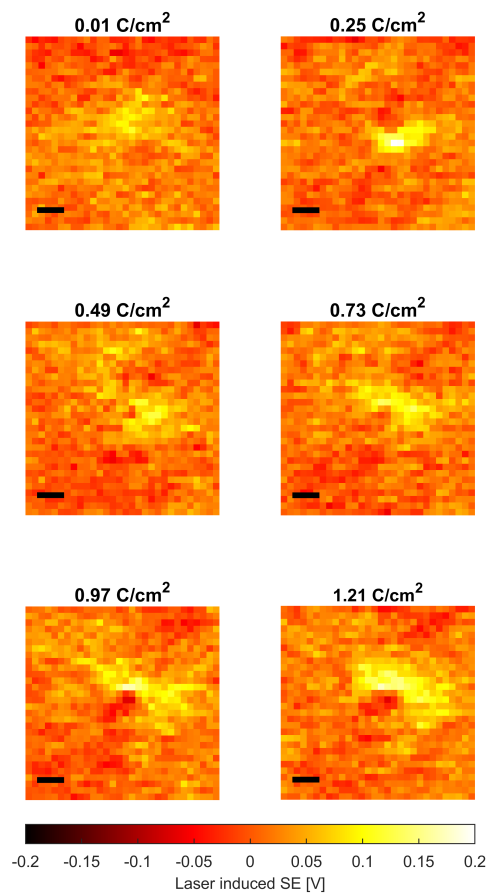


Figure 3.A2: **As the cumulative dose on the same measurement area increases, the contrast pattern evolves into a dipolar pattern.** By repeatedly measuring laser induced SE yield for a day, we can see how the contrast pattern changes with increasing dose. While the first measurement shows a bright spot, this gradually changes into a dipolar pattern. All measurements conducted with a pulsed laser and continuous electron beam as described in the main text. Scale bars 2 μm .

onwards, which corresponds to 12 hours of measurement at 50 pA. Given the observed time scale, we deem it unlikely that charging by the electron beam is the cause of the observed change in contrast. We note that we also observe a slight darkening of the exposed areas in SE images obtained after the USEM measurement, which is commonly associated with carbon deposition. Thus, we conclude that deposition of a thin layer of carbon on top of the MoS_2 flakes is the most likely explanation for the observed contrast change and occurrence of a SPV on MoS_2 . This means pre-exposure of samples is required to get reproducible measurement results, and reduce the influence of dose accumulated during measurement on the result. All areas on which the data shown in figures 3.5,3.6,

and 3.7 of the main text was acquired, were pre-exposed with a dose of at least 1 C/cm^2 . Thus, we also conclude that the ultrafast relaxation of charge carriers within the MoS_2 can still be measured, with the contamination layer contributing to the contrast observed in the image sequence.

References

- [1] M. W. H. Garming, M. Bolhuis, S. Conesa-Boj, P. Kruit, and J. P. Hoogenboom, “Lock-in Ultrafast Electron Microscopy Simultaneously Visualizes Carrier Recombination and Interface-Mediated Trapping”, *Journal of Physical Chemistry Letters* **11**, 8880–8886 (2020).

4

Imaging Resonant Micro-Cantilever Motion

Here, we demonstrate ultrafast scanning electron microscopy (SEM) for making ultrafast movies of mechanical oscillators at resonance with nanoscale spatiotemporal resolution. Locking the laser excitation pulse sequence to the electron probe pulses allows for video framerates over 50 MHz, well above the detector bandwidth, while maintaining the electron beam resolution and depth of focus. The pulsed laser excitation is tuned to the oscillator resonance with a pulse frequency modulation scheme. We use an atomic force microscope cantilever as a model resonator, for which we show ultrafast real-space imaging of the first and even the 2 MHz second harmonic oscillation as well as verification of power and frequency response via the ultrafast movies series. We detect oscillation amplitudes as small as 20 nm and as large as 9 μm . Our implementation of ultrafast SEM for visualizing nanoscale oscillatory dynamics adds temporal resolution to the domain of SEM, providing new avenues for the characterization and development of devices based on micro- and nanoscale resonant motion.

4.1. Introduction

Scanning electron microscopy (SEM) is characterized by resolutions capable of imaging deep below the optical diffraction limit and is, therefore, a fundamental tool for the inspection of nanoscale devices. SEM images have a highly desirable combination of resolution, depth of focus, and ease of interpretation of the data [2]. However, limited time resolution of SEM constrains their applicability to (quasi-)static samples. Long image scanning times of tenths of seconds at least, limited detector bandwidth, and low current in the electron beam are the factors limiting time resolution in conventional SEM [3]. The scan time limitation has been addressed with hyperspectral motion visualization

This chapter has been published as M. W. H. Garming, P. Kruit, and J. P. Hoogenboom, “Imaging resonant micro-cantilever movement with ultrafast scanning electron microscopy”, [Review of Scientific Instruments](#) **93**, 093702 (2022)

SEM, which analyzes frequency components in the secondary electron signal to gain information on the movement of the sample [4], but temporal resolution is still limited by detector bandwidth [3]. Ultrafast scanning electron microscopy (USEM), in which a sample is pumped and probed with ultrafast laser and electron pulses, respectively, in a stroboscopic fashion, has been developed to do SEM with time resolutions limited by laser and electron pulse duration [5].

USEM applications have focused on studying photo-excited charge carrier dynamics in semiconductors, measuring ultrafast lifetimes and diffusion of carriers in a multitude of materials [6–8]. Direct quantitative observation of the motion of micro- and nanoscale objects such as mechanical resonators has to our knowledge not yet been pursued despite their importance for sensing [9–16] and probe-based microscopy [17, 18], and the fact that SEM is routinely used for (static) quality inspection after fabrication. Optical interferometry is typically used to characterize micro- and nanomechanical resonators, but it has limited lateral resolution and the data acquired requires extensive analysis and interpretation [19, 20]. Ultrafast transmission electron microscopy (UTEM) has been used to measure non-resonant cantilever motion [21], and the movement of a resonant beam structure has been studied through the analysis of motion blur in images recorded with continuous beam transmission electron microscopy [22]. Further applications of UTEM have focused on measuring strain wave dynamics in thin materials [23, 24]. Combining the advantages of SEM with the temporal resolution required for dynamical imaging of high-frequency miniature resonators would enable direct real-space imaging and monitoring amplitude, phase, and frequency under resonant and non-resonant excitation.

Here, we present ultrafast movies of a single clamped beam resonator, an atomic force microscope (AFM) cantilever, performing real-space imaging of the fundamental resonance to demonstrate our approach. We determine the power dependency of the oscillation amplitude and run a frequency sweep to determine the resonator quality factor (Q-factor). Additionally, we capture the 2 MHz second harmonic oscillation, where USEM enables straightforward visualization of the mode shape while pushing the framerate to an effective 50 MHz.

4.2. Setup and method

Our USEM setup (figure 4.1a) is based on a commercial scanning electron microscope [7], which has been modified to enable pulsed beam operation through electron beam blanking [25] and to accommodate femtosecond laser excitation of the sample through an optical objective positioned below the sample in the vacuum chamber. The laser, a Coherent Vitara-T with 800 nm central wavelength and 95 MHz pulse repetition rate, is used in conjunction with a pulse picker based on a Conoptics Model 350-160 E-O Modulator. The pulse picker allows us to control the pulse repetition time and tune the laser excitation rate to the resonator we examine. For these experiments, we have used a NANOSENSORS PPP-NCHR 300 kHz AFM probe, for its trapezoidal cross section and aluminium coating on the detector side make it very suitable for photothermal excitation [26, 27]. In this process, laser pulses prompt local heating of the material and thermal expansion initiates a bending motion. The cantilever is mounted horizontally, rotated along the longitudinal axis such that the direction in which the tip points makes a 55 degree angle with the electron beam (see figure 1a inset). This makes the displacement of

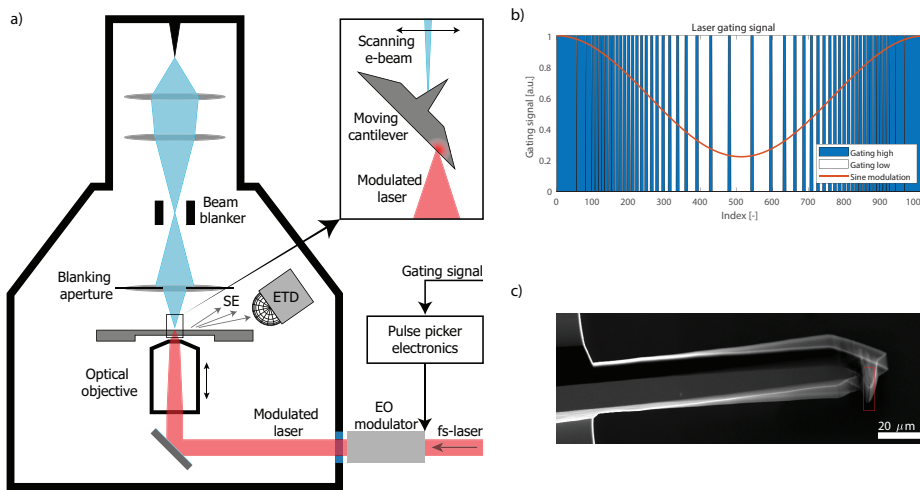


Figure 4.1: (a) Schematic for USEM on laser-excited resonant cantilevers. Electron pulses, illuminating the sample from above, are created using a beam blanker. The cantilever is excited using a fs-laser focused on the sample via an objective lens below the sample. Secondary electrons (SEs) are used as signal and are detected with an Everhart-Thornley detector (ETD). (b) The fs-laser excitation is modulated with a pulse frequency modulation (PFM) scheme, approximating sinusoidal excitation. We use the pulse sequence to gate the pump laser, resulting in periodic modulation of the laser power to get the cantilever into resonant motion. (c) SEM image of the cantilever recorded with a continuous electron beam while laser actuated near the cantilever base at its 316.71 kHz resonance frequency. A multi-micron amplitude motion is seen through motion blur, with the shape representing the fundamental mode. A detailed view of the region marked by the red box is found in figure 4.2.

the cantilever clearly visible in electron beam imaging.

The laser is focused on the back (detector) side of the cantilever (see figure 1a inset) through a Nikon objective with 10x magnification and an NA of 0.3. Through optical imaging of the laser spot on the sample, we focus the laser near the cantilever base to excite the first mode. A pulse frequency modulation (PFM) scheme is implemented to approximate sinusoidal excitation near the 300 kHz specified cantilever resonance frequency, which is much lower than the 95 MHz laser pulse repetition frequency. To this end, we operate the laser pulse picker in gated mode, and supply a 1024-character PFM sequence (figure 4.1b) to the gating input with a Thurlby Thandar Instruments TG1010A programmable function generator. Laser pulses are only transmitted when the gating input is high, and the PFM sequence is repeated to create periodic modulation. Continuous beam electron imaging easily identifies the resulting movement of the cantilever through motion blur (figure 4.1c). When the laser excites the cantilever at its resonance frequency of 316.71 kHz with 48 mW of laser power, we see a multi-micron displacement of the tip. The mode shape features a single node and antinode at the base and tip, respectively, indicating this is the fundamental frequency.

Electron pulses are generated by electron beam blanking, a scheme in which the electron beam travels between two blanker plates with an electric field between them that can deflect the beam over an aperture placed lower in the column. By rapidly switching the polarity of the blanker voltage and thereby the field direction, the beam is quickly

swept over the aperture, creating a sub-ns electron pulse during the brief moment the electron beam is directed through the aperture. Electron pulse generation is also triggered by the function generator, synchronizing the laser excitation and electron probing of the cantilever. Pulses as short as 90 ps have been demonstrated on our setup [25]. Longer pulses can be generated by switching the blaster voltage to zero to transmit the beam for as long as the desired pulse duration and then back to the original value to block the beam again. This flexibility in pulse duration offered by beam blanking can be useful as the current in the pulsed beam and consequently the acquired signal is directly proportional to the pulse duration, meaning that longer pulses can drastically shorten measurement times. We, therefore, adapt the pulse duration to the timescale of the dynamics measured, using either 20 ns or 100 ns pulse durations.

Ultrafast movies are constructed from stroboscopic images, recorded by scanning full images of the cantilever with a 10 kV pulsed electron beam and the modulated laser focused on the cantilever (figure 4.2a). As the laser excitation and electron beam probing are phase locked, the cantilever appears to be standing still and the resulting image looks like a regular SE micrograph. Upon completion of an image frame, a phase shift is added to the PFM signal in order to vary the point in the oscillation probed by the electron pulse. The next frame is scanned, showing the cantilever at another point in its oscillatory cycle (figure 4.2b), and this is repeated until the phase shifts cover the full 2π oscillation. All frames are combined into a video of the oscillatory movement, which constitutes our ultrafast movie.

4.3. Results

Stroboscopic imaging with a 20 ns pulsed electron beam allows for time resolved real-space imaging of the beam without significant motion blur. By sequentially acquiring frames and increasing the pump-probe delay in 88 ns steps between scans, we map the full oscillation period and combine the frames into an ultrafast movie of the beam vibration (see figure 4.2, multimedia view). Stroboscopic images recorded with two different delays between cantilever excitation and electron pulse generation are shown in figure 4.2a and b, where the cantilever is probed at different time points in the oscillation. Figure 4.2c shows sections of all recorded frames, with the image cropped to the AFM sensing tip for clarity. Difference images between frame zero, which functions as a reference, and the other movie frames can be seen in figure 4.2d. The tip moves away from its original position until maximum displacement is reached, at which point the tip returns to its starting point with good focus throughout the image sequence. Imaging with 100 ns electron pulses gives more motion blur, but is an option to reduce noise (see the supplementary material online [1]). Tip displacement relative to the reference frame is quantified using an image shift algorithm [28] (see figure 4.2e). A sinusoidal fit represents the data well and indicates a peak-peak amplitude of $5.0 \pm 0.2 \mu\text{m}$.

Power dependence of the oscillator amplitude is measured by successively recording ultrafast movies of the cantilever motion at various power levels ranging from 0 to 58 mW. We extract the displacement of the tip from the movie frames (figure 4.3a), and fit sinusoidal functions to obtain amplitude data. Figure 4.3b shows the amplitude as a function of laser power, with error bars indicating the fitting uncertainty. Amplitudes are lower than seen in figure 4.2, as we excited slightly off-resonance at 317 kHz to mitigate the

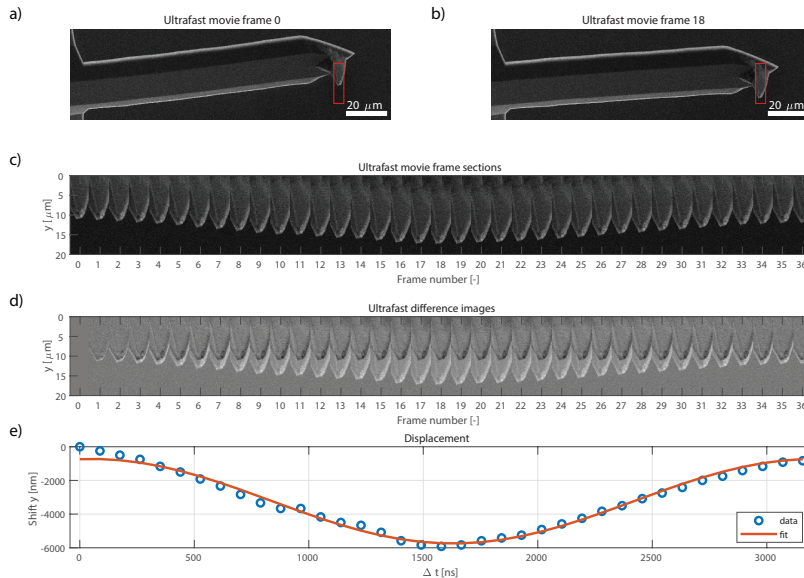


Figure 4.2: (a) Stroboscopic USEM images of an AFM cantilever are recorded with a pulsed electron beam locked to the laser frequency. The cantilever is excited with the laser and probed with electron pulses at 316.72 kHz. (b) By changing the phase delay (here 1585 ns with respect to (a)) between the cantilever laser excitation and electron pulse generation, stroboscopic images at different time points in the oscillation are recorded. (c) Multiple stroboscopic images are combined into an ultrafast movie of the motion of an AFM cantilever. Shown are sections of the movie frames cropped to the AFM sensing tip, marked by the red box in figures 4.2a and 4.2b. Each frame corresponds to a 88 ns step. (d) Difference images relative to a reference frame (frame 0, shown in (a)) show the position of the cantilever tip at various times during an oscillation cycle. (e) The tip displacement as a function of laser - electron pulse delay follows a sine curve with an amplitude of $5.0 \pm 0.2 \mu\text{m}$. (Multimedia view online [1])

effect of frequency drift between acquisition of different movies. We see a consistent trend of increasing amplitude with increasing laser power within the error margins. For low power the relation is linear, but a saturation effect is observed at high power as illustrated by linear and exponential fits, respectively. The linear fit includes the power levels up to 5.4 mW and yields $36 \pm 5 \text{ nm/mW}$ at this excitation frequency. Saturation at higher powers is attributed to non-linear dynamics of the cantilever itself that become non-negligible at high amplitudes [29, 30]. Cantilever amplitude strongly depends on laser focus and spot position, as well as the excitation frequency and cantilever type [27, 31]. Keeping in mind these possible variations, the measured linear relation at low power and the obtained slope are in line with those found in literature [32, 33], indicating that USEM can be a tool for investigating cantilever power response.

We next characterize the frequency response and Q-factor of the resonator by means of movies recorded with varying the excitation frequency at 42 mW laser power. Figures 4.3c and 4.3d show the amplitude and relative phase of the recorded oscillation as a function of

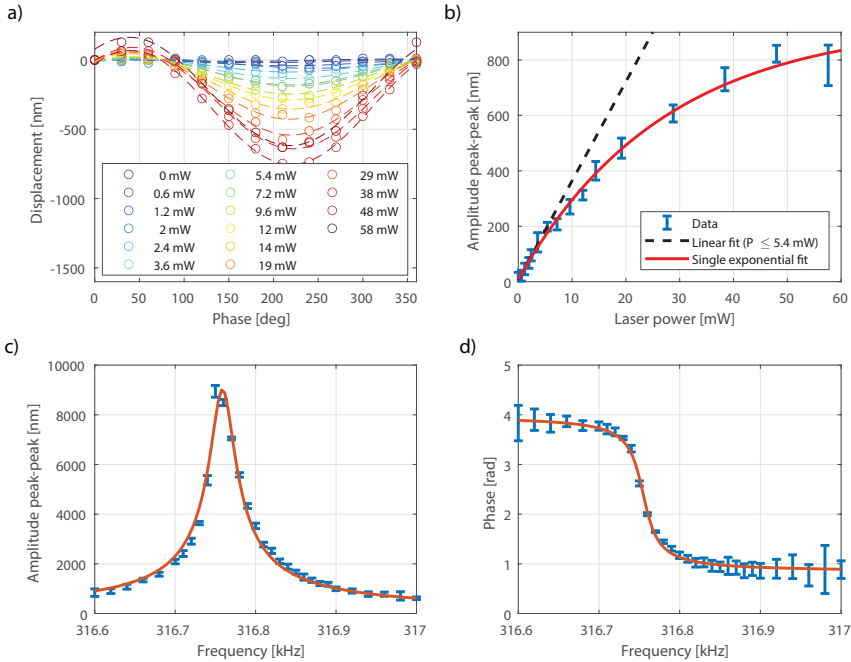


Figure 4.3: Power and frequency dependency of cantilever oscillation as characterized with USEM. (a) Displacement derived from ultrafast movies for the indicated range of excitation powers at 317 kHz driving frequency. (b) The oscillation amplitude increases linearly with laser power in the low power regime, but it saturates according to a single exponential function for exciting powers on the order of tens of mW. (c) Varying the excitation frequency shows a clear resonance peak at 316.75 kHz and (d) corresponding shift of π for the phase between laser modulation and cantilever motion. The resonator has a Q-factor of $1.1 \cdot 10^4$.

excitation frequency. The resonance frequency at 316.76 kHz is easily identifiable by the sharp increase in amplitude and a phase change of π centered at this frequency. Despite the high excitation power, fits based on theoretical relations valid for small actuation force and amplitude [34] mostly show agreement with the experimental data. The amplitude is fitted to a Lorentzian equation and the phase to an inverse tangent relation. We extract mutually corresponding Q-factors of $1.03 \pm 0.15 \cdot 10^4$ and $1.15 \pm 0.11 \cdot 10^4$ from fits to the amplitude and phase response, respectively. Furthermore, we notice the amplitude of the oscillation reaches a high peak value of $9 \mu\text{m}$, which brings imaging higher harmonic oscillations with reduced amplitude within reach.

Higher harmonic oscillations have a more complex mode shape as well as smaller amplitudes than the fundamental mode, adding to the utility of large depth of focus real-space imaging combined with high resolution of the electron beam that USEM offers. We excite the second harmonic by focusing the laser on the middle of the cantilever for optimum excitation efficiency [26, 31] with a power of 60 mW and a repetition frequency of 1.953,570 MHz and probe it with 20 ns electron pulses. An ultrafast movie of the oscillation was recorded and the dynamics visualized in figure 4.4 (multimedia view). The movie is constructed of 37 frames with 14 ns time steps, equivalent to a 70 MHz sampling

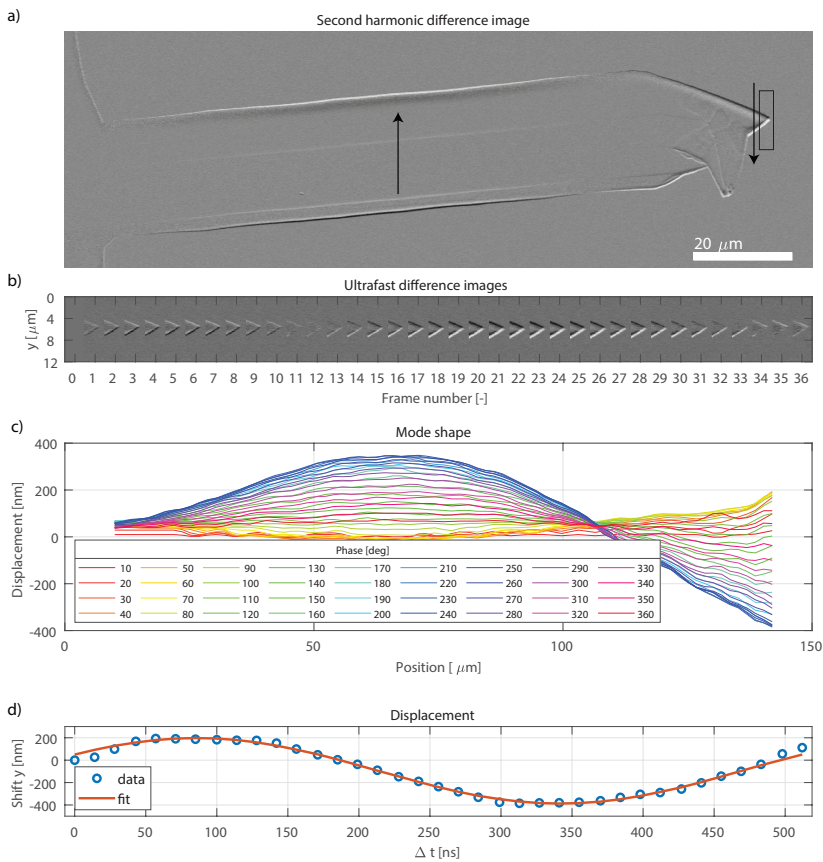


Figure 4.4: The combination of high resolution and focus depth allows for tracking the mode shape of the second harmonic in time over the full length of the cantilever. (a) Difference image between 230 and 50 degrees at second harmonic frequency showing movement in opposite direction at central part and tip of cantilever as indicated by the arrows. (b) Ultrafast difference images series of movement of cantilever tip (marked area in (a)). (c) Plotting the displacement as a function of position for all phases highlights the characteristic shape of the second harmonic. (d) The tip displacement over time is sinusoidal in shape with 590 nm amplitude. (Multimedia view online [1])

frequency; but with the 20 ns pulse duration we effectively imaged at 50 MHz. This rate exceeds the 10 MHz detector bandwidth, and it can be further improved if required by simply reducing the electron pulse duration.

Both the movie and the difference images in figures 4.4a and 4.4b give qualitative insight into the mode shape, featuring displacement of the cantilever near the middle with the tip moving in opposite direction. The quantitative displacement over the full length of the cantilever, determined by comparing individual columns of pixels in the

movie frames, is displayed in figure 4.4c. Displacement down to the tens of nm scale is well defined over the full cantilever length. The curve shapes clearly represent the second harmonic with a node at around 75% of the cantilever length from the base and an amplitude of a few hundred nanometers at the antinodes. Displacement of the tip over time (figure 4.4d) shows sinusoidal motion with 590 ± 20 nm peak-peak amplitude.

4.4. Conclusion

In conclusion, we have performed real-space time resolved imaging on a nanomechanical resonator at resonance, constructing ultrafast movies of a laser actuated cantilever with USEM. Large depth of focus allows for imaging the full cantilever in focus throughout the oscillation while the resolution is high enough to register displacement on the micro- and nanoscale. Moreover, the pulse duration can be selected to achieve high current to speed up acquisition or prioritize time resolution to image dynamics at rates beyond the detector bandwidth. Our work provides the prospect of real-space characterization and visualization of nanomechanical movement in MEMS resonators, aiding the development of new and bolstering our understanding of existing devices. Direct imaging of tip movement in close proximity to and interaction with a surface would be possible as is imaging nanomechanical cantilever mass sensors and other resonators exhibiting in-plane movement.

References

- [1] M. W. H. Garming, P. Kruit, and J. P. Hoogenboom, “Imaging resonant micro-cantilever movement with ultrafast scanning electron microscopy”, *Review of Scientific Instruments* **93**, 093702 (2022).
- [2] M. Henini, “Scanning electron microscopy: An introduction”, *III-Vs Review* **13**, 40–44 (2000).
- [3] A. H. Zewail, “Four-Dimensional Electron Microscopy”, *Science* **328**, 187–193 (2010).
- [4] T. Liu, J. Y. Ou, E. Plum, K. F. MacDonald, and N. I. Zheludev, “Visualization of Subatomic Movements in Nanostructures”, *Nano Letters* **13**, 46 (2021).
- [5] J. Spencer Baskin and A. H. Zewail, “Seeing in 4D with electrons: Development of ultrafast electron microscopy at Caltech”, *Comptes Rendus Physique* **15**, 176–189 (2014).
- [6] A. Adhikari, J. K. Eliason, J. Sun, R. Bose, D. J. Flannigan, and O. F. Mohammed, “Four-Dimensional Ultrafast Electron Microscopy: Insights into an Emerging Technique”, *ACS Applied Materials & Interfaces* **9**, 3–16 (2017).
- [7] M. W. H. Garming, M. Bolhuis, S. Conesa-Boj, P. Kruit, and J. P. Hoogenboom, “Lock-in Ultrafast Electron Microscopy Simultaneously Visualizes Carrier Recombination and Interface-Mediated Trapping”, *The Journal of Physical Chemistry Letters* **11**, 8880–8886 (2020).

- [8] M. W. H. Garming, I. G. C. Weppelman, M. Lee, T. Stavenga, and J. P. Hoogenboom, “Ultrafast scanning electron microscopy with sub-micrometer optical pump resolution”, *Applied Physics Reviews* **9**, 021418 (2022).
- [9] B. Arash, J. W. Jiang, and T. Rabczuk, “A review on nanomechanical resonators and their applications in sensors and molecular transportation”, *Applied Physics Reviews* **2**, 021301 (2015).
- [10] R. Abdolvand, B. Bahreyni, J. Lee, and F. Nabki, “Micromachined Resonators: A Review”, *Micromachines* **7**, 160 (2016).
- [11] L. Wei, X. Kuai, Y. Bao, J. Wei, L. Yang, P. Song, M. Zhang, F. Yang, and X. Wang, “The Recent Progress of MEMS/NEMS Resonators”, *Micromachines* **12**, 724 (2021).
- [12] G. Gruber, C. Urgell, A. Tavernarakis, A. Stavrinadis, S. Tepsic, C. Magén, S. Sangiao, J. M. De Teresa, P. Verlot, and A. Bachtold, “Mass Sensing for the Advanced Fabrication of Nanomechanical Resonators”, *Nano Letters* **19**, 6987–6992 (2019).
- [13] I. E. Rosłoń, R. J. Dolleman, H. Licon, M. Lee, M. Šiškins, H. Lebius, L. Madauß, M. Schleberger, F. Alijani, H. S. J. van der Zant, and P. G. Steeneken, “High-frequency gas effusion through nanopores in suspended graphene”, *Nature Communications* **11**, 6025 (2020).
- [14] M. Šiškins, M. Lee, S. Mañas-Valero, E. Coronado, Y. M. Blanter, H. S. J. van der Zant, and P. G. Steeneken, “Magnetic and electronic phase transitions probed by nanomechanical resonators”, *Nature Communications* **11**, 2698 (2020).
- [15] H. Hu, H. Cho, S. Somnath, A. F. Vakakis, and W. P. King, “Silicon nano-mechanical resonators fabricated by using tip-based nanofabrication”, *Nanotechnology* **25**, 10.1088/0957-4484/25/27/275301 (2014).
- [16] H. Fujita, “Microactuators and micromachines”, *Proceedings of the IEEE* **86**, 1721–1732 (1998).
- [17] B. Bhushan and O. Marti, “Scanning Probe Microscopy – Principle of Operation, Instrumentation, and Probes”, in *Springer handbook of nanotechnology* (Springer, Berlin, Heidelberg, 2010), pp. 573–617.
- [18] L. Gross, B. Schuler, N. Pavliček, S. Fatayer, Z. Majzik, N. Moll, D. Peña, and G. Meyer, “Atomic Force Microscopy for Molecular Structure Elucidation”, *Angewandte Chemie - International Edition* **57**, 3888–3908 (2018).
- [19] A. Barg, Y. Tsaturyan, E. Belhage, W. H. P. Nielsen, C. B. Møller, and A. Schliesser, “Measuring and imaging nanomechanical motion with laser light”, *Applied Physics B* **123**, 8 (2017).
- [20] S. J. Rothberg, M. S. Allen, P. Castellini, D. Di Maio, J. J. Dirckx, D. J. Ewins, B. J. Halkon, P. Muyschondt, N. Paone, T. Ryan, H. Steger, E. P. Tomasini, S. Vanlanduit, and J. F. Vignola, “An international review of laser Doppler vibrometry: Making light work of vibration measurement”, *Optics and Lasers in Engineering* **99**, 11–22 (2017).
- [21] D. J. Flannigan, P. C. Samartzis, A. Yurtsever, and A. H. Zewail, “Nanomechanical Motions of Cantilevers: Direct Imaging in Real Space and Time with 4D Electron Microscopy”, *Nano Letters* **9**, 875–881 (2009).

- [22] N. Lobato-Dauzier, M. Denoual, T. Sato, S. Tachikawa, L. Jalabert, and H. Fujita, “Current driven magnetic actuation of a MEMS silicon beam in a transmission electron microscope”, *Ultramicroscopy* **197**, 100–104 (2019).
- [23] Y. Zhang and D. J. Flannigan, “Observation of Anisotropic Strain-Wave Dynamics and Few-Layer Dephasing in MoS₂ with Ultrafast Electron Microscopy”, *Nano Letters* **19**, 8216–8224 (2019).
- [24] J. Hu, G. M. Vanacore, A. Cepellotti, N. Marzari, and A. H. Zewail, “Rippling ultrafast dynamics of suspended 2D monolayers, graphene”, *Proceedings of the National Academy of Sciences* **113**, E6555–E6561 (2016).
- [25] R. J. Moerland, I. G. C. Weppelman, M. W. H. Garming, P. Kruit, and J. P. Hoogenboom, “Time-resolved cathodoluminescence microscopy with sub-nanosecond beam blanking for direct evaluation of the local density of states”, *Optics Express* **24**, 24760 (2016).
- [26] M. Vassalli, V. Pini, and B. Tiribilli, “Role of the driving laser position on atomic force microscopy cantilevers excited by photothermal and radiation pressure effects”, *Applied Physics Letters* **97**, 10.1063/1.3497074 (2010).
- [27] D. Kiracofe, K. Kobayashi, A. Labuda, A. Raman, and H. Yamada, “High efficiency laser photothermal excitation of microcantilever vibrations in air and liquids”, *Review of Scientific Instruments* **82**, 013702 (2011).
- [28] M. Guizar-Sicairos, S. T. Thurman, and J. R. Fienup, “Efficient subpixel image registration algorithms”, *Optics Letters* **33**, 156 (2008).
- [29] C. van der Avoort, R. van der Hout, J. J. M. Bontemps, P. G. Steeneken, K. Le Phan, R. H. B. Fey, J. Hulshof, and J. T. M. van Beek, “Amplitude saturation of MEMS resonators explained by autoparametric resonance”, *Journal of Micromechanics and Microengineering* **20**, 105012 (2010).
- [30] J. Jahng, D. A. Fishman, S. Park, D. B. Nowak, W. A. Morrison, H. K. Wickramasinghe, and E. O. Potma, “Linear and Nonlinear Optical Spectroscopy at the Nanoscale with Photoinduced Force Microscopy”, *Accounts of Chemical Research* **48**, 2671–2679 (2015).
- [31] B. A. Bircher, L. Duempelmann, H. P. Lang, C. Gerber, and T. Braun, “Photothermal excitation of microcantilevers in liquid: effect of the excitation laser position on temperature and vibrational amplitude”, *Micro & Nano Letters* **8**, 770–774 (2013).
- [32] G. Gruca, D. Chavan, J. Rector, K. Heeck, and D. Iannuzzi, “Demonstration of an optically actuated ferrule-top device for pressure and humidity sensing”, *Sensors and Actuators A: Physical* **190**, 77–83 (2013).
- [33] Y. Miyahara, H. Griffin, A. Roy-Gobeil, R. Belyansky, H. Bergeron, J. Bustamante, and P. Grutter, “Optical excitation of atomic force microscopy cantilever for accurate spectroscopic measurements”, *EPJ Techniques and Instrumentation* **7**, 2 (2020).
- [34] H. J. R. Westra, “Nonlinear Beam Mechanics”, PhD thesis (Delft University of Technology, 2012), p. 16.

5

Development of a Laser Triggered Beam Blanker

Beam blankers are a practical solution to create pulsed electron beams for ultrafast electron microscopy (UEM), but conventional approaches face challenges in the areas of pulse duration and synchronisation of electron probe pulses to laser pump pulses. Laser triggered beam blankers, where the deflection field between blanker plates is rapidly altered through use of a photoconductive switch, offer the prospect of faster electron pulses whose generation is directly triggered by the laser for optimum pulse synchronisation. We present a design for a mm-sized laser triggered beam blanker making use of a commercially available photoconductive switch, with the goal of generating 10 ps electron pulses at 5 kV acceleration voltage. The design features a 60 micron plate separation and is sufficiently compact to be incorporated into a scanning electron microscope through the standard blanker port. We have constructed a working prototype and characterised the device with streak camera measurements, demonstrating both laser induced electron beam deflection and electron pulse generation. Our measured pulse duration is 530 ps, in close agreement with a calculated estimate based on the current experimental parameters. We discuss how the pulse duration can be further reduced to the 10 ps goal by modifying the laser pulse duration and repetition frequency.

5.1. Introduction

Ultrafast electron microscopy (UEM) has seen major development in recent years, revealing the dynamics of charge carriers, molecular vibrations, phase transitions, and more [1–3]. This is generally achieved by photo-exciting a specimen with a fs-laser to bring the sample out of equilibrium (pump), followed by an electron pulse to gauge the response (probe). For many applications, a multitude of these pump-probe cycles are required to build sufficient signal for an ultrafast measurement, where the time resolution is determined by the pulse duration [4]. These pulse durations can by now be well in the sub-ps range, with some reports of pulse durations below 1 fs [5–9]. Key to accessing

these ultrafast time scales is the development of electron sources capable of delivering ultrashort electron pulses.

The formation of ultrashort electron pulses for ultrafast electron microscopy has been demonstrated by employing photoemission sources and by means of beam blanking [10]. Photoemission sources use photoexcitation of the electron source to provide electrons with the energy needed to be extracted. While this facilitates very short pulses (sub-ps), it is an extensive modification to the microscope that makes switching between pulsed and continuous beam operation cumbersome, and needs frequent realignment of the laser on the tip. Beam blanking based UEM setups use a standard continuous high-brightness electron source in combination with a deflector that sweeps the beam over an aperture or slit to chop it [11–13]. Beam blankers generally provide longer electron pulses (tens of ps) than photoemission sources but are easier to implement and more straightforward to switch between continuous and pulsed operation [14]. Furthermore, this solution is very stable requiring no optical realignment, enabling very long acquisition times. Our goal is to combine the practical advantages of beam blankers with the time resolution of laser triggered sources.

5

Conventional beam blanker setups use a set of parallel plates with the electron beam in between, and an electronic square wave generator to modulate the voltage on the blanker plates by a few Volt and thereby switch the field between them [15]. As the field direction is switched, the beam is deflected over an aperture or slit lower in the column, forming an electron pulse during the brief moment the beam is positioned in the aperture and transmitted to the specimen. The resulting pulse duration is given by equation 5.1 where Φ is the electron acceleration voltage, α_{full} the full deflection angle required to sweep the beam over the aperture, dV/dt the time derivative of the blanker voltage, and d/L the ratio between blanker plate separation and plate length along the electron optical axis.

$$\tau_{pulse} = \frac{2\Phi\alpha_{full} d}{dV/dt L} \quad (5.1)$$

The faster the field can be switched, the shorter the pulse duration will be. The rise time of the electronic signal driving the blanker can be a limitation, but pulse generators with sub-100 ps rise time are commercially available [16]. Other solutions to obtain fast deflection of the electron beam include the use of a resonating microwave cavity recently demonstrated for TEM, where an oscillating field rapidly deflects the beam over an aperture to achieve an experimentally determined pulse duration of 750 fs [17, 18].

The natural synchronisation between laser pump and electron probe pulses offered by photocathode sources is absent for electrostatic beam blankers, which instead rely on a photodiode signal triggering an electronic pulse generator to synchronize laser and electron pulses [19]. This introduces jitter between the pulses, which can be on the tens of ps scale [16] and can limit the time resolution of UEM experiments even if pulse durations are shorter. Solutions are thus needed to reduce jitter in electron beam blanking.

Laser triggered blankers rely on an integrated photoconductive switch shorting the blanker plates for rapid change of the blanker voltage and electron pulse generation [20]. Their independence on the triggering of electronic pulse generators to prompt electron pulse generation eliminates the influence of their trigger jitter on UEM time resolution.

The RC time constant of the blanker is crucial for fast voltage switching and obtaining short electron pulses. Laser triggered blankers therefore require miniaturized designs to limit capacitance and achieve fast pulse durations.

Previous publications of our group have detailed designs for a nanofabricated beam blanker with integrated photoconductive switch with a simulated pulse duration of 100 fs [20, 21]. Such solutions are highly advanced to the point where the simplicity of a beam blanking solution is lost and practical implementation becomes highly challenging [22]. Easing the demands for pulse duration from hundreds of fs to 10 ps could allow for simpler designs while still accomplishing a significant improvement over conventional beam blankers for experiments that do not require sub-ps time resolution.

Here, we present a micro-fabricated beam blanker with photoconductive switch to rapidly discharge the blanker and generate electron pulses with targeted widths of 10 ps. The small dimensions of the device result in reduced capacitance while the photoconductive switch removes dependence on electronics rise time and trigger jitter for pulse synchronisation. The device is primarily constructed from workshop rather than clean-room components and makes use of a commercially available photoconductive switch for increased accessibility and simpler construction. In this report, we introduce our design and explain design decisions. Furthermore, we present an experimental demonstration of the blanker in the form of streak camera pulse characterisation.

5.2. Principle

A schematic representation of our beam blanking scheme is shown in figure 5.1. One of the blanker plates is grounded while the other is connected to the voltage supply; a photoconductive semiconductor switch (PCSS) connects the blanker plates. The beam comes into the blanker at an angle such that when the blanker voltage is zero, the beam is blocked by an aperture on the optical axis. This is different from the usual situation where the incoming beam is on the optical axis and is transmitted through the aperture without voltage on the plates. From the situation with zero voltage, the blanker goes through a cycle where it is first charged relatively slowly by the voltage supply resulting in the beam slowly traversing the aperture until fully blocked again. When a fs-laser pulse hits the photoconductive switch in the blanker, the plates are shorted and their voltage is rapidly equalised; the beam sweeps over the aperture and a pulse is generated. The photoconductive switch then recovers to its non-conducting state and the cycle starts again. The slow electron pulse generated during the blanker reset is undesired and can be removed with a second blanker, which can be a conventional electrostatic blanker.

The electrical circuit of the blanker is depicted in figure 5.2, where we represent the blanker itself as a capacitor and the photoconductive switch as a variable resistor whose value depends on its on/off state. An additional resistor in the feed line is present as close to the blanker plates as possible to minimize the amount of material that has to switch voltage, thus reducing the total switching capacitance. What we have essentially constructed here is a voltage divider where one of the two resistors has a time varying resistance and a capacitance has been added. During operation, the voltage shifts from the photoconductive switch and blanker to the feed resistor, and back again.

There are two important RC times, namely the discharge RC time τ_{dis} and the recharging RC time τ_{rec} . The discharge RC time is determined by the photoconductive switch

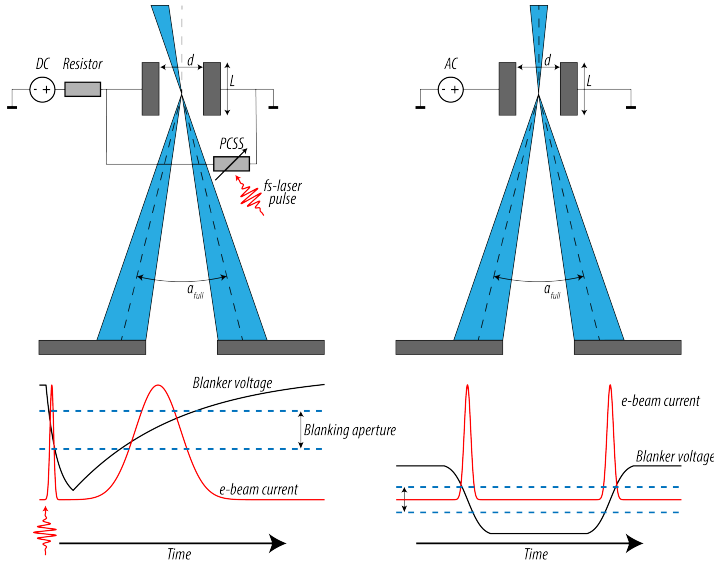


Figure 5.1: Novel laser triggered blanking scheme (left) using a photoconductive semiconductor switch (PCSS) to rapidly equalise the voltage on the blanker plates and generate a fast electron pulse. Contrary to a traditional electrostatic blanker setup (right), the new scheme has the beam coming in at an angle and uses a DC power supply. In both situations, a second electron pulse is generated during blanker reset. In the electrostatic design this second pulse is of equal duration as the primary pulse, but it has to be removed in the laser triggered design, e.g. by a second standard blanker to only transmit the ultrashort pulse.

illuminated resistance and the combined capacitance of the blanker plates, parasitic capacitance of the feed resistor, and capacitance originating from the fields between voltage switched elements to grounded surroundings. The discharge RC time is relevant for the electron pulse duration. The voltage over the blanker during discharge is given in equation 5.2, and combined with equation 5.1 this results in the expression in equation 5.3 for the pulse duration in this design.

$$V(t) = \Delta V \exp(-t/\tau_{dis}) \quad (5.2)$$

$$\tau_{pulse} = \frac{2\Phi\alpha_{full}d\tau_{dis}}{\Delta VL} \quad (5.3)$$

Here ΔV represents the change in voltage over the blanker. With our goal of 10 ps electron pulses, equation 5.3 indicates τ_{dis} is to be approximately 100 ps in case of an acceleration voltage of 5 kV, opening angle of 1 mrad, L/d ratio of 10, and 10 V blanker voltage change. After discharging of the blanker and recovery of the photoconductive switch, τ_{rec} dictates how fast the blanker resets and is determined by the same capacitance as before in combination with the feed resistance; it should be about 1-3 ns for proper functioning of the device with laser pulse repetition frequencies up to 100 MHz.

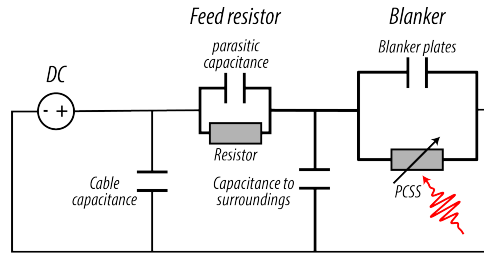


Figure 5.2: The electrical circuit of the laser-triggered blanker. The blanker, represented as a capacitor, is charged with a DC voltage supply at a rate dictated by the feed resistor and blanker capacitance. After photoexcitation, discharging of the blanker occurs via the photoconductive switch, but the parasitic capacitance of the feed resistor also contributes to the discharging RC time and thus has to be minimized.

5.3. Parameters

5.3.1. L/d ratio

The deflection angle of the blanker at a given voltage and beam energy depends linearly on the ratio between plate length and separation L/d , and therefore a larger ratio can provide a shorter pulse duration (see also equation 5.1), which is advantageous. However, the capacitance of a parallel plate capacitor also scales with L/d , meaning that gains in pulse duration from a larger ratio are reduced by slower blanker discharging when the pulse duration is RC time limited. This diminishing effect is however small, as the contribution of the blanker plate capacitance to the total capacitance is less than the impact of the feed plate capacitance to other components and parasitic capacitance of the feed resistor. In addition, a high L/d ratio results in the introduction of increased spot displacement and blur in the probe [23], and in increased difficulty in aligning the device. In extreme cases the beam can hit the blanker plates. We decide on a L/d ratio of 10 to have a reasonable amount of deflection while still being practical.

5.3.2. Device size

Smaller blankers tend to be faster due to lower capacitance, which is a good reason to aim for a miniature design by itself. A second reason to limit the device size is to avoid the situation where circuit size exceeds signal wavelength and transmission line effects and line impedances influence the circuit behaviour. Absorption and pulse reflections of high frequency components then become an issue, and we avoid this by keeping path length sufficiently short. Quantitatively, we aim to keep the path length below a quarter of the signal wavelength such that phase differences stay below 90 degrees and transmission line effects can be neglected. Given the rule of thumb relating 10-90% rise time and bandwidth as $\tau_{10-90} = 0.35/f_{max}$, and assuming a signal speed of $2/3 c$, we arrive at the following expression for the maximum allowable circuit length:

$$L = \frac{1}{4} \frac{\frac{2}{3}c}{f_{max}} = \frac{c\tau_{10-90}}{6 \cdot 0.35} = 1.4 \cdot 10^8 \tau_{10-90} \quad (5.4)$$

With a desired rise time of 100 ps for the blanker discharging, the circuit path length cannot exceed 14 mm. This means that in the blanker design all components have to

be in close proximity to the blanker plates, not only to reduce the switching capacitance but also to prevent transmission line effects. All components - i.e. the blanker plates, photoconductive switch, resistors, and connectors - should therefore be combined into a single entity that can be mounted on a rod that can be inserted in the SEM column and allows for alignment of the blanker to the electron optical axis. This puts another size constraint on the blanker module as the port through which it has to be inserted into the SEM column has a 6.5 mm diameter.

A minimum size requirement stems from our goal of utilising primarily workshop manufactured components rather than cleanroom fabrication techniques. The latter are expensive, time consuming, and labour-intensive undertakings that are difficult to troubleshoot and perfect. We therefore decided to construct our blanker primarily out of workshop manufactured components that are large enough to manipulate and assemble by hand. The smallest part of the blanker will be the gap between the blanker plates; this gap is cut using Electric Discharge Manufacturing (EDM) with which a gap size down to 60 microns can be reliably achieved. We therefore choose for this plate separation in our blanker, and in combination with the pre-determined L/d ratio of 10, this leads to a blanker plate length of 600 microns. In combination with a 200 micron plate width, this would result in a blanker capacitance of roughly 18 fF. However, this does not take into account factors such as the capacitance from the feed plate to other components, and stray capacitance in the resistor, so the actual switching capacitance will be much higher.

5

5.3.3. Spot displacement and blur

Spot displacement and blur are evaluated with the theoretical framework developed by Zhang et al. [23]. Here, we also make the simplification of a linear voltage ramp, but use a ramp from ΔV to 0 rather than $-\Delta V/2$ to $+\Delta V/2$ as would be the case for an electrostatic blanker. This ramp accounts for the greater spot displacement corresponding with the greater deflection angle in our blanking scheme compared to electrostatic blanking. We arrive at the following equations for spot displacement and blur:

$$x_{sd} = \frac{\Delta V L}{2\Phi^2 t_r d \sqrt{q}} \left(\frac{L\sqrt{2\Phi m_0}}{4} \left(\frac{L}{6} - \Delta z \right) - \Phi \Delta z \sqrt{q} (t_{en} - t_r) \right) \quad (5.5)$$

$$x_{blur} = \frac{1}{2\Phi} \frac{\Delta V}{t_r} \frac{L}{d} \tau_{pulse} \Delta z \quad (5.6)$$

Here, t_r represents the voltage rise time, q the elementary charge, m_0 the electron mass, t_{en} the entrance time of the electron into the blanker, and Δz the misalignment of the crossover from the centre of the blanker. For the calculation we use the chosen blanker dimensions ($L = 600 \mu\text{m}$, $d = 60 \mu\text{m}$) in combination with a 5 V voltage drop over 100 ps and a beam energy of 5 keV. Such a fast voltage change on the blanker and modest beam energy result in a larger spot displacement and blur. Calculated spot displacement and blur in the blanker plane is demagnified with a factor $M = 1/25$ by the electron objective lens to obtain values at the sample plane.

We calculate a blur of $5 \cdot 10^{-4} \Delta z$ in the blanker plane, with Δz the vertical alignment offset of the beam crossover with respect to the centre of the blanker. Even with a severe misalignment of 250 micron, nearly half the blanker plate length, this translates to a blur of 5 nm on the sample. Blur will therefore not significantly deteriorate the resolution.

Spot displacement is equal to $x_{sd} = 3.6 \cdot 10^{-8} + \Delta z(4.6 \cdot 10^{-3} - 5.0 \cdot 10^7 t_{en})$, where t_{en} is the entrance time of electrons into the blanker relative to the voltage ramp. In the unfavourable situation of 250 micron misalignment and zero entrance time, the spot displacement amounts to 48 nm on the sample. This is a noticeable shift but will not result in losing the region of interest and can be greatly reduced with better alignment of the crossover than assumed for this calculation.

5.4. Design

We distinguish between the blanker, discussed first, and the optics outside the vacuum necessary to align the system and focus the laser on the blanker, discussed after.

5.4.1. Blanker

Figure 5.3 shows the mechanical design of the blanker. The blanker chip itself has a metal substrate, measuring 3 by 4.5 mm, with the blanker plates on top. One plate, the feed plate, is insulated from the substrate such that we can put a voltage on it to deflect the electron beam. To prevent charging of the insulator affecting the electron beam trajectory, the insulator is shielded from the e-beam by metal ridges on the substrate. The photoconductive switch is mounted on top of the ground plate and the electrodes on it are connected to the blanker plates through wire bonding.

The blanker chip is mounted in a metal cap (shown in brown in the figure) that will be attached to a connecting piece (shown in purple) containing a lens with 5 mm focal length to focus the laser on the photoconductive switch. This unit, containing the blanker chip and the lens, is mounted at the end of the blanker stick that is inserted into the vacuum to position the blanker in the electron beam path, utilising the standard blanker port of our scanning electron microscope. Laser pulses propagate through the blanker stick vacuum window and then through the hollow stick towards the lens and photoconductive switch [22]. The blanker stick also accommodates a wire and resistor for electrical connection to the feed plate of the blanker.

The photoconductive switch we use is a Menlo Systems TERA8-1, a photoconductive device based on LT-GaAs with a sub-ps carrier recombination time. On the GaAs substrate there are two parallel gold channels that have protrusions in the centre of the chip that narrow the gap between the channels to 5 μm over a length of 10 μm (see figure 5.4). Laser excitation of the GaAs in this gap region creates mobile charge carriers that bring about a transient photocurrent in the presence of a bias voltage between the gold strips. The switch is suitable for excitation with our 800 nm fs-laser, with a maximum optical power of 10 mW and maximum bias voltage of 40 V. Figure 5.4c shows a measurement of the photoconductive switch illuminated current measured in ambient conditions mounted on the blanker stick.

The capacitance of the blanker design is numerically calculated with COMSOL Multiphysics; we recreate the design in COMSOL and use the electrostatics toolbox. The total capacitance of the feed plate to all other components is 223 fF. To this we add the capacitance of the feed resistor, which is 40 fF for a 0402 SMD resistor [24], for a total of 260 fF. Therefore, a 10 kOhm resistor is used to yield a 2.6 ns recharge time, which is in the desired range of 1-3 ns. Furthermore, with this capacitance, every 1 pC of charge

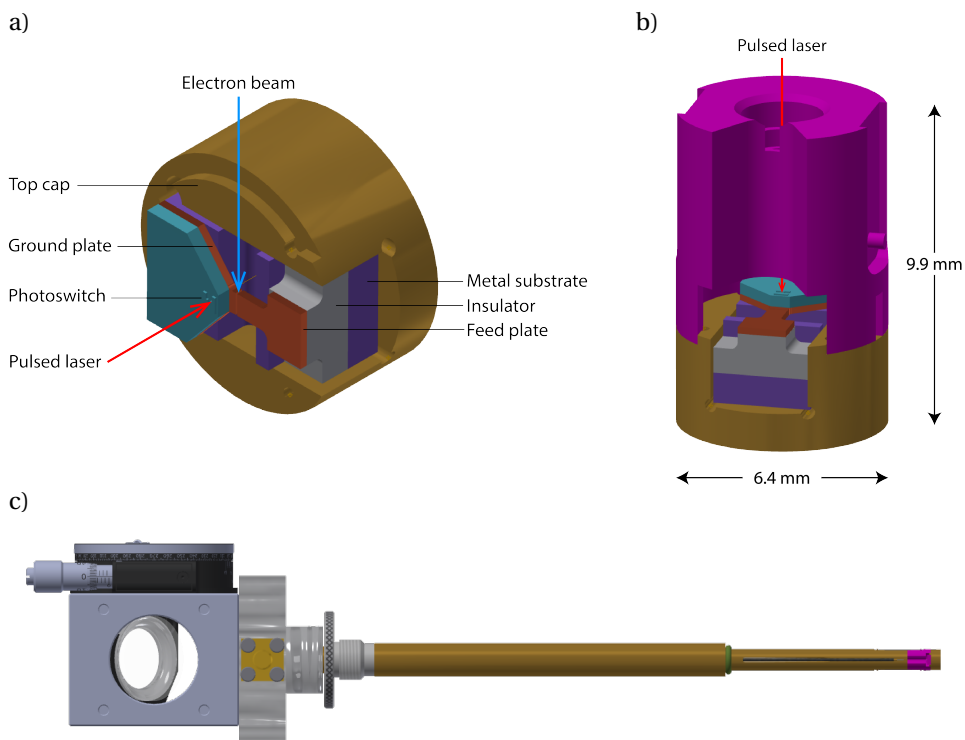


Figure 5.3: Mechanical design of the blanker and blanker stick. (a) The blanker plates and photoswitch are mounted on a metal substrate with a 3 by 4.5 mm footprint. It is inserted into a metal cap (shown in brown). (b) An element containing a 5 mm focal length lens is attached to the cap. (c) The blanker is then mounted on the end of the blanker stick, which is to be inserted into the SEM column. The stick is hollow to accommodate the laser beam entering through a vacuum window, and also contains a wire to connect to the blanker feed plate.

moved through the photoconductive switch results in a voltage modulation of roughly 3 to 4 volts on the blanker. Based on $10 \mu\text{A}$ of current, this can be achieved with pulse repetition frequencies up to 10 MHz ($=10 \mu\text{A}/1 \text{ pC}$) without requiring too high laser power for the switch to withstand. The fs-laser in our setup is a Coherent Vitara-T with a fixed 95 MHz repetition frequency. This exceeds our maximum requirement, and we therefore place a rotating chopper wheel with 10% duty cycle in the laser path, allowing the switch to cool when the laser is blocked by the blades. However, this solution also causes laser pulses to be partially blocked by the blades, introducing unwanted variation in the laser pulse energy.

After excitation, the switch will conduct for the duration of the 1 ps lifetime of the photo-excited carriers in the switch. The more carriers are generated, the lower the resistance. With a blanker capacitance of 260 fF, a switching time equal to the 1 ps lifetime would permit a resistance of only a few Ohms, including the wire resistances and contact resistances. Parasitic resistance contributions are typically on this scale and would therefore affect blanker performance. Furthermore, a switching time this fast is

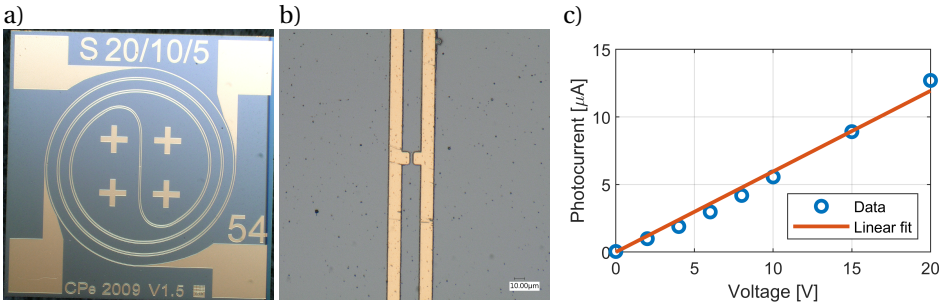


Figure 5.4: (a) The photoconductive switch has a 5x5 mm GaAs substrate with parallel gold conductive channels deposited on top. (b) At the photosensitive area in the centre of the chip, protrusions in the gold channels create a small gap on which the laser is to be focused. The gap measures 5 μm wide and 10 μm long. (c) Illuminated current measured after processing and mounting in the blanker under fs laser illumination at 800 nm, 95 MHz, 10 mW at stick entrance. Current is on the order of 10 μA at 15 V.

not required as equation 5.3 determined 100 ps would be sufficient. Switch conduction time can be modified by regulating the laser pulse duration through the introduction of dispersion with an optical fiber. A laser pulse duration exceeding the carrier lifetime of the switch keeps the switch in its conductive state for the duration of the pulse, at the expense of lower conductance as photon fluence and thereby total displaced charge is unaffected. In addition to reducing the influence of parasitic resistance sources, this means the electron pulse duration can be regulated with the laser pulse duration. This flexibility is advantageous as slow pulses contain more electrons, which can accelerate measurement times by boosting signal strength.

Altering the laser pulse duration affects the blanker discharge rate and voltage drop through a change in photoconductive switch resistance. Assuming the dark current is much smaller than the photocurrent and the laser pulse much shorter than the laser repetition time, the resistance of the switch in its conductive state can be approximated as

$$R_{switch,on} = \frac{\tau_{laserpulse} V}{\tau_{rep} I} \quad (5.7)$$

Here, $\tau_{laserpulse}$, is the laser pulse duration, τ_{rep} the laser pulse repetition time, V the supplied voltage and I the photocurrent. From this it follows that the blanker discharge time τ_{dis} is given by

$$\tau_{dis} = R_{switch,on} C = \frac{VC}{I\tau_{rep}} \tau_{laserpulse} \quad (5.8)$$

with C the total capacitance, showing the blanker discharge time scales with laser pulse duration. With values of 15 Volts, 260 fF, 10 μA, and a pulse repetition frequency of 9.5 MHz, we find the discharge time depends on laser pulse duration as $\tau_{dis} = 3.7 \cdot \tau_{laserpulse}$. Consequently, the blanker will not fully discharge before the switch stops conducting, at which point the voltage drop relative to what it would have been with very long conduction time is

$$\frac{\Delta V_{stop}}{V} = 1 - e^{-\frac{I\tau_{rep}}{VC}} \quad (5.9)$$

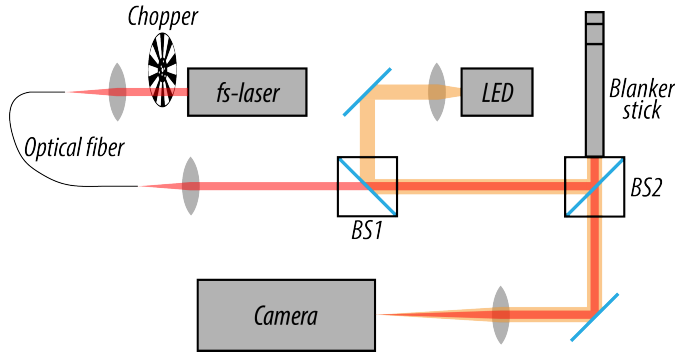


Figure 5.5: The blanker is illuminated with fs-laser pulses for photoswitch actuation and LED lighting for alignment purposes. A multimode fibre guides the laser to the blanker setup and introduces necessary dispersion. The beam passes through a 25% reflecting beam splitter (BS1) where it is combined with LED light, and is subsequently directed into the blanker stick with an 80% reflecting beam splitter (BS2). Reflection images are captured with a Guppy CMOS camera.

5

, or 24% for the numbers given. This effect is not problematic if the electron pulse is generated within this initial voltage drop. Furthermore, the feed resistor and photoconductive switch function as a voltage divider, and when the switch resistance in conductive state approaches the 10 kOhm value of the feed resistor, the voltage modulation of the blanker is further limited. Equation 5.10 below gives the change in blanker voltage if given enough time to stabilise. However, as the laser pulse duration is less than the discharge time, this voltage will not be reached. We therefore combine equations 5.7, 5.9, and 5.10 to obtain an expected voltage drop given in equation 5.11.

$$\frac{\Delta V}{V} = \frac{R_{feed}}{R_{feed} + R_{switch,on}} \quad (5.10)$$

$$\frac{\Delta V_{stop}}{V} = \left(1 - e^{-\frac{I\tau_{rep}}{VC}}\right) \frac{R_{feed}}{R_{feed} + \frac{\tau_{laserpulse} V}{\tau_{rep} I}} \quad (5.11)$$

For example, with 15 Volts supply, 10 μ A photocurrent, 260 fF capacitance, 9.5 MHz repetition frequency, 10 kOhm feed resistance, and 100 ps laser pulse duration, we can therefore expect a 3.1 V modulation of the blanker voltage.

5.4.2. Optics

The laser path to the blanker is shown in figure 5.5. The laser beam from our 95 MHz Coherent Vitara-T fs-laser passes through the rotating chopper wheel placed at the exit pupil and is subsequently coupled into a multimode optical fiber. The fiber has the dual purpose of guiding laser light to the blanker, as well as to stretch pulse duration to increase the time the photoconductive switch is illuminated. We initially use 200 metres of fibre to stretch pulses to an estimated 1 ns, based on an initial pulse duration of 20 fs and dispersion of 3500 fs²/mm. This will have to be shortened later, but for initial experiments the longer pulses are advantageous as they are easier to detect.

At the blanker optics, laser light is coupled out of the fibre and collimated with an 25 mm focal length aspheric lens, after which the beam enters the blanker stick via two beam splitters. The lens at the end of the blanker stick and the collimator lens have a combined magnification of 1/5, so the 50 micron optical fibre is imaged on the photoconductive switch to a geometric spot size of 10 micron. This corresponds to the photoconductive switch gap size. LED illumination and camera imaging of the photoconductive switch facilitates laser alignment on the active area.

5.5. Construction and assembly

Assembly of the blanker begins with the metal substrate which is milled out of metal. On top of this we glue the plastic insulator that will support the feed plate using araldite composite glue. On top of the substrate and insulator we glue an hourglass shaped part that will become the feed plate and ground plate. The glue is cured in the oven and the result is shown in figure 5.6a. Next the gap between the ground and feed plates is cut using EDM; the distance between the plates is 60 microns. Figure 5.6b is a side view of the blanker chip at this point, in which one can already see the gap through which the electron beam will travel.

The photoconductive switch has a substrate too large to fit our design and is therefore cut to size in a wafer dicer, also removing the contact pads on the corners of the chip. Hence, we remove the SiN protective layer on the switch with a dry etching method and add new molybdenum contact pads near the photosensitive area using optical lithography and sputter deposition. Subsequently, the switch is glued onto the blanker ground plate. The whole blanker chip is then inserted into the blanker stick topcap and secured using another drop of composite glue (Figure 5.7a). Next, wire bonding connects the photoconductive switch contact pads to the feed plate and to the topcap (see Figure 5.7b).

The topcap is joined with the connecting piece containing the lens; these parts are manufactured with tight tolerances to fit precisely together and are further secured with composite glue. For mounting the lens-topcap combination on the blanker stick, there is room to manoeuvre and ensure the laser light coming in through the blanker stick illuminates the desired area of the photoconductive switch. The part is mounted on a 3D translation stage and optically imaged through the blanker stick. We move the stage to get the photoconductive switch active area centrally in view (Figure 5.8a) and secure with glue. Next, the feed plate is connected to the feed cable through a resistor (Vishay MCS 0402-professional series). The resistor is to be positioned as close to the feed plate as possible to minimise the switching capacitance. We solder one resistor terminal to the feed cable running along the inside of the blanker stick and connect the other side to the feed plate with conductive silver paint (Figure 5.8b). The blanker is now fully assembled and ready for testing in the SEM.

5.6. Testing

The completed blanker is inserted into our Quanta 200 FEG based USEM setup for testing, where it replaces the conventional electrostatic blanker. Firstly, the blanker is to be positioned at the electron optical axis. There is a crossover close of the electron beam close to the blanker position, which can be used to image the blanker to facilitate alignment.

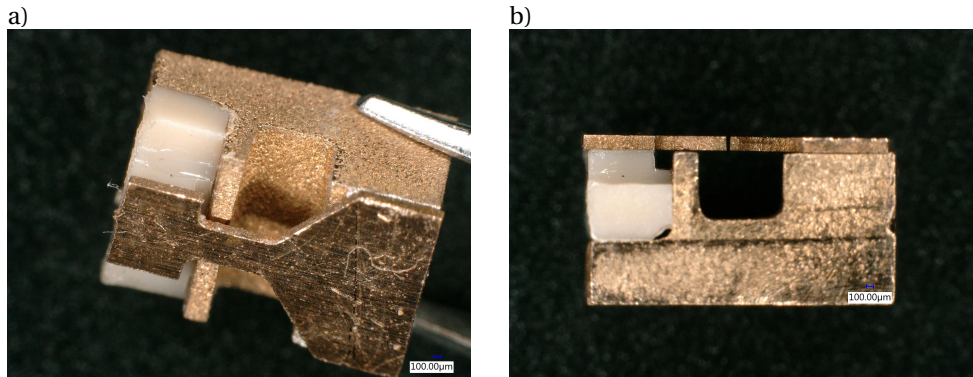


Figure 5.6: (a) Blanker chip substrate with blanker plate on top. (b) The blanker gap is cut with EDM, creating a narrow slit that the electron beam will travel through. Both images show the feed plate on the left and the ground plate on the right. Scale bar 100 μm (in blue).

5

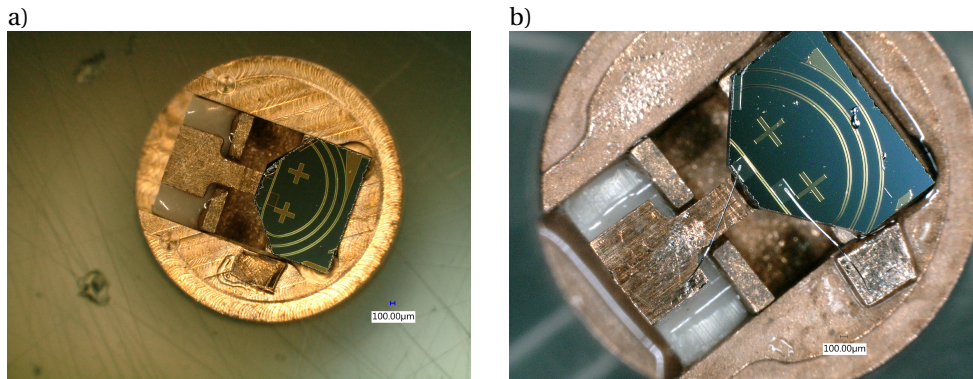


Figure 5.7: (a) The blanker is inserted in the blanker stick topcap and secured with composite glue. (b) Electrical contacts with the photoconductive switch are made with wire bonding. Scale bar 100 μm (in blue).

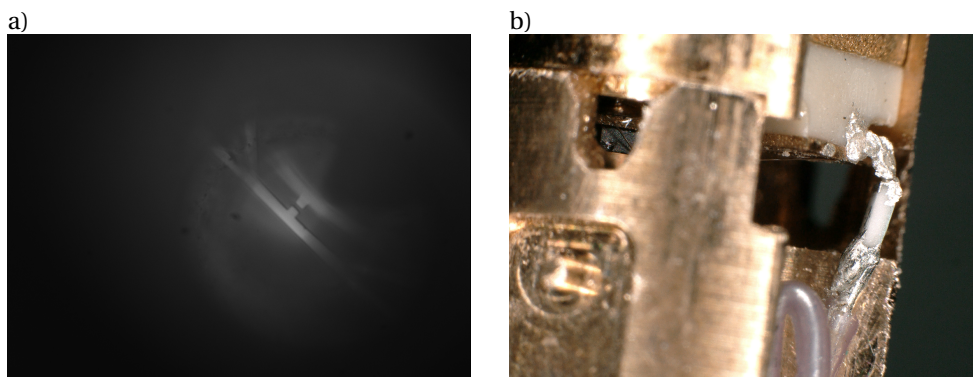


Figure 5.8: (a) Image of the photoconductive switch taken through the blanker stick to ensure correct positioning before securing the connecting piece with glue. (b) The feed plate is then connected to the feed cable in the blanker stick through a 10 k Ω feed resistor.

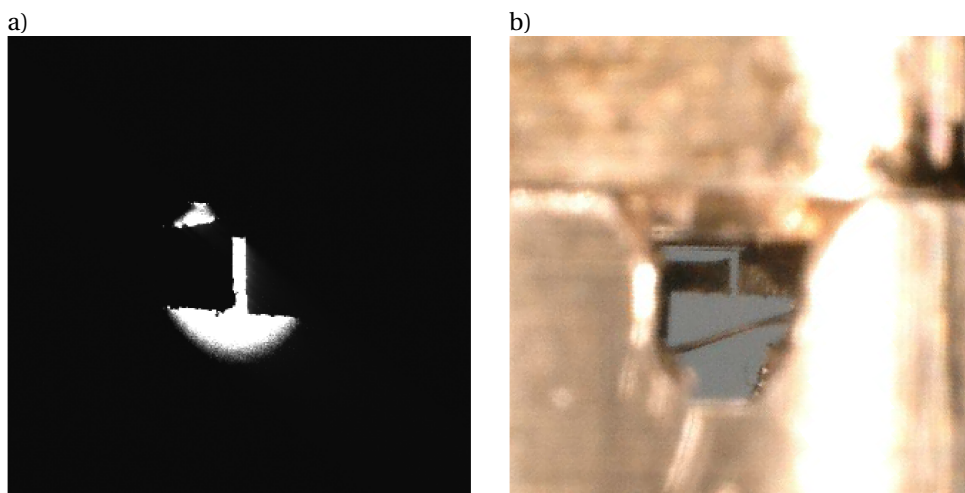


Figure 5.9: (a) SEM image of the blanker plates made by scanning the beam crossover while the blanker is mounted, showing the blanker is successfully positioned in the electron beam path. (b) The optical image for comparison was taken before mounting with the same view.

We adjust lens currents to focus the crossover plane on the blanker and scan the crossover position with the gun shift and tilt coils higher in the column, recording secondary electron generated by transmitted electrons. A beam energy of 5 keV is used for all experiments. Mechanical adjustment of the blanker position are then made to centre it around the optical axis, and the blanker is rotated such that the plates are parallel to the optical axis and the beam can travel in between. Figure 5.9 shows the blanker gap in crossover scanning mode after these alignments, and also an optical image of the same view taken before mounting in the SEM. A clear image of the gap indicates the blanker is correctly positioned in the SEM column.

Laser focussing on the photoconductive switch is done coarsely by moving the laser spot to the gap area on the camera image of the switch imaged through the blanker stick. Fine adjustments are subsequently made by optimising the photocurrent. Figure 5.10 shows the photoconductive switch imaged through the blanker stick with the laser off and on, showing the laser spot is positioned at the gap and has a size comparable to the gap size.

A streak camera approach [15, 22] is employed to characterise deflection by the blanker, see also figure 5.11. A second deflector is positioned between the electron objective lens and a scintillating sample consisting of cerium doped yttrium aluminium garnet (YAG:Ce); emitted cathodoluminescence is imaged on a CCD camera. The electron objective lens is defocussed such that a deflection of the beam by the blanker or streak camera deflectors will move the electron beam position on the YAG screen, which is visible on the CCD camera image. To minimize the size of the defocussed spot and maximize visibility of spot displacement, the variable aperture above the blanker is set to 20 μm and moved off axis to pinch the beam and further reduce its opening angle.

Generation of electron pulses requires laser induced deflection of the electron beam

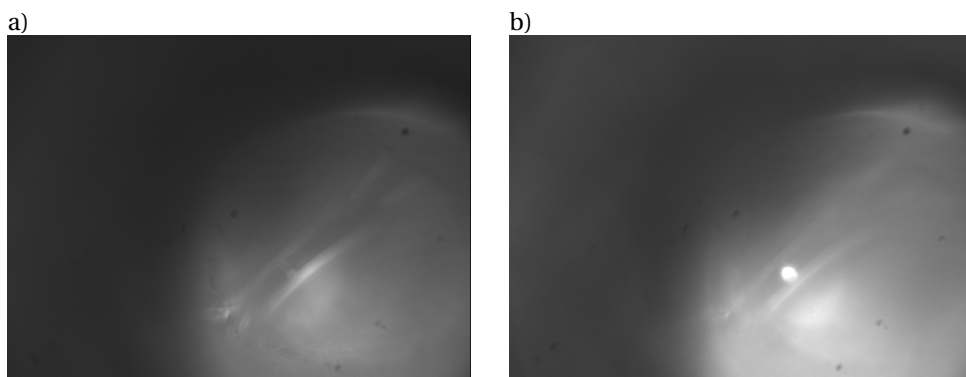


Figure 5.10: Optical images of the photoconductive switch with the laser off (a) and on (b) demonstrate the optics used to focus the laser on the switch is functional. The spot is positioned at the photoconductive switch active area and has dimensions comparable to the gap size.

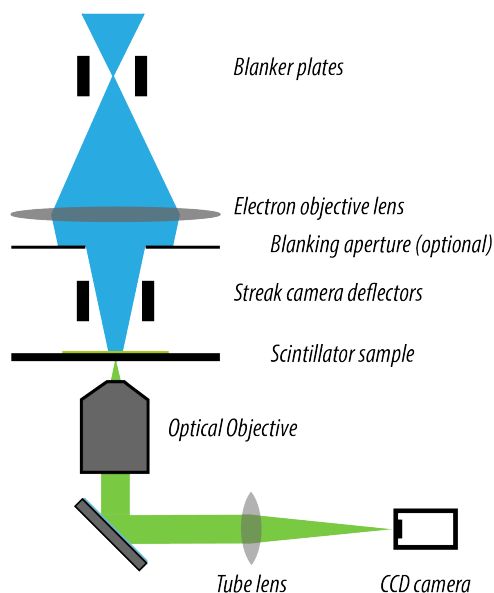


Figure 5.11: Streak camera characterisation of the blanker is implemented by positioning a second deflector between the electron objective lens and a scintillating sample imaged with an integrated optical microscope. With the electron beam defocussed, deflections by blanker as well as streak camera translate to movement of the cathodoluminescence spot imaged by the camera while there is a beam crossover in the blanker plane.

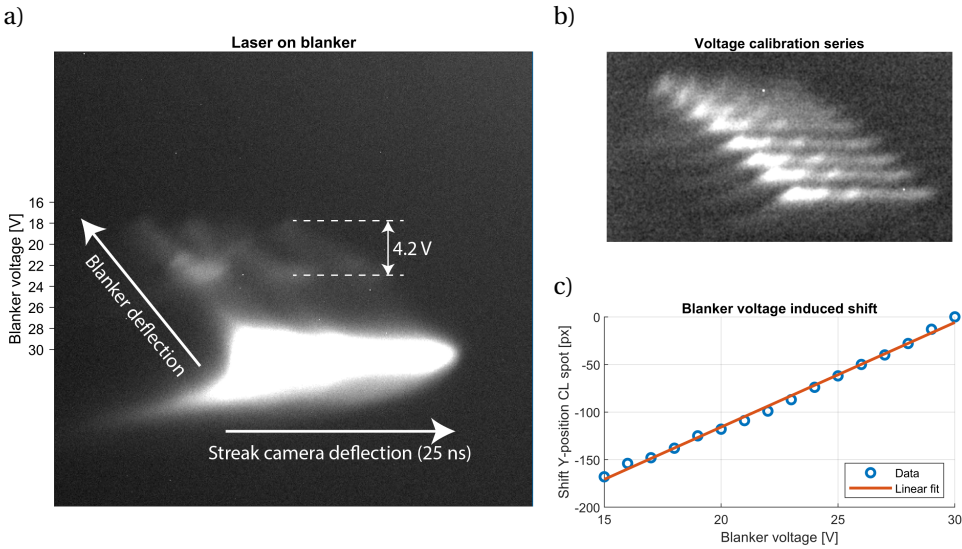


Figure 5.12: Streak camera measurements indicate laser induced electron beam deflection. (a) A 25 ns voltage ramp on the streak camera deflects the electron beam in the direction left to right while the laser excited blanker deflects in the diagonal direction. A wave like pattern with roughly 2.5 oscillations is seen, indicating periodic deflection by the blanker at the 95 MHz (10.5 ns) laser repetition time. The bright saturated line is the result of the streak camera scanning without the blanker deflecting as the laser is blocked by the chopper. (b) Summed images acquired with various DC blanker voltages without laser excitation of the blanker. They are used to calibrate beam position to blanker voltage through measuring image shift. (c) Image shift as a function of DC blanker voltage shows a linear trend of 11 pixels per volt; we add this voltage scale to figure (a) and determine the laser induced blanker voltage modulation to be in excess of 4 V.

at the laser repetition frequency of 95 MHz. To demonstrate this, we set up the streak camera with a 5 V ramp signal with a 25 ns rise time and 5 ns fall time. The signal from a laser illuminated photodiode is frequency divided by a factor 4 and triggers the generation of this ramp every 42 ns. We ensure the electron objective lens is defocused and the blanking aperture removed. Figure 5.12a shows the camera image of the scintillator with a blanker supply voltage of 30 V and laser power corresponding to a photocurrent of 23 μA . The streak camera deflects in the horizontal direction, effectively creating a time axis, while the blanker deflects along the diagonal direction indicated in the figure. There are multiple features visible in this image. Firstly, the bright horizontal line, which shows the electron beam being deflected by the streak camera with the laser blocked by the chopper wheel. As the blades rotate and the switch is exposed to laser light, the voltage over the blanker plates drops, causing deflection to the top left in the CCD image. Here, we see a wave like shape with circa 2.5 oscillations, indicating that the blanker voltage drops and (partially) recovers 2.5 times over the 25 ns streak camera ramp time. The deflection occurs periodically with 10 ns repetition time, which is in agreement with the 95 MHz laser repetition time, and indicates that we measure periodic laser induced electron beam deflection.

The laser induced voltage drop can be quantified by relating the position on the CCD

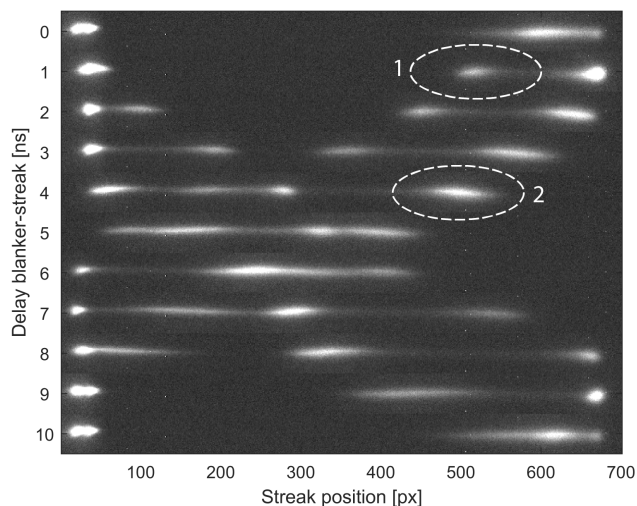


Figure 5.13: Streak camera results, shown here in the form of a stack of streak camera strips, recorded with blanker aperture inserted show two pairs of pulses moving in opposite direction when changing the delay. Each pair consists of a laser generated (marked 1) and a recovery pulse (marked 2), with the latter lagging the former. The longer pulse duration of the recovery pulse is reflected by brighter and wider signature on the streak camera result.

image to blanker voltage. To this end, we record images of the scintillator with various DC voltages on the blanker without laser exciting the blanker (figure 5.12b). In range of 30 down to 15 V, a shift of 11 pixels in the position of the CL spot is recorded per volt change on the blanker (figure 5.12c). Adding this voltage scale to figure 5.12a shows a laser induced blanker voltage variation of about 4 V. A modulation of 3.4 V was expected based on equation 5.11, which is in reasonable agreement. Moreover, figure 5.12a indicates the beam deflection angle is larger than the opening angle, which is a prerequisite for electron pulse generation.

Electron pulses are generated by inserting a blanking aperture (30 micron diameter) between electron objective lens and streak camera deflector. Streak camera characterisation of electron pulses transmitted by the blanking aperture is performed to ascertain the generation of pulses and measure their duration. For these measurements, the electron beam is focussed on the sample while the blanker (25 V, 21 μ A) deflects it over the blanking aperture. A square wave signal at 47.5 MHz, half the laser frequency, on the streak camera deflector streaks the pulses over the scintillator sample, which is imaged with the CCD camera. We vary the delay between the excitation of the blanker photoconductive switch and deflection of the streak camera, acquiring multiple images to track pulses in time.

Streak camera results are shown in figure 5.13. As the streak camera signal and laser frequency differ by a factor two, there are two pairs of pulses that move in opposite direction corresponding to the rising and falling edge of the streak camera signal. Each pair consists of a laser generated electron pulse and a recovery pulse formed as the blanker resets. Comparing the marked pulses in the image, we see the recovery pulse, lagging the

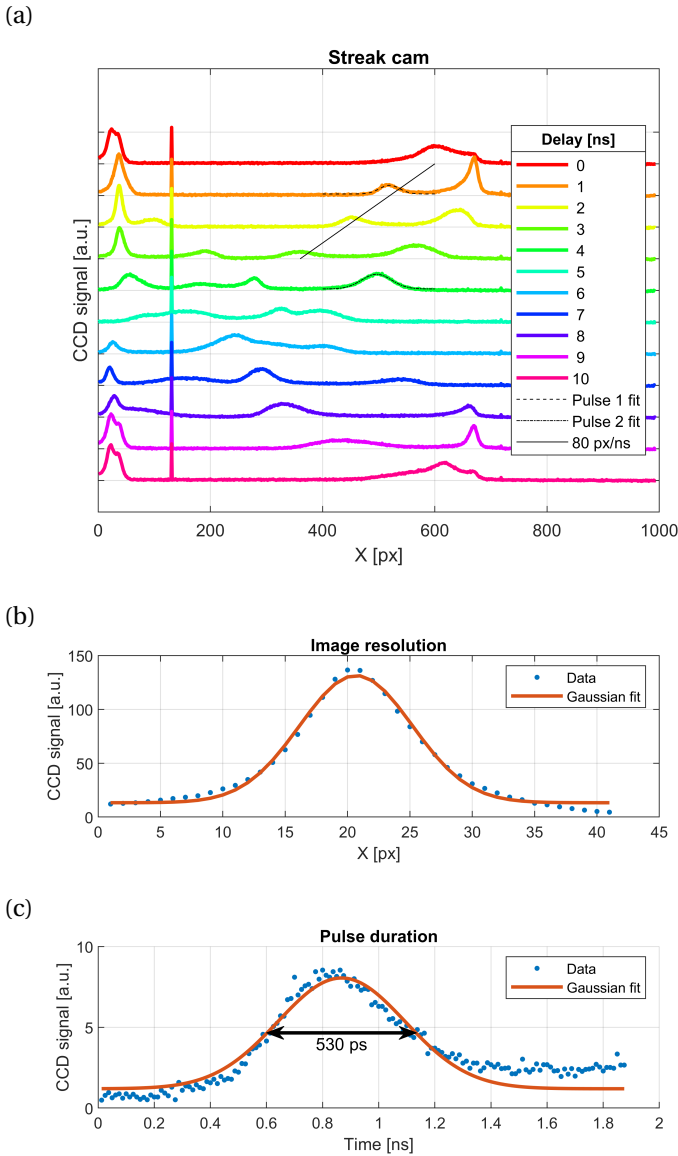


Figure 5.14: (a) Streak camera profiles show a peak shift of 80 pixels per nm. In combination with Gaussian fitting to peaks yielding Gaussian sigma values of 18 and 27 pixels for pulses 1 and 2 respectively, we calculate pulse durations of 530 and 780 ns full width half maximum. (b) A profile of the CL spot generated by a stationary beam. With a Gaussian width of 4.5 pixels, this demonstrates that that the instrument response is not limiting the pulse measurements. (c) The fit to pulse 1 shows 530 ps FWHM pulse duration.

laser-generated pulse, is brighter and wider than the laser generated pulse. This is due to the longer pulse duration of the recovery pulse, resulting from the slower reset time than discharge time of the blanker.

Figure 5.14 shows line profiles along each of the measured streaks and allows us to extract the pulse duration. For this, we first translate the pixel values on the x-axis to time by determining the shift in peak position resulting from a change in delay between the blanker and streak excitation. The black line along the first pulse travelling leftwards shows a shift of 80 pixels per ns and represents the data well. Subsequently, we fit Gaussian functions to a laser generated pulse (pulse 1) and a recovery pulse (pulse 2) and find Gaussian sigma values of 18.1 ± 1.1 and 26.7 ± 0.7 pixels, respectively. These values include blurring by the optical point spread function (PSF) that is introduced in the imaging of the scintillator (figure 5.14b), but with a PSF sigma of 4.5 pixels the effect of deconvolution is smaller than the fitting uncertainty and is therefore neglected. As the position in the streak is similar, we use the same conversion factor of 80 pixels per ns for both peaks. Also converting from sigma values to full width half maximum we arrive at 530 ± 30 ps for the laser generated pulse and a significantly longer value of 780 ± 20 ps for the recovery pulse. From the fitted peak positions we calculate a time lag of 2.7 ns between the pulses, which is as designed and sufficiently long to block the recovery pulse with an additional blanker.

5.7. Discussion

The obtained value of 530 ps is far away from the target value of 10 ps. However, we note that these measurements have been done with a very long (~ 1 ns) laser pulse duration in order to maximize deflection before optimizing pulse duration. Filling in the used experimental parameters into equation 5.3 to calculate the pulse duration with discharge time and voltage drop determined with equation 5.8 and 5.10 results in a pulse duration of 250 ps. Additionally, our method of increasing laser pulse energy while limiting average power with a rotating chopper wheel in the laser path, while proven effective in preventing thermal overload of the switch, is not ideal and affects pulse duration. The gaps between chopper blades are 4 mm and the laser beam diameter is about 2 mm, resulting in the partial transmission of pulses during the transition between blocking and unblocking the beam. With these dimensions, two thirds of the laser pulses that arrive at the switch have reduced energy, and the average laser pulse energy is reduced by 33% compared to a chopper that can pick pulses without partial transmission. Pulse duration is strongly dependent on photocurrent, as this 33% reduction in photocurrent would result in a pulse duration of 480 ps according to equation 5.3 with all other parameters unchanged. This is close to our experimental result, meaning that the blanker performs as well as we can expect it to given the current implementation.

Follow up experiments will have to be done with shorter laser pulse durations for a shorter and stronger reduction of the switch resistance, resulting in faster discharging of the blanker plates. Crucial is that the charge transferred by the photoconductive switch does not decrease with shorter pulse durations. It also remains to be investigated if the effect of resistances of other components and contacts on the discharging RC time can become a limiting factor as the switch resistance is decreased. Furthermore, the chopper needs to be replaced with a solution that does not introduce variation in laser pulse energy. A laser that can generate pulses at a suitable repetition frequency would be an

option. Alternatively, a pulse picker could be employed to reduce the pulse repetition time of the laser. In either case the laser pulse energy can be safely increased without introduction of additional frequency components and variable laser pulse energy. With these changes, the goal of 10 ps electron pulses is expected to be achieved with a laser pulse duration of 75 ps, based on equations 5.3, 5.8, and 5.10.

Some practical concerns that need addressing for a follow up design include a charging problem that complicates alignment of the electron beam through the blanker and can still affect beam quality despite the fact that a beam could be transmitted for the experiments presented here. The source of the charging is possibly glue that has flown out before curing, but this could nevertheless require additional shielding in a new design. Furthermore, the number of processing steps required on the photoconductive switches is high and often requires clean room access. This detracts from the intended simplicity of manufacturing and is not without risk of damage as multiple switches were lost in the process. Minimizing required processing steps by procuring more suitable switches would therefore be an improvement. The addition of a second blanker to remove the electron pulse generated as the blanker resets also remains to be implemented. However, our streak camera characterisation of the blanker already demonstrates the possibility to temporally align a second deflector to the laser triggered blanker, albeit for a different purpose.

5.8. Conclusion

In conclusion, we have designed and built a laser triggered electron beam blanker for the generation of electron pulses, and the prototype device has been tested in a commercial SEM. We have demonstrated laser triggered electron beam deflection by the blanker and shown that the deflection is sufficient to create electron pulses. The ability to form electron pulses has been confirmed with streak camera characterisation and constitutes a significant milestone in the development of the device.

We measured a pulse duration of 530 ps, but this includes the detrimental effect of variable laser pulse energies and it is also expected that improvements can be made with shorter and higher energy laser pulses. On the longer term, the photoconductive switch is where the largest improvements can be made as the current through it ultimately determines the how fast the blanker is capable of switching. Additionally, the incorporation of the switch in the blanker is the most challenging part of constructing the blanker. Therefore, a photoconductive switch capable of higher current requiring fewer processing steps would benefit both the performance and practicality of the blanker.

References

- [1] J. Spencer Baskin and A. H. Zewail, "Seeing in 4D with electrons: Development of ultrafast electron microscopy at Caltech", *Comptes Rendus Physique* **15**, 176–189 (2014).
- [2] G. M. Vanacore, A. W. P. Fitzpatrick, and A. H. Zewail, "Four-dimensional electron microscopy: Ultrafast imaging, diffraction and spectroscopy in materials science and biology", *Nano Today* **11**, 228–249 (2016).

- [3] A. Adhikari, J. K. Eliason, J. Sun, R. Bose, D. J. Flannigan, and O. F. Mohammed, “Four-Dimensional Ultrafast Electron Microscopy: Insights into an Emerging Technique”, *ACS Applied Materials & Interfaces* **9**, 3–16 (2017).
- [4] A. H. Zewail, “Four-dimensional electron microscopy”, *Science* **328**, 187–193 (2010).
- [5] P. Hommelhoff, C. Kealhofer, and M. A. Kasevich, “Ultrafast electron pulses from a tungsten tip triggered by low-power femtosecond laser pulses”, *Physical Review Letters* **97**, 247402 (2006).
- [6] Y. Morimoto and P. Baum, “Diffraction and microscopy with attosecond electron pulse trains”, *Nature Physics* **2017 14:3 14**, 252–256 (2017).
- [7] K. E. Priebe, C. Rathje, S. V. Yalunin, T. Hohage, A. Feist, S. Schäfer, and C. Ropers, “Attosecond electron pulse trains and quantum state reconstruction in ultrafast transmission electron microscopy”, *Nature Photonics* **2017 11:12 11**, 793–797 (2017).
- [8] D. S. Yang, O. F. Mohammed, and A. H. Zewail, “Scanning ultrafast electron microscopy”, *Proceedings of the National Academy of Sciences* **107**, 14993–14998 (2010).
- [9] A. Feist, N. Bach, N. Rubiano da Silva, T. Danz, M. Möller, K. E. Priebe, T. Domröse, J. G. Gatzmann, S. Rost, J. Schauss, S. Strauch, R. Bormann, M. Sivilis, S. Schäfer, and C. Ropers, “Ultrafast transmission electron microscopy using a laser-driven field emitter: Femtosecond resolution with a high coherence electron beam”, *Ultramicroscopy* **176**, 63–73 (2017).
- [10] L. Zhang, J. P. Hoogenboom, B. Cook, and P. Kruit, “Photoemission sources and beam blankers for ultrafast electron microscopy”, *Structural Dynamics* **6**, 10.1063/1.5117058 (2019).
- [11] N. C. MacDonald, G. Y. Robinson, and R. M. White, “Time-resolved scanning electron microscopy and its application to bulk-effect oscillators”, *Journal of Applied Physics* **40**, 4516–4528 (1969).
- [12] K. Ura, H. Fujioka, and T. Hosokawa, “Picosecond pulse stroboscopic scanning electron microscope”, *Journal of Electron Microscopy* **27**, 247–252 (1978).
- [13] D. Winkler, R. Schmitt, M. Brunner, and B. Lischke, “Flexible picosecond probing of integrated circuits with chopped electron beams”, *IBM Journal of Research and Development* **34**, 189–203 (1990).
- [14] S. Meuret, M. Solà Garcia, T. Coenen, E. Kieft, H. Zeijlemaker, M. Lätzel, S. Christiansen, S. Y. Woo, Y. H. Ra, Z. Mi, and A. Polman, “Complementary cathodoluminescence lifetime imaging configurations in a scanning electron microscope”, *Ultramicroscopy* **197**, 28–38 (2019).
- [15] R. J. Moerland, I. G. C. Weppelman, M. W. H. Garming, P. Kruit, and J. P. Hoogenboom, “Time-resolved cathodoluminescence microscopy with sub-nanosecond beam blanking for direct evaluation of the local density of states”, *Optics Express* **24**, 24760 (2016).
- [16] Berkeley Nucleonics, *Model 765 Fast Rise Time Pulse Generator*, 2020.

- [17] W. Verhoeven, J. F. M. van Rens, E. R. Kieft, P. H. A. Mutsaers, and O. J. Luiten, “High quality ultrafast transmission electron microscopy using resonant microwave cavities”, *Ultramicroscopy* **188**, 85–89 (2018).
- [18] J. F. M. Van Rens, W. Verhoeven, E. R. Kieft, P. H. A. Mutsaers, and O. J. Luiten, “Dual mode microwave deflection cavities for ultrafast electron microscopy”, *Applied Physics Letters* **113**, 163104 (2018).
- [19] M. W. H. Garming, M. Bolhuis, S. Conesa-Boj, P. Kruit, and J. P. Hoogenboom, “Lock-in Ultrafast Electron Microscopy Simultaneously Visualizes Carrier Recombination and Interface-Mediated Trapping”, *Journal of Physical Chemistry Letters* **11**, 8880–8886 (2020).
- [20] I. G. C. Weppelman, R. J. Moerland, J. P. Hoogenboom, and P. Kruit, “Concept and design of a beam blanker with integrated photoconductive switch for ultrafast electron microscopy”, *Ultramicroscopy* **184**, 8–17 (2018).
- [21] I. G. C. Weppelman, R. J. Moerland, L. Zhang, E. Kieft, P. Kruit, and J. P. Hoogenboom, “Pulse length, energy spread, and temporal evolution of electron pulses generated with an ultrafast beam blanker”, *Structural Dynamics* **6**, 10.1063/1.5089517 (2019).
- [22] I. G. C. Weppelman, “Creation of electron pulses with a laser-triggered micro fabricated electron beam deflector”, PhD thesis (2021).
- [23] L. Zhang, M. W. H. Garming, J. P. Hoogenboom, and P. Kruit, “Beam displacement and blur caused by fast electron beam deflection”, *Ultramicroscopy* **211**, 112925 (2020).
- [24] Vishay Intertechnology, *Frequency Response of Thin Film Chip Resistors*, 2009.

6

Conclusion

The project was started with the goal of expanding the capabilities of USEM through improvements and innovations in the instrumentation and increased understanding of the technique and contrast mechanisms.

Adaptations to previously reported USEM experiments have been made with the introduction of lock-in USEM in chapter 2. This alternative detection scheme allowed for simultaneous recording of processes on multiple time scales as well as highlighting the impressive sensitivity of USEM to surface morphology. In chapter 3, we implemented USEM with high-NA laser excitation to bring the pump resolution below 1 micron, allowing for more local excitation of samples than previously possible. In both these chapters dealing with charge carrier dynamics, dipolar contrast patterns were observed in the ultrafast movies recorded. These adjacent regions that show an increase and decrease in detected secondary electron signal have been determined to be the result of a local photo-induced surface potential through particle tracing simulations. This finding provides additional insight into the contrast mechanism that enables imaging carrier dynamics with USEM.

A further application of USEM has been investigated in chapter 4, where we imaged the motion of a micromechanical resonator. Here, the standard detection scheme without lock-in detection was used, but we employed an alternative excitation scheme compared conventional single pulse pumping of the sample. A cantilever was brought into motion through a pulse frequency modulation scheme on the laser excitation and imaged with pulsed electrons to construct a video of the resonator moving at resonance.

The work presented in chapter 5 pertains to improvement of the electron pulse duration, which is a fundamental specification of any ultrafast electron microscopy setup that determines temporal resolution. A new design for a laser triggered electron beam blaster was presented, and a prototype constructed and tested. Laser triggered electron pulses have been generated, but additional work is required to reach the targeted 10 ps pulse duration.

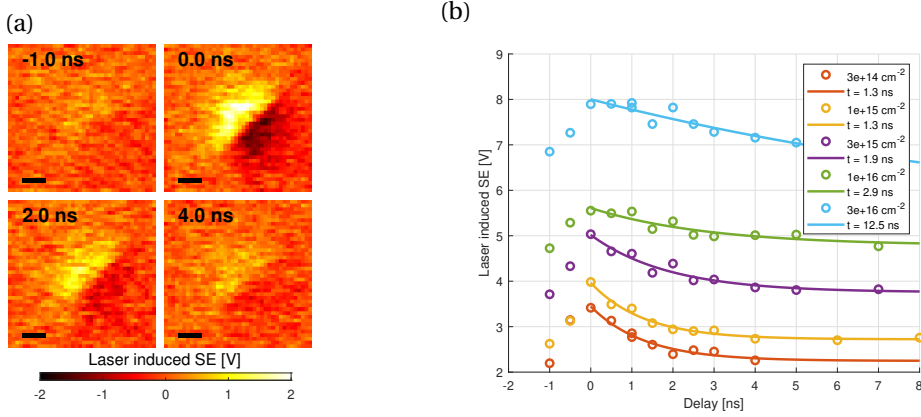


Figure 6.1: **Lock-in USEM can be used to image the effect of ion implantation on the carrier lifetime near semiconductor surfaces, as shown here for copper indium selenide (CIS).** (a) Ultrafast movie frames of laser induced SE measured on CIS implanted with 30 kV hydrogen ions at a dose of $3 \cdot 10^{15} \text{ cm}^{-2}$. A dipolar pattern appears due to the formation of a surface potential, which recedes as carriers recombine. (b) Decay curves extracted from USEM movies, plotted with offsets for visibility, recorded on samples with doping doses ranging from $3 \cdot 10^{14}$ to $3 \cdot 10^{16} \text{ cm}^{-2}$. A trend of increasing lifetime with dose is observed. Scale bars of 100 μm . Sample courtesy of G. Naresh-Kumar and M. V. Yakushev of Strathclyde University.

6.1. Outlook

The findings presented in this thesis provide openings for future research. The high degree of surface sensitivity evident from our results on semiconductor carrier dynamics can be of great benefit depending on the use case. Where techniques that rely on bulk interactions see a reduction in signal strength when sample thickness reduces, the high surface sensitivity in USEM does not suffer from this. This provides interesting prospects for the characterisation of thin samples such as 2D materials, or samples that have undergone surface modification of some sort. An example of the latter is to study semiconductor materials doped through ion implantation, where only the top layer of the sample is affected by the doping process.

As a demonstration of the merit of surface sensitivity, figure 6.1 shows a lock-in USEM measurement of the doping dependence of carrier lifetime of copper indium selenide (CIS) that has been implanted with hydrogen ions. CIS is a material with applications to photovoltaics, where doping of semiconductors is valuable to achieve more favourable carrier properties. As only the top layer of the sample is implanted, typical bulk sensitive techniques that can be employed to probe carrier dynamics will see their signal heavily diluted by signal originating from unaffected sample material deep below the surface. Our technique resolves a clear relation between hydrogen dose and carrier lifetime. It should also be noted that these results were mostly measured in one day, which means samples can be measured on a time scale similar to how fast they can be prepared.

An undesirable side effect of high surface sensitivity can be the probing of effects that are not the target of investigation. The dependence of the contrast pattern on electron dose reported in chapter 3 indicated sensitivity to electron beam induced sample modification, likely related to deposition of carbonaceous material. This stresses the

importance of proper cleaning and handling of the sample and the vacuum chamber to limit contamination. However, the presence of contaminants cannot be excluded completely at high vacuum (10^{-6} mbar), which is why an alternative solution is required for sample materials that require very long measurement times or are otherwise beam sensitive. Implementation of ultrahigh vacuum (UHV) in a USEM setup greatly reduces contamination concentrations and therefore deposition rates. Other matter, such as water layers that can decompose into free radicals under the influence of the electron beam, will also be removed and therefore the influence of these external factors is reduced. However, practical downsides of UHV include long pumping times and different requirements on the vacuum chamber. Alternatively, solutions such as sample heaters and cold traps can be investigated to reduce contaminant concentration at the sample.

The ultrafast movies of nanomechanical motions (chapter 4) demonstrate the capability of measuring with nanoscale spatiotemporal resolution. Interesting continuations of this work would be to image the interaction of an AFM cantilever with a surface, which would require a piezo stage to make the cantilever gradually approach a stationary sample, or vice versa. Application to different types of resonators can also be investigated, including graphene drums or carbon nanotube resonators. Such resonators can have resonance frequencies in the GHz range, which is faster than the maximum achievable modulation frequency of the laser and necessitates different excitation methods. Additionally, higher resonance frequencies require shorter electron pulses for sharp images of the oscillator.

The pulse duration achievable with the laser triggered blanker discussed in chapter 5 can likely be improved from the currently realized 530 ps to values below the 90 ps achieved with the electrostatic blanker. Charging problems in the current prototype make experiments with this blanker difficult, and therefore these problems need to be addressed. Optimization of the laser pulse duration and implementation of a pulse picker to reduce the laser repetition frequency can then result in a vast improvement of pulse duration. Lower repetition frequencies enable higher laser pulse energies and consequently faster electron pulses. Therefore we note that the laser triggered blanker is most suited to ultrafast measurements conducted at lower repetition frequencies. When the targeted pulse duration of 10 ps is achieved, this blanker can fill the gap between the sub-ps pulse duration of laser triggered sources and the conventional electrostatic blanker.

Acknowledgements

Doing this PhD was quite the journey and I am fortunate to have met so many great people along the way. Without support of others, this thesis would have never been completed, and I am grateful for all the help I got. Along with those who made direct contributions to the work, I also thank those who had positive impacts indirectly and made the past years more enjoyable. Some people I would like to thank specifically for the role they have played.

I extend my gratitude to Jacob for his supervision over the past years. Many good discussions have resulted in steady progression of the work, and you really helped push me in the right direction at times when progress was more difficult. These pushes have often led to new ideas, which I learned a lot from, particularly when slightly outside my comfort zone. Also in the presentation of the work, your critical eye for detail has significantly improved the quality of both the thesis and the papers we have published. Your support has been very important for my development into the researcher I am today, and for that I thank you. I would also like to thank Pieter for his guidance and contributions. The many creative ideas you had during the project meetings and great knowledge of physics have been very helpful. Next, I thank Robert and Gerward for their help, support, and supervision during and after my bachelor and master thesis projects, and for piquing my interest in the topic and science in general. Without you, I might not have even started this PhD project.

I worked together with a variety of people, without whom these results could not have been achieved. First, I thank Lixin Zhang. We closely collaborated on the design, fabrication, and testing of the laser triggered blanker that led to chapter 5. I look back on this with pleasure and learned a lot working with you. Next, I would like to thank Naresh Kumar for our collaboration, where we got nice results applying USEM to doped semiconductors. It was really interesting to exchange thoughts and run various experiments together. I also thank Martin Lee. While we initially met to talk about ITO glass, our discussions about MoS₂ and mechanical resonators have been very valuable and led to us working together. I much appreciate your input and the samples provided. I also thank Irek Roslon for the work on drum resonators.

The technical staff of the group played a pivotal role in enabling the experimental work done for this project. I thank Dustin for his help in keeping the microscope up and running. You were always very quick diagnosing and solving problems, and I admire your enthusiasm for SEMs. Next, I thank Carel for his work on sample fabrication, and for introducing me to cleanroom fabrication techniques. I also thank Martin for his work in the cleanroom, and Paul and Han for their help with the electronics.

Our research group is full of wonderful people that have been great to work with, and to not work with. I appreciate everyone's willingness to lend helping hands and input during work related discussions, but also the company during coffee breaks and Friday afternoon drinks. I am grateful to all of you, but I would particularly like to thank Yoram,

whom I shared an office with for all these years, and also Ryan and Luc. We all started at roughly at the same time and have had many good discussions, work related or otherwise, that have been useful as well as fun. It has been a pleasure to work alongside you and to spend time together outside of work.

Furthermore, I thank Stefan, Bart, and Ahmad for the good times shared since we all started our studies in Delft. Our cycling trips in particular have been great breaks from research.

I also thank my family for their continued support during the past years. Your enthusiasm and encouragement has been heartwarming and I'm grateful for it. The last words are for Lisanne, you have been hugely supportive, which made finishing the PhD considerably easier. Thank you.

- L. Zhang, M. W. H. Garming, J. P. Hoogenboom, and P. Kruit, “Beam displacement and blur caused by fast electron beam deflection”, [Ultramicroscopy](#) **211**, 112925 (2020)
- M. W. H. Garming, I. G. C. Weppelman, P. De Boer, F. P. Martínez, R. Schirhagl, J. P. Hoogenboom, and R. J. Moerland, “Nanoparticle discrimination based on wavelength and lifetime-multiplexed cathodoluminescence microscopy”, [Nanoscale](#) **9**, 12727–12734 (2017)
- R. J. Moerland, I. G. C. Weppelman, M. W. H. Garming, P. Kruit, and J. P. Hoogenboom, “Time-resolved cathodoluminescence microscopy with sub-nanosecond beam blanking for direct evaluation of the local density of states”, [Optics Express](#) **24**, 24760 (2016)